

Realization of Beam Polarization at the Linear Collider and its Application to EW Processes.

Dissertation
zur Erlangung des Doktorgrades
des Fachbereichs Physik
der Universität Hamburg

vorgelegt von
Filip Franco-Sollova
aus México D.F

Hamburg
2006

Gutachter der Dissertation:

Univ. Prof. Dr. Rolf-Dieter Heuer

Gutachter der Disputation:

Univ. Prof. Dr. Peter Schleper

Univ. Prof. Dr. Rolf-Dieter Heuer

Datum der Disputation:

Univ. Frau Prof. Dr. Caren Hagner

28.06.2006

Vorsitzender des Prüfungsausschusses:

Dr. Hans Dierk Rüter

Vorsitzender des Promotionsausschusses:

Prof. Dr. Günter Huber

Dekan der MIN Fakultät:

Prof. Dr. Arno Frühwald

Abstract

The use of beam polarization at the future ILC e^+e^- linear collider will benefit the physics program significantly. This thesis explores three aspects of beam polarization: the application of beam polarization to the study of electroweak processes, the precise measurement of the beam polarization, and finally, the production of polarized positrons at a test beam experiment.

In the first part of the thesis the importance of beam polarization at the future ILC is exhibited: the benefits of employing transverse beam polarization (in both beams) for the measurement of triple gauge boson couplings (TGCs) in the W -pair production process are studied. The sensitivity to anomalous TGC values is compared for the cases of transverse and longitudinal beam polarization at a center of mass energy of 500 GeV. Due to the suppressed contribution of the t-channel ν exchange, the sensitivity is higher for longitudinal polarization.

For some physics analyses the usual polarimetry techniques do not provide the required accuracy for the measurement of the beam polarization (around 0.25% with Compton polarimetry). The second part of the thesis deals with a complementary method to measure the beam polarization employing physics data acquired with two polarization modes. The process of single- W production is chosen due to its high cross section. The expected precision for 500 fb $^{-1}$ and $W \rightarrow \mu\nu$ decays only, is $\Delta P_{e^-}/P_{e^-} = 0.26\%$ and $\Delta P_{e^+}/P_{e^+} = 0.33\%$, which can be further improved by employing additional W -decay channels.

The first results of an attempt to produce polarized positrons at the E-166 experiment are shown in the last part of the thesis. The E-166 experiment, located at the Final Focus Test Beam at SLAC's LINAC employs a helical undulator to induce the emission of circularly polarized gamma rays by the beam electrons. These gamma rays are converted into longitudinally polarized electron-positron pairs. The polarization of the positrons is analyzed by reconvertng them into photons and measuring the transmission asymmetry through a magnetized iron absorber. The analysis of the transmission asymmetry yields the following result for the June 2005 run: $\delta = 0.0073$ and the error is $\Delta\delta = 0.0013$; indicating the presence of positron polarization. The actual degree of polarization is still under study by the E-166 collaboration.

Zusammenfassung

In dieser Arbeit werden drei Aspekte von Strahlpolarisation am zukünftigen ILC, einem linearen e^+e^- Beschleuniger mit mindestens 500 GeV Schwerpunktsenergie, besprochen: der positive Einfluss auf elektroschwache Messungen, eine neue Methode zur Messung der Polarisation und die Analyse von Daten eines Testexperimentes zur Erzeugung polarisierter Positronen.

Im ersten Teil der Arbeit wird eine Analyse der Drei-Eichbosonkopplungen (TGC) in W -Paar Ereignissen am zukünftigen ILC mit 500 GeV Schwerpunktsenergie vorgestellt. Es wird untersucht, inwieweit die Sensitivität auf anomale Anteile zu diesen Kopplungen durch transversale Strahlpolarisation erhöht werden kann. Die Ergebnisse werden mit Studien für longitudinal polarisierte Strahlen verglichen. Die Sensitivität im Falle longitudinal polarisierter Strahlen ist aufgrund einer geringeren Untergrundrate für W -Paarproduktion mit t -Kanal Neutrinoaustausch höher.

Das volle Potential polarisierter Strahlen kann nur ausgeschöpft werden, wenn der Polarisationsgrad sehr genau bekannt ist. Herkömmliche Compton-Polarimeter mit einer Auflösung von etwa 0.25 % sind dabei nicht immer ausreichend. Der zweite Teil dieser Arbeit stellt eine alternative Methode zur Messung der Polarisation vor, die auf der Analyse von Kollisionsdaten bei zwei verschiedenen Polarisationswerten beruht. Insbesondere wird die Produktion einzelner W -Bosonen wegen des hohen Wirkungsquerschnitts untersucht. Mit 500 fb^{-1} und $W \rightarrow \mu\nu$ Zerfällen wird eine Präzision von 0.26 % (0.36 %) für die Elektron-(Positron-)Polarisation erwartet, die durch die Analyse weiterer W -Zerfallskanäle erhöht werden kann.

Im dritten Teil dieser Arbeit werden erste Ergebnisse des E-166 Experiments zur Erzeugung polarisierter Positronen präsentiert. Ein helischer Undulator wird verwendet, um mit Hilfe des SLAC Elektronstrahls zirkular polarisierte Photonen zu erzeugen. Diese wiederum werden in polarisierte e^+e^- Paare konvertiert. Die Positronen werden in Photonen rekonvertiert, deren Transmissionsasymmetrie in einem magnetisierten Eisenabsorber gemessen wird, die wiederum ein Maß für die Polarisation der Positronen ist. Die Analyse der im Juni 2005 genommenen Daten ergibt eine Transmissionsasymmetrie von $\Delta\delta = 0.0073 \pm 0.0013$. Der daraus zu ermittelnde Wert für die Positronpolarisation wird noch von der E-166 Kollaboration untersucht.

Contents

1	INTRODUCTION	1
2	The Standard Model: Theory and Experimental Confirmation	5
2.1	Standard Model of Particle Physics	5
2.2	Gauge Fields	6
2.3	Electroweak Sector of the Standard Model	8
2.4	Single-W and W-pair Production	10
2.5	Physics with Beam Polarization at the ILC	11
2.5.1	Transverse Beam polarization	14
2.5.2	Longitudinal Beam Polarization	14
2.6	Present Status of the SM	17
3	The International Linear Collider	23
3.1	The Cold Technology Based ILC	23
3.2	The Large Detector Concept	27
3.3	Beam Polarization and Polarimetry at the ILC	36
4	TGCs and Transverse Beam Polarization	41
4.1	Triple Gauge Boson Couplings	42
4.2	Transverse Polarization	44
4.3	Monte Carlo Event Generators	48
4.4	Analysis	50
4.4.1	Frame of the Study	50
4.4.2	Fit Method and Construction of Reference Distributions	50
4.4.3	Azimuthal Asymmetry	51

4.5	Results	54
4.6	Systematic Errors	55
4.7	Summary and Conclusion	56
5	Precision Measurements of the Beam Polarization at the ILC Using Single-W Production	59
5.1	Introduction	59
5.2	Single- W Production	60
5.3	Single- W Generators	62
5.4	Measuring the Beam Polarization	64
5.5	Conditions of the Study and Analysis	65
5.6	Results	66
5.7	Systematic Errors	69
5.8	Conclusions	69
6	Polarized Positrons at the E-166 Experiment	73
6.1	Aim of the Experiment	73
6.2	Interaction of Particles with Matter	74
6.3	Polarized Positron Production	76
6.3.1	Production of Circularly Polarized Photons	76
6.3.2	Polarized Positrons Production	80
6.4	Polarimetry at E-166	80
6.5	Structure of the E-166 Experiment	83
6.5.1	Beam Parameters and Background	85
6.5.2	The Helical Undulator	86
6.5.3	The Photon Polarimeter	86
6.5.4	Positron Production and Polarimetry	88
6.6	Data-taking June 2005	91
6.6.1	Data Analysis	91
6.6.2	Results for the Positron Polarimeter Asymmetry Measurements	95
6.6.3	Systematic Errors	98
6.7	Conclusions and Outlook	102
	Summary and Conclusions	103
	Bibliography	105
	Acknowledgements	113
	Appendix A	114
	Appendix B	116

CONTENTS

7

Appendix C	118
Appendix D	119
Appendix E	121

Chapter 1

INTRODUCTION

Historically the development of particle physics has been based on an interplay between experiment and theory. The work of the theoreticians has produced models which describe with high accuracy the experimentally observed behavior of the elementary particles and their interactions. These theories not only model the observed phenomena, but in addition they have predicted new components of the nature never observed before. More specifically, the standard model (SM)¹ of the elementary particles and their interactions predicted the existence of a number of particles which have been discovered as the available energy and luminosity of the particle accelerators has been increasing. A significant example is the discovery of the W^\pm and Z^0 gauge bosons in 1983 at the Super Proton Synchrotron at CERN by the UA1 and UA2 experiments led by Carlo Rubbia and Simon van der Meer respectively. The existence of these particles was predicted by the electroweak model (Glashow-Weinberg-Salam model), which is a component of the SM.

The physics program for the future high energy physics (HEP) experiments is very rich; the SM has to be tested with more precision than the one provided by the experiments at LEP, and even further, the existence of a very important component predicted by the electroweak sector of the SM has to be confirmed, namely, the Higgs boson. Unsatisfactory features of the SM² stimulated the proposal of more fundamen-

¹A description of the SM is given in Chapter 1. A few words on some models beyond the SM are also given on that chapter.

²Actually, the first experimental deviation from the Standard Model was observed in 1998, when Super-Kamiokande published results indicating neutrino oscillations. This fact contradicted the as-

tal theories in which the SM would be a particular case. Supersymmetry (SUSY) is the extension of the SM which has attracted most of physicist's attention. A prediction of Supersymmetry is the expansion of the spectra of elementary particles by assigning a boson partner to every SM fermion and vice-versa. The fact that this supersymmetric partners have not been observed yet suggests very high values of the super-particles' masses (outside of the range of today's existing colliders) and one of the tasks of future colliders is to try to produce such particles and study their properties.

High luminosity and beam energy are without question the most important features of HEP colliders, nevertheless, another powerful tool which ends up being very helpful to obtain deeper and more precise results is beam polarization. The cross section for the physical processes observed at the experiments depend on the polarization of the beam particles; making use of this feature it is possible to enhance the processes of interest or suppress others which make difficult the study of the desired ones. Additionally, some physical properties of the elementary particles and their interactions can be studied only with the aid of polarization. In this thesis results from studies of three complementary aspects of beam polarization at the International Linear Collider (ILC) are presented:

- Use of beam polarization for precision measurements of electroweak processes.
- Precise determination of the degree of electron and positron beam polarization.
- Production of polarized positron beams.

The second chapter introduces the SM of particles and interactions as well as some basic aspects of the effects of beam polarization in the electron-positron annihilation process. A brief description of the SM status closes Chapter 2. The main features of the ILC and its detector are the topic of Chapter 3, paying special attention on the Large Detector Concept (LDC). The fourth chapter presents the results of a study of the sensitivity of the ILC to measure anomalous values of the triple gauge-boson couplings (TGC's) employing transverse beam polarization. The precision of several measurements to be made at the ILC depends largely on how precise is the knowledge of the degree of beam polarization. On Chapter 5 a complementary method (with respect to the usual polarimeter based techniques) to measure precisely the beam polarization at the ILC is exposed. Using this method the degree of beam polarization is obtained from the properties of the physics processes during the analysis. For the study presented in this chapter the single- W production process is used. The last chapter deals with an

sumption of massless neutrinos in the SM (A necessary condition for a neutrino oscillation to occur is a non-zero neutrino mass).

experimental attempt directed to probe the feasibility of producing polarized positrons for their use at the ILC, namely the E-166 experiment which is a multinational project involving DESY among other scientific institutions. The last chapter presents the general conclusions from this multi-aspect study of beam polarization and its application at the ILC.

Chapter 2

The Standard Model: Theory and Experimental Confirmation

The Standard Model (SM) is the theory which has succeeded describing the elementary particles and their interactions (except gravity). In this chapter some basic facts about the SM are introduced. In particular some notions on gauge theories and the formulation of the electroweak theory are discussed. The processes of Single-W and W-pair production, which are employed in the studies described in Chapters 4 and 5, are introduced as well. Beam polarization and its importance at the ILC are highlighted in this chapter too.

2.1 Standard Model of Particle Physics

The SM is a set of quantum field theories which employs the concept of gauge invariance to describe the characteristics of elementary particles and their interactions. The elements conforming the SM are fermions (leptons and quarks) and bosons (interaction fields and the Higgs boson). In the SM the strong interaction experimented by quarks is modeled by quantum chromodynamics (QCD) [1], a gauge theory where the symmetry group is $SU(3)$. The resulting gauge bosons (gluons) are electrically neutral but have an additional “charge”: the quarks come in three different color charges (red, blue and green and the corresponding anticolours). The gluons themselves are colored. The

electroweak theory [2] describes the electromagnetic and weak interactions using the symmetry group $SU(2) \times U(1)$. The electromagnetic interaction is carried by the photon, and three massive gauge bosons are responsible of the weak force: the electrically charged W^\pm bosons and the neutral Z boson. The “charges” of the initially unbroken symmetry theory are the isospin I for the $SU(2)$ sector and the hypercharge Y for the $U(1)$ case. A peculiarity of the weak interaction is the fact that only left-handed fermions can “feel” this force. The gravitational interaction can be neglected in particle physics processes because its strength is at least thirty orders of magnitude smaller than that of the weak interaction.

2.2 Gauge Fields

In this section some concepts of gauge field theories are exposed. To simplify the discussion consider a set of N -coupled scalar fields $\phi(x) = (\phi_1(x), \dots, \phi_N(x))$ and a Lagrangian of the form

$$\mathcal{L}_o = \frac{1}{2}(\partial_\mu \phi) \cdot (\partial^\mu \phi) - V(\phi(x)), \quad (2.1)$$

where $V(\phi(x))$ is the potential function. In the above expression for the Lagrangian \mathcal{L}_o we have

$$(\partial_\mu \phi) \cdot (\partial^\mu \phi) = \sum_{\mu=0}^3 \sum_{i=1}^N (\partial_\mu \phi_i)(\partial^\mu \phi_i).$$

A gauge potential $A_\mu(x)$ has to be introduced to keep the Lagrangian \mathcal{L}_o invariant under the local transformation

$$\phi_i(x) \longrightarrow \phi_i(x)' = U_{ij}(x)\phi_j(x),$$

or suppressing the indices i and j

$$\phi(x) \longrightarrow \phi(x)' = U(x)\phi(x),$$

where $U(x)$ is a unitary transformation matrix belonging to a Lie group G . The matrix $U(x)$ can be written as

$$U(x) = \exp(J_a \varepsilon^a(x)).$$

Here the $\varepsilon^a(x)$ are arbitrary real functions of x and the J_a are the generators of G satisfying

$$[J_a, J_b] = f_{ab}^c J_c,$$

where f_{ab}^c are the totally antisymmetric real structure constants of the Lie group G. In order to construct a Lagrangian \mathcal{L} which is invariant under the local transformation generated by U , the gauge potentials $A_\mu^a(x)$ (one for each generator of the group G) are introduced to form the gauge-covariant derivative

$$D_\mu = (\partial_\mu + gJ_a A_\mu^a),$$

which replaces ∂_μ in equation (2.1). Here, g is the coupling constant of the theory. The Lagrangian \mathcal{L} will remain invariant if $D_\mu\phi$ transforms as

$$D_\mu\phi \longrightarrow (D_\mu\phi)' = UD_\mu\phi.$$

This holds provided A_μ^a transforms in the following way

$$J_a A_\mu^a = U(J_a A_\mu^a)U^{-1} - \frac{1}{g}(\partial_\mu U)U^{-1}. \quad (2.2)$$

The gauge potential A_μ is defined as $A_\mu \equiv gA_\mu^a J_a$; it takes values in the Lie algebra of the group G. In this notation (2.2) can be written as $A'_\mu = UA_\mu U^{-1} - (\partial_\mu U)U^{-1}$. The field strength tensor $F_{\mu\nu}$ is constructed using the matrix valued gauge potential A_μ as

$$F_{\mu\nu} \equiv \partial_\mu A_\nu - \partial_\nu A_\mu + [A_\mu, A_\nu],$$

or in component form

$$F_{\mu\nu}^a \equiv \partial_\mu A_\nu^a - \partial_\nu A_\mu^a + g\epsilon^{abc} A_\mu^b A_\nu^c.$$

The relation between $F_{\mu\nu}$ and $F_{\mu\nu}^a$ is: $F_{\mu\nu} = gJ_a F_{\mu\nu}^a$. From the fact that $F_{\mu\nu}$ can be written as

$$F_{\mu\nu} \equiv [D_\mu, D_\nu], \quad (2.3)$$

and from the transformation law $(D_\mu\phi)' = UD_\mu\phi$, one can see that the field strength tensor $F_{\mu\nu}$ transforms in the following way: $F'_{\mu\nu} = UF_{\mu\nu}U^{-1}$. This implies that the product $\text{Tr}[F_{\mu\nu}F^{\mu\nu}] = \frac{1}{2}F_{\mu\nu}^a F^{a\mu\nu}$ is gauge invariant. It contains derivatives of A_μ , and therefore it becomes the Lagrangian $\mathcal{L}_{gauge} = -\frac{1}{4}F_{\mu\nu}^a F^{a\mu\nu}$ for the potentials A_μ . When it is added to the Lagrangian \mathcal{L} , we obtain the complete gauge invariant Lagrangian \mathcal{L}' :

$$\mathcal{L}' = \mathcal{L} + \mathcal{L}_{gauge} = \frac{1}{2}(D_\mu\phi) \cdot (D^\mu\phi) - V(\phi(\mathbf{x})) - \frac{1}{4}F_{\mu\nu}^a F^{a\mu\nu}.$$

2.3 Electroweak Sector of the Standard Model

In the description of the electroweak (EW) sector of the SM the following experimental facts must be considered:

- The weak interaction mediators couple only to left-handed fermions, while the photon couples to both: left and right.
- Only left handed neutrinos and right handed antineutrinos have been observed.
- It was well established in old four-fermionic theory of weak interactions that charged currents (responsible for β -decay of nucleons and other hadrons) have $V - A$ structure, i.e. they are constructed from the left-handed fermions.

In order to cope with these facts it is convenient to express the Dirac spinors Ψ as the sum of two Weil spinors: $\Psi = \Psi_L + \Psi_r$ where $\Psi_{L,R} = [(1 \mp \gamma_5)/2]\Psi$. The standard EW theory is a chiral theory, in the sense that Ψ_L and Ψ_R behave differently under the gauge group. The minimal group of gauge symmetry which includes charged vector currents is $SU(2)$ group. Consequently, the group of gauge symmetry of a unifying theory of the weak and electromagnetic interactions should be conformed by such group as well as by $U(1)$ (the simplest choice is the group $G = SU(2)_L \times U(1)$). In the minimal SM left-handed fermions are arranged in weak isodoublets, while the righthanded fermions are weak isosinglets. For simplicity consider a lepton isodoublet $\Psi_L = \begin{pmatrix} \nu_L \\ l_L \end{pmatrix}$ and the singlet $\Psi_R = l_R$. The massless symmetric Lagrangian for the $SU(2)_L \times U(1)_Y$ theory can be written in the form (for the general case a sum over all flavors of quarks and leptons must be considered):

$$\mathcal{L}_{sym} = -\frac{1}{4}W_{\mu\nu}^A W^{A\mu\nu} - \frac{1}{4}B_{\mu\nu} B^{\mu\nu} + \bar{\Psi}_L i\gamma^\mu D_\mu \Psi_L + \bar{\Psi}_R i\gamma^\mu D_\mu \Psi_R \quad (2.4)$$

where $B_{\mu\nu}$ is the gauge tensor constructed out of the gauge field B_μ associated with $U(1)$ and $W_{\mu\nu}$ is the $SU(2)$ gauge tensor (see Section 2.2). The structure constant ϵ_{ABC} for the $SU(2)$ group is the totally antisymmetric Levi-Civita tensor. The covariant derivatives are explicitly given by:

$$D_\mu = \partial_\mu - ig_2 T_A W_\mu^A - ig_1 \frac{Y}{2} B_\mu. \quad (2.5)$$

Here T_A and Y are the generators of the $SU(2)$ and $U(1)$ groups respectively, and the corresponding gauge fields are: W_μ^A and B_μ . The symmetry of the Lagrangian

is spontaneously broken giving rise to an additional field: the Higgs boson¹. In the broken symmetry Lagrangian the physical gauge bosons are expressed as combinations of W_μ^A and B_μ :

$$W_\mu^\pm = \frac{1}{\sqrt{2}}(W_\mu^1 \mp iW_\mu^2), \quad Z_\mu = \frac{g_2 W_\mu^3 - g_1 B_\mu}{\sqrt{g_2^2 + g_1^2}}, \quad A_\mu = \frac{g_2 W_\mu^3 + g_1 B_\mu}{\sqrt{g_2^2 + g_1^2}}. \quad (2.6)$$

The following bilinear terms appear in the new effective Lagrangian:

$$M_W^2 W_\mu^+ W^{-\mu}, \quad M_Z^2 Z_\mu Z^\mu, \quad M_A^2 A_\mu A^\mu, \quad (2.7)$$

The W and Z bosons have acquired masses, while the photon remains massless:

$$M_W = \frac{1}{2}vg_2, \quad M_Z = \frac{1}{2}v\sqrt{g_2^2 + g_1^2}, \quad M_A = 0, \quad (2.8)$$

Here v is the vacuum expectation value of the Higgs field. The fermions acquire their masses by the same mechanism. In the neutral-current sector, the photon and the Z boson are orthogonal and normalized linear combinations of B_μ and W_μ^3 :

$$A_\mu = \cos \theta_W B_\mu + \sin \theta_W W_\mu^3 \quad (2.9)$$

$$Z_\mu = -\sin \theta_W B_\mu + \cos \theta_W W_\mu^3. \quad (2.10)$$

This relations define the weak mixing angle θ_W , which is related to g_1, g_2 and the positron charge e as follows:

$$g_2 \sin \theta_W = g_1 \cos \theta_W = e, \quad \tan \theta_W = g_1/g_2. \quad (2.11)$$

The nonabelian nature of the $SU(2)$ group induces self interactions between the gauge fields, in particular, the Lagrangian for triple gauge bosons couplings (TGCs) has the form:

$$\mathcal{L}_{TGC} = ig_2 \sin \theta_W \left[(W_{\mu\nu}^- W^{+\mu} - W_{\mu\nu}^+ W^{-\mu}) A^\nu + A_{\mu\nu} W^{-\mu} W^{+\nu} \right] \quad (2.12)$$

$$+ ig_2 \cos \theta_W \left[(W_{\mu\nu}^- W^{+\mu} - W_{\mu\nu}^+ W^{-\mu}) Z^\nu + Z_{\mu\nu} W^{-\mu} W^{+\nu} \right] \quad (2.13)$$

A more general form of \mathcal{L}_{TGC} will be introduced in Chapter 4 with the aim of modeling possible deviations from the SM. A particular property of the electroweak interaction

¹The formalism of the Higgs mechanism is addressed in most modern QFT and particle physics books.

is the occurrence of CP-symmetry violation, i.e. the breaking of the invariance of physics processes under the simultaneous inversion of charge and parity. CP violation has its own importance in cosmology because it is an ingredient of a mechanism which attempts to explain the excess of matter over antimatter in the universe, although the amount of CP violation provided by electroweak phenomena is not enough to explain the presence of the observable matter in the universe.

2.4 Single-W and W-pair Production

Single-W and W-pair production are particularly interesting processes because they reflect the nonabelian structure of the electroweak sector of the SM as indicated in Section 2.3. At the same time they can be sensible to phenomena beyond the SM. Single-W (Fig. 2.1) and W-pair production (Fig. 2.2) manifest themselves as contributions to events where the final state is constituted by 4 fermions. The cross section for Single-W and W-pair production together with other SM processes is shown in Fig. 2.4. The contributions to four fermion final states can be classified in the

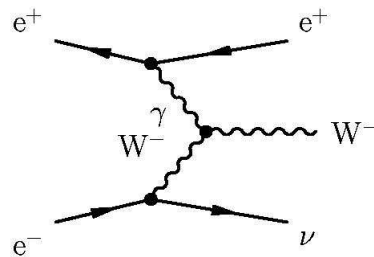


Figure 2.1: Diagrams for the single- W production process.

six types of diagrams shown in Figure 2.3. The *multiperipheral diagrams* provide the largest contribution to the cross section of some 4 fermion final states (which represent a source of background for missing energy/momentum events) [3]. Relevant for electroweak physics measurements are the nonabelian classes of diagrams; these processes contribute to W , Z and Higgs boson production.

The main contribution to W -pair production comes from the *conversion* and *annihilation* diagrams (Fig. 2.2), where the *annihilation* diagram, containing the TGC vertex is appropriate for testing the nonabelian structure of the SM. The *fusion* TGC vertex is the principal diagram for single- W production (Fig. 2.1).

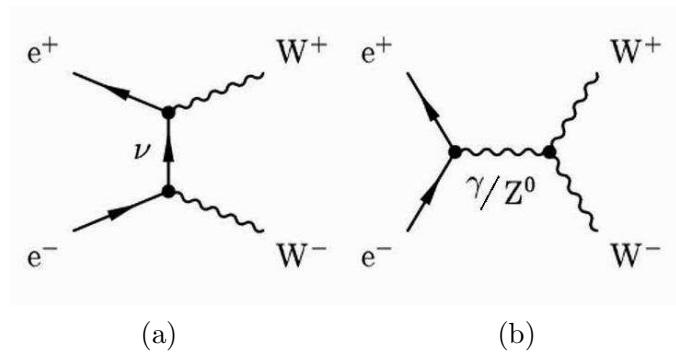


Figure 2.2: Diagrams for the W -pair production process.

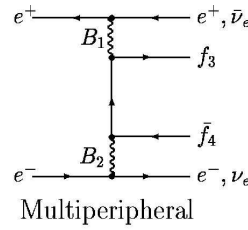
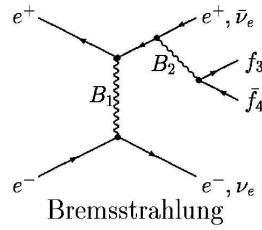
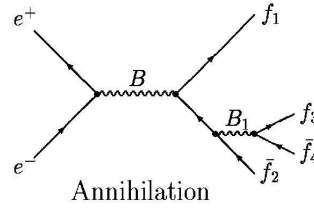
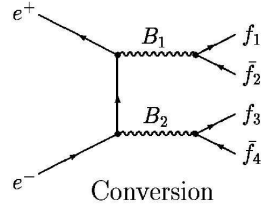
2.5 Physics with Beam Polarization at the ILC

This section sketches the role of beam polarization in the ILC physics programme. Production of polarized beams and polarimetry are topic of Section 3.3, and in particular, Chapter 6 presents the first results of the experiment E-166, whose aim is to test a method to produce polarized positrons. The benefits of electron and positron beam polarization are in general terms:

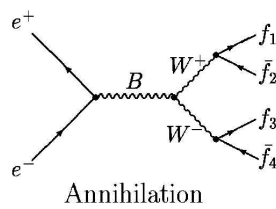
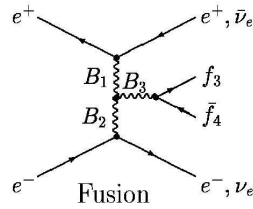
- The precision of the measurements is significantly increased in many cases.
- Some analysis can not be carried out unless the beams are polarized.
- As mentioned in Section 2.4 the events' final states receive contributions from different processes. Such contributions can be individually analyzed with the aid of beam polarization.

The idea of using beam polarization in a lepton collider experiment has been already applied at the SLD experiment at the SLAC Linear Collider (SLC) [61]. SLD studied e^+e^- collisions at the Z -resonance employing electron beam polarization of 75%. This degree of electron polarization provided an improvement in statistical power of approximately a factor 25 for many Z -pole asymmetry observables. Electron beam polarization allowed the SLD experiment to make the best individual measurement of the weak mixing angle. In the case of the ILC polarization in both beams is foreseen (80% electron beam polarization and 60% positron beam polarization). A comprehensive study of the role of electron and positron beam polarization at the ILC is presented in [5]. Two categories of beam polarization will be discussed next: transverse and longitudinal.

Abelian Classes



Nonabelian Classes



($B = Z^0, \gamma$; $B_1, B_2, B_3 = Z^0, \gamma, W^\pm$; + Higgs Graphs.)

Figure 2.3: Four fermion production classes of diagrams [3].

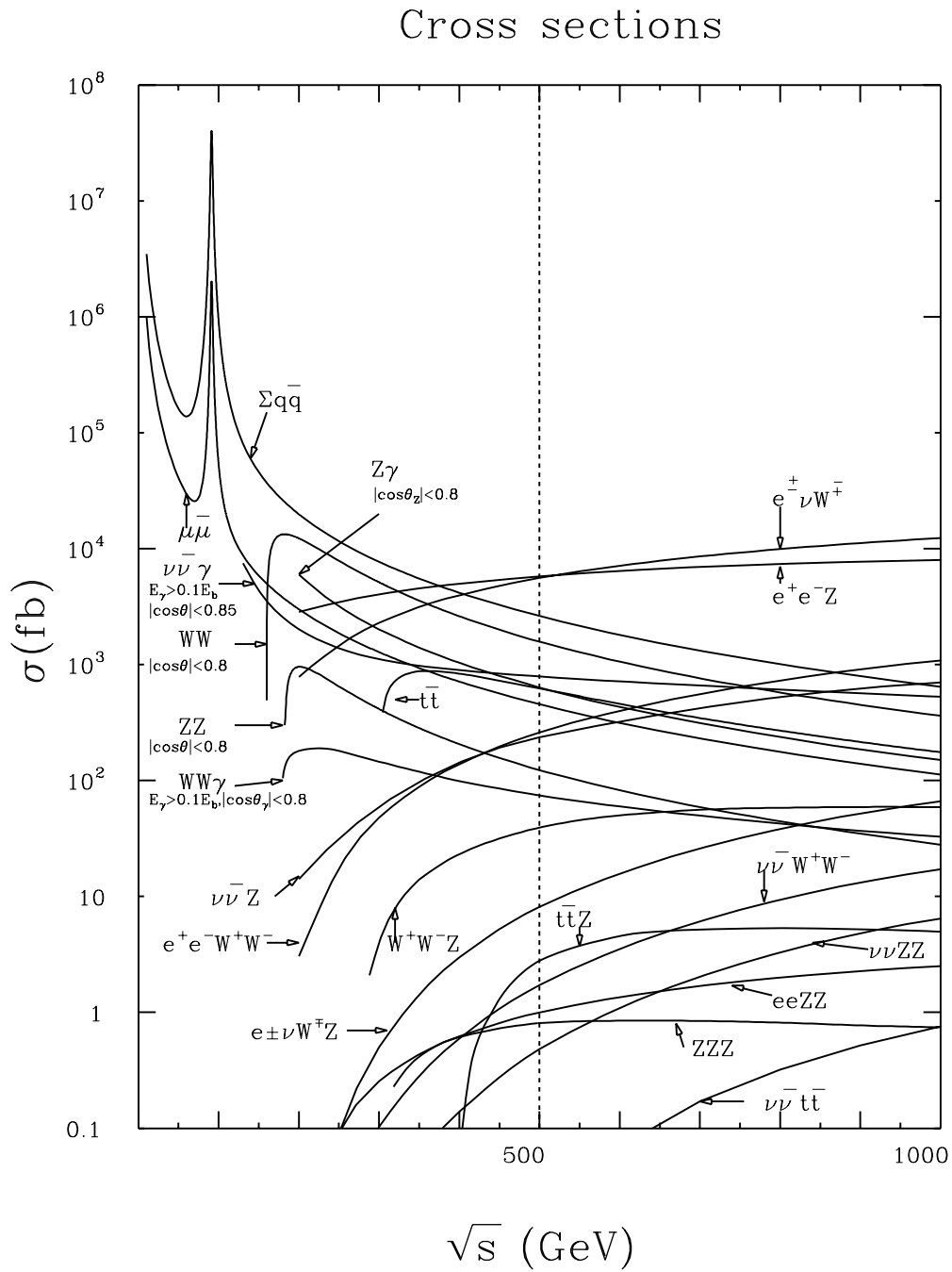


Figure 2.4: Cross section for Single-W, W-pair production and other SM processes [4].

2.5.1 Transverse Beam polarization

At the ILC the longitudinal beam polarization can be reoriented with the help of spin rotators in order to achieve transverse polarization. A proposed spin rotation scheme for the ILC is described in [6]. Spin rotators have been used at HERA to achieve the opposite effect: the natural transverse polarization acquired by the leptons at the storage ring is converted into longitudinal polarization [33]. Some of the phenomena where transverse beam polarization plays an important role are (see Table 2.1):

- TGCs and longitudinal W -bosons.
- CP-sensitive observables in chargino and neutralino production.
- Extra dimensions.

In Chapter 4 a study of TGCs and longitudinal W -bosons employing transverse beam polarization at the ILC [7] is discussed.

2.5.2 Longitudinal Beam Polarization

Four ideal cases of longitudinally polarized beams cross sections, σ_{LL} , σ_{LR} , σ_{RL} and σ_{RR} are listed in Fig. 2.5. Here σ_{LL} denotes the cross section for 100% left-handed electron polarization and 100% left-handed positron polarization. The same scheme applies for defining σ_{LR} , σ_{RL} and σ_{RR} . A general expression $\sigma(P_{e^-}, P_{e^+})$ for the cross section for an arbitrary degree of longitudinal beam polarization can be written as:

$$\begin{aligned} \sigma(P_{e^-}, P_{e^+}) = \frac{1}{4} & \left\{ (1 + P_{e^-})(1 + P_{e^+})\sigma_{RR} + (1 - P_{e^-})(1 - P_{e^+})\sigma_{LL} \right. \\ & \left. + (1 + P_{e^-})(1 - P_{e^+})\sigma_{RL} + (1 - P_{e^-})(1 + P_{e^+})\sigma_{LR} \right\}. \end{aligned} \quad (2.14)$$

where P_{e^-} and P_{e^+} denote the electron and positron beam polarization respectively.

The influence of beam polarization on a given process can be inferred from one of the two classes of diagrams in which the process can be divided:

Annihilation diagrams. In this case the helicities of the incoming beams are coupled to each other. In the SM only the recombination into a vector particle with total angular momentum $J = 1$ is permitted (see Fig. 2.5), therefore, processes where the incoming particles have the same helicities can not occur (only σ_{RL} and σ_{LR} contribute to the cross section in the expression 2.15).

	e^-	e^+		
σ_{RR}			$\frac{1+P_{e^-}}{2}, \frac{1+P_{e^+}}{2}$	$J_z = 0$
σ_{LL}			$\frac{1-P_{e^-}}{2}, \frac{1-P_{e^+}}{2}$	
σ_{RL}			$\frac{1+P_{e^-}}{2}, \frac{1-P_{e^+}}{2}$	$J_z = 1$
σ_{LR}			$\frac{1-P_{e^-}}{2}, \frac{1+P_{e^+}}{2}$	

Figure 2.5: Spin configurations in e^+e^- collisions with longitudinal beam polarization. The second and third columns show the particle's direction of motion (internal arrow) and the spin direction (double arrow). The fourth column indicates the fraction of particles with this configuration when the polarization of the incoming beams is (P_{e^-}, P_{e^+}) . The total spin projection is shown in the fifth column.

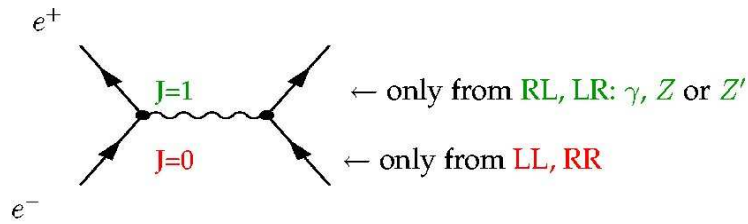


Figure 2.6: Diagram for e^+e^- annihilation. In the SM only incoming particles with opposite helicities can produce this kind of reaction ($J = 1$).

Exchange diagrams. In this case all helicity combinations are possible. The exchanged particle can be vector, fermion or scalar and the incoming particle is directly coupled to the vertex (see Fig. 2.5).

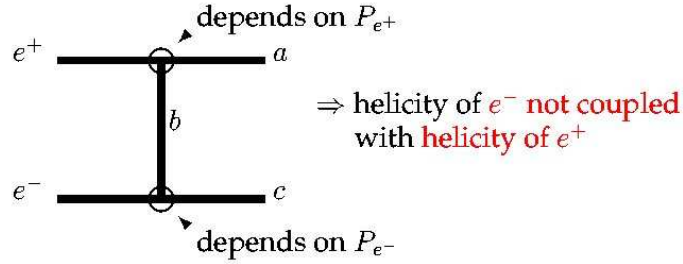


Figure 2.7: In these events the helicity of the incoming particle is independent of the helicity of the second incoming particle.

The study described in Chapter 5 employs single- W^- and single- W^+ production (Fig. 2.1) an exchange diagram process, taking advantage of the fact that single- W^- (single- W^+) production is independent of the positron (electron) beam polarization.

Case	Effects	Gain& Essentiality
SM:		
top threshold	Improvement of coupling measurement	factor 3
$t\bar{q}$	Limits for FCN top couplings reduced	factor 1.8
CPV in $t\bar{t}$	Azimuthal CP-odd asymmetries give access to S- and T-currents up to 10 TeV	$P_{e^-}^T P_{e^+}^T$ required
W^+W^-	Enhancement of $\frac{S}{B}, \frac{-S}{\sqrt{B}}$	up to a factor 2
	TGC: error reduction of $\Delta\kappa_\gamma, \Delta\lambda_\gamma, \Delta\kappa_Z, \Delta\lambda_Z$	factor 1.8
	Specific TGC $\tilde{h}_+ = \text{Im}(g_1^R + \kappa^R)/\sqrt{2}$	$P_{e^-}^T P_{e^+}^T$ required
CPV in γZ	Anomalous TGC $\gamma\gamma Z, \gamma ZZ$	$P_{e^-}^T P_{e^+}^T$ required
HZ	Separation: $HZ \leftrightarrow H\nu\nu$	factor 4 with RL
	Suppression of $B = W^+\ell^-\nu$	factor 1.7

Table 2.1: Examples of gains in the precision of the measurements when using positron polarization (80%,60%) compared to the pure electron polarization (80%,0%). B (S) denotes background (signal); CPV (RPV) means CP (R-parity) violation. [5].

As previously mentioned, beam polarization helps to reduce the influence of the background processes. Here two cases can be distinguished: a) The signal increases with polarization while the background is suppressed (the benefit is straightforward). b) Both, signal and background depend on polarization in a similar way. In order to estimate the statistical gain when using beam polarization the change in the signal to background ratio S/B has to be considered as well as the ratio S/\sqrt{B} . The first example in Table 2.8 is an instance of situation a), where the use of polarization increases the signal by a factor 2 and reduces the background by $1/2$. The second case exemplifies situation b), both, signal and background are incremented by a factor 2. In this case S/B remains constant, but the statistical significance of the signal is increased by a factor: $\sqrt{2}$.

	S	B	S/B	S/\sqrt{B}
Example 1	$\times 2$	$\times 0.5$	$\times 4$	$\times 2\sqrt{2}$
Example 2	$\times 2$	$\times 2$	Unchanged	$\times \sqrt{2}$

Figure 2.8: The gain in signal over background, S/B , and in S/\sqrt{B} , when the background and signal processes have the same (Example 1) or an inverse scaling (Example 2). factor.

2.6 Present Status of the SM

The masses of the elementary particles and the coupling constants corresponding to the fundamental interactions are free parameters in the SM. This quantities have to be determined experimentally, however, in the electroweak theory the weak coupling is related to the electromagnetic coupling and to the masses of the W and Z bosons. As a result, it is enough to determine the electromagnetic and the strong interaction couplings, α and α_s respectively, as well as the masses of the W and Z bosons. In this section some examples of experimental results supporting the validity of the SM predictions are presented. The combination of the many precise electroweak results yields stringent constraints on the Standard Model. Using this results it has been possible to constrain the value of the SM Higgs' mass. Measurements of the top quark also contribute to set bounds on this quantity. A very important result is the constraint on the number of light neutrino types, N_ν [11, 9, 12]. The values of the Z resonance's partial and total widths were measured at LEP. The invisible partial width Γ_{inv} , was

determined by subtracting the measured visible partial widths, corresponding to Z decays into quarks and charged leptons, from the total Z width. The invisible width is assumed to be due to N_ν light neutrino species each contributing the neutrino partial width Γ_ν as given by the Standard Model. The combined result from the four LEP experiments is $N_\nu = 2.984 \pm 0.008$ [9, 13] (see Fig. 2.9).

In the SM the masses of the W , the top quark, and the Higgs are related through

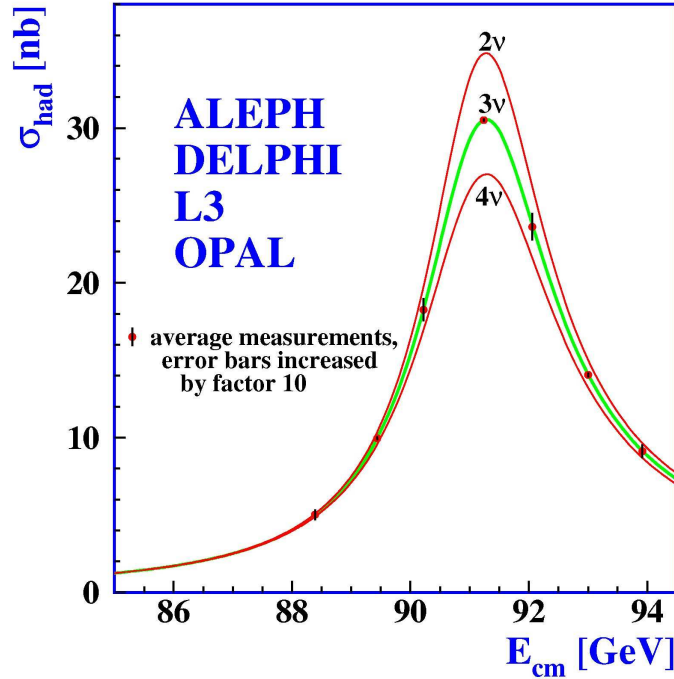


Figure 2.9: Predicted hadron production cross section for two, three and four neutrino species with SM couplings and negligible mass. [8].

loop corrections. Precision measurements of the masses of the W and the top quark provide an estimate of the mass range for the Higgs boson. The measured value of the mass of the W boson is $80.404 \pm 0.03 \text{ GeV}/c^2$ [14]. Fig. 2.10 shows the value of the W boson mass obtained by different experiments as well as the average. Upper and lower bounds for the mass of the Higgs boson have been established by several experiments.

A new measurement of the top quark mass obtained in 2004 by the $D\bar{O}$ experiment ($179.0 \pm 5.1 \text{ GeV}/c^2$) was combined with results of the CDF experiment to yield a new world average of $178.0 \pm 4.3 \text{ GeV}/c^2$ [15, 16]. This result shifts the best-fit value

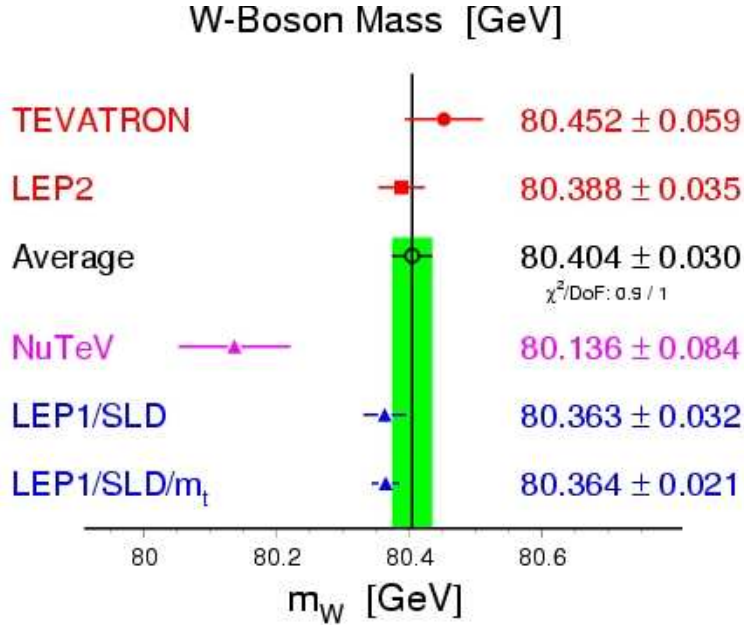


Figure 2.10: Mass of the W boson measured by different experiments [14].

of the expected Higgs mass outside the experimentally excluded region ($114.4 \text{ GeV}/c^2$ with a confidence level (C.L.) of 95%). The previous value of the expected Higgs mass was $96 \text{ GeV}/c^2$ and the new is $117 \text{ GeV}/c^2$, the upper limit on the Higgs mass at the 95% confidence level changes from $219 \text{ GeV}/c^2$ to $251 \text{ GeV}/c^2$ (see Fig. 2.11).

The measurement of the weak mixing angle by the SLD Experiment at SLAC is interesting in the context of this thesis because it shows the advantages of using beam polarization for electroweak measurements. The SLD Z -factory collected over half a million Z particles between 1992 and 1998, obtaining the most accurate measurement of the weak mixing angle: $\sin^2 \theta_W^{eff} = 0.23098 \pm 0.00026$ [8] (see Fig. 2.12). This value was obtained by measuring the left-right asymmetry $A_{LR} = (\sigma_L - \sigma_R)/(\sigma_L + \sigma_R)$, where $\sigma_L(\sigma_R)$ is the Z production cross section measured employing left(right)-handed electrons. Although the amount of data recorded by SLD is much smaller than that of LEP (about 17 million Z events) the presence of longitudinal beam polarization provides complementary competitive measurements. The A_{LR} measurement is a very important contribution to the determination of the Higgs' mass.

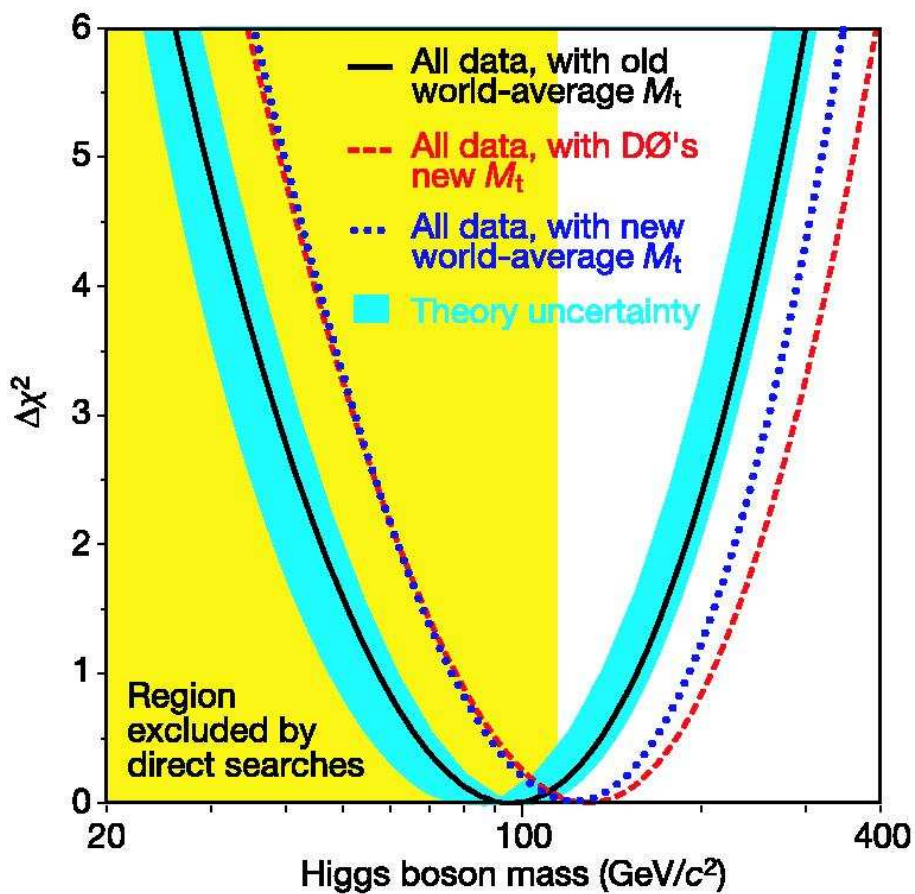


Figure 2.11: The plot shows the χ^2 for a global fit to electroweak data is shown as a function of the Higgs mass. The yellow shaded area on the left indicates the region of Higgs masses excluded by experiment (114.4 GeV/c² at the 95 % confidence level) [15].

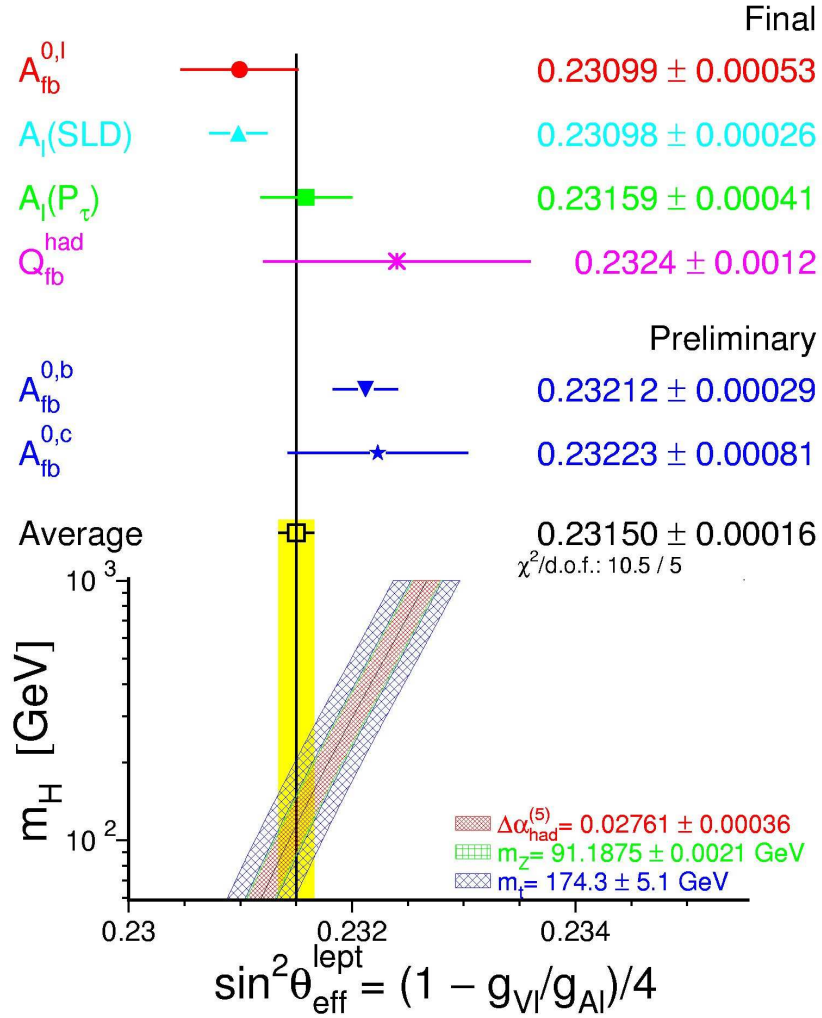


Figure 2.12: Determinations of $\sin^2 \theta_{eff}$ from asymmetries. Also shown is the prediction of the SM as a function of the Higgs' mass m_H . The width of the SM band is due to the uncertainties in the hadronic vacuum polarization $\alpha_{had}^{(5)}(m_Z^2)$, the Z mass m_Z and the top quark mass m_t . The total width of the band is the linear sum of these effects. [13].

Chapter 3

The International Linear Collider

3.1 The Cold Technology Based ILC

The main motivations for a high energy e^+e^- linear collider are: the necessity of high energy and luminosity to make searches and precision measurements of SM physics and beyond, and the limitations of circular colliders to reach practicable high energy collisions. The envisaged center of mass energy for the ILC can be adjusted between 200 and 500 GeV with the possibility of an upgrade to 1 TeV. High statistical precision is to be provided by a luminosity around $3 \times 10^{34} \text{ cm}^{-2} \text{ s}^{-1}$. As outlined in Chapter 2, beam polarization will enhance the physics potential significantly. For the electron beam the degree of polarization will be of at least 80% and for the positron beam a polarization of about 60% is expected. The relative simplicity of the e^+e^- annihilation events at the ILC makes the linear collider the perfect tool to explore the properties of particles which might be discovered by the LHC. In addition to direct searches, the ILC can make discoveries by means of indirect searches because of its sensitivity to quantum effects.

The ILC will be based on superconducting RF technology following the recommendation of the International Technology Recommendation Panel (ITRP) presented in 2004 [17]. The accelerator cavities made of niobium (operated at $2^\circ K$) will be driven by 1.3 GHz radio-frequency reaching a gradient of 31.5 MV/m. This superconducting technology has been successfully developed at the TESLA Test Facility (TTF) in an in-

ternational collaboration at DESY and will be employed in the European X-Ray Laser Project XFEL [19]. The tentative layout of the linear collider is shown in Fig. 3.1. The proposed length for the initial stage of the ILC is approximately 26 km [20]. Each one of the main linear accelerators will contain roughly ten-thousand 1 m long superconducting cavities, each one constituted by 9 cells (see Fig 3.2). The planned beam size at the interaction point (IP) will be 553×5 nm; the main beam parameters are listed in Table 3.1.

PARAMETER	UNITS	VALUE
RF Frequency	GHz	1.3
Repetition Rate	Hz	5
N.of Bunches/Train		2820
Bunch Spacing	ns	337
Bunch Charge	N_e	2×10^{10}
Beam size at IP (σ_x, σ_y)	nm	553, 5

Table 3.1: ILC main beam parameters.

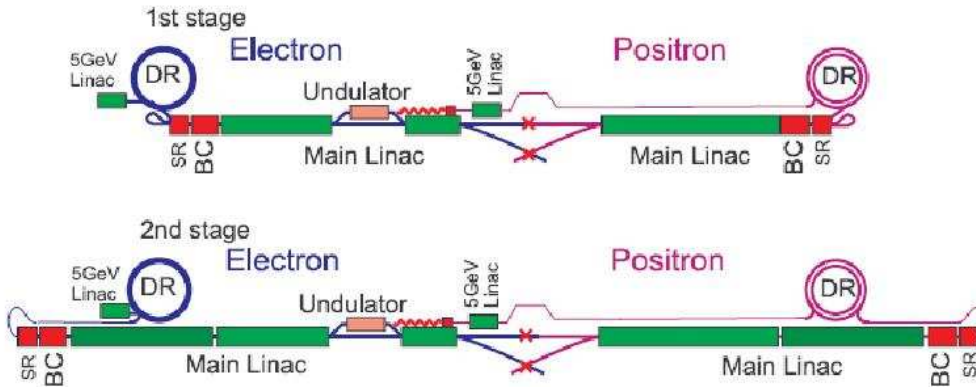


Figure 3.1: Layout of the ILC. During the first stage it will reach a center of mass energy of 500 GeV, and on the second stage the energy is to be increased to about 1 TeV.

The polarized electron beam will be created by illuminating a GaAs/GaAsP photo cathode with a Ti:Sapphire drive laser. The electron bunches are divided into smaller

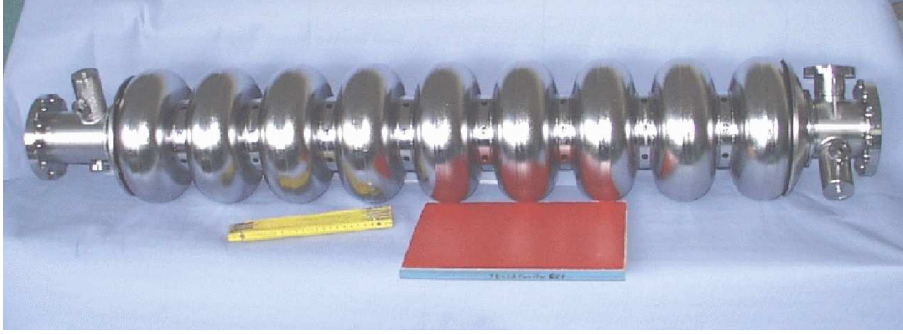


Figure 3.2: The ILC 1 m long niobium superconducting cavity.

bunches, and then are accelerated in a room-temperature linac to an energy of approximately 100 MeV. The electrons are further accelerated employing standard ILC superconducting accelerating module to an energy of 5 GeV before being injected into the damping ring. There, the beam emittance is reduced to the small values required by the ILC via the combination of synchrotron radiation in the bending fields and the energy gain in RF cavities. The 17 km damping ring proposed in [21] shares the same tunnel as the main linac in order to reduce costs. Recent developments on fast kicker magnets permit to consider alternative shorter external damping rings of 6 km for the electron beam and two 6 km rings for the positron beam due to its higher emittance. More details on the polarized electron and positron sources are given in Section 3.3

High luminosity at the ILC is achieved by the small size of the electron and positron bunches. The high density of particles in each bunch leads to energy loss by means of the beamstrahlung effect (the particles emit hard synchrotron radiation in the strong electromagnetic space-charge field of the opposing bunch) according to:

$$\delta_E \approx 0.86 \frac{r_e^3 N_e^2 \gamma}{\sigma_z (\sigma_x^* + \sigma_y^*)^2}, \quad (3.1)$$

where r_e is the classical electron radius, N_e is the number of particles per bunch, γ is the relativistic factor $\gamma = E_{beam}/m_0 c^2$, σ_z is the bunch length and σ_x^* (σ_y^*) is the horizontal (vertical) beam size at interaction point. The consequences of beamstrahlung are a reduction and spread of the collision energy as well as background contamination in the detector (see Fig. 3.3). Another issue to be considered in the design of the ILC concerns the crossing angle of the primary beams. A beam crossing angle at the interaction point is the solution to the complications arising from the case of head

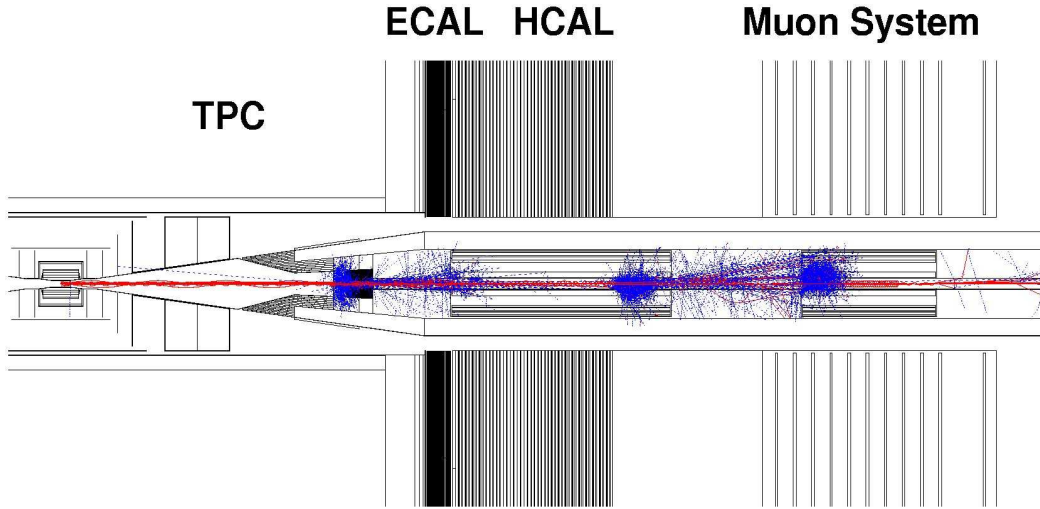


Figure 3.3: Simulation of a fraction of electron-positron pairs generated by beamstrahlung photons hitting the mask elements (The forward detector in this figure corresponds to the old design, the new design is discussed in Section 3.2).

on collisions: a) The beam extraction becomes difficult because the optics must be shared by the incoming and outgoing beams. b) The incoming beam is affected by the beamstrahlung radiation. The possibility of having two interaction points with two detectors is considered, one with a crossing angle of 2 mrad and the other of 20 mrad. A drawback of having a crossing angle is the loss of luminosity because of the orientation of the colliding bunches. This effect must be compensated by “rotating” the bunches by means of an electric field. The beam polarization is unaffected by this procedure. The precision required for the physics programme at the ILC requires a very good knowledge of both beam energies. As an example, the measurement of the top quark mass with an error of less than 100 MeV requires a beam energy precision $\Delta E/E \leq 10^{-4}$. The energy measurements can be accomplished by a magnetic spectrometer similar to the one proposed in [22] (see Fig. 3.4). The field of the spectrometer magnet has to be known to a precision of $\Delta B/B \leq 3 \times 10^{-5}$. Three beam position monitors (BPMs) located on each side of the spectrometer magnet (the circles on Fig. 3.4) must measure the beam deflection angle θ with high precision in order to get the beam energy from:

$$E_{beam} = \frac{ec \int B dl}{\theta} \quad (3.2)$$

The magnetic spectrometer could be installed in the final focus beam line. If BPMs

with a resolution of the order of 100 nm are implemented it would be feasible to have an energy resolution $\Delta E/E \approx 10^{-4}$. The ILC is expected to accumulate an integrated luminosity of 500 fb^{-1} in four years reaching a maximum center of mass energy (CME) of 500 GeV. After this period an upgrade to a CME of 1 TeV is planned, expecting to accumulate a luminosity of 1 ab^{-1} in 3 to 4 years.

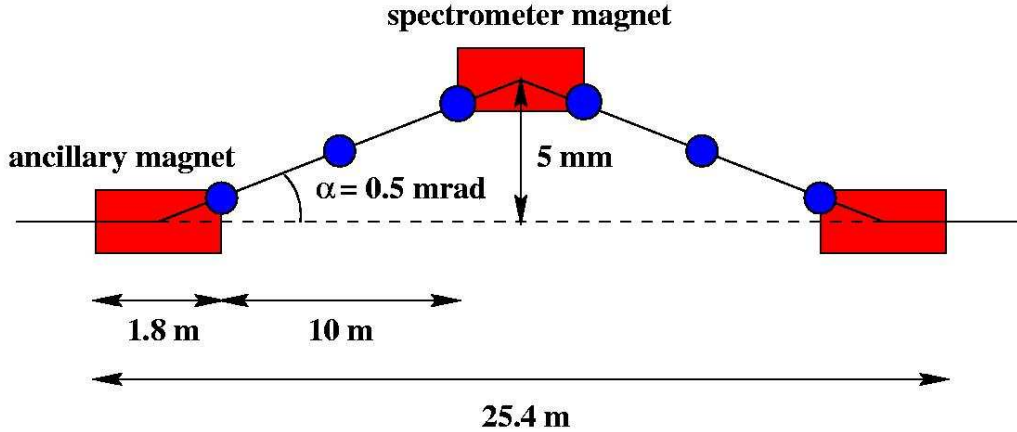


Figure 3.4: The ILC magnetic spectrometer should measure the energy of both beams with a precision $\Delta E/E \approx 10^{-4}$

3.2 The Large Detector Concept

The design of the detector for the ILC assumes particle flow as the conceptual model for event reconstruction. Particle flow implies the reconstruction of the four-vectors of all final state particles belonging to one event. When applying the particle flow algorithms photons are measured by the electromagnetic calorimeter, charged hadrons by the tracker, and neutral long-living hadrons by the hadronic calorimeter, which also is used to tag muons. In addition, lepton identification down to low momenta is important in order to separate purely hadronic jets from jets containing leptonic decays. Currently there are three detector concepts for the ILC under study, in this thesis the attention is focused to the Large Detector Concept (LDC) [18]. A brief description of the three detector concepts is given in Table 3.2. The desired properties for the detector according to the physics requirements and the proposed solution are listed in Table 3.3. The design of the detector for the ILC is dictated by the complexity of the events resulting from the high energy and luminosity e^+e^- collisions (events with

more than eight parton final states are expected). The concept of the LDC detector inherits from the TESLA detector concept as proposed in the TESLA technical design report (TDR) [22]. Fig. 3.5 shows the structure of the LDC; a time projection chamber and the electromagnetic and hadronic calorimeters are contained inside a coil which will provide a 4 T magnetic field. A vertex detector and a system of forward region detectors are also included in the design. The main subdetectors of the LDC are described below.

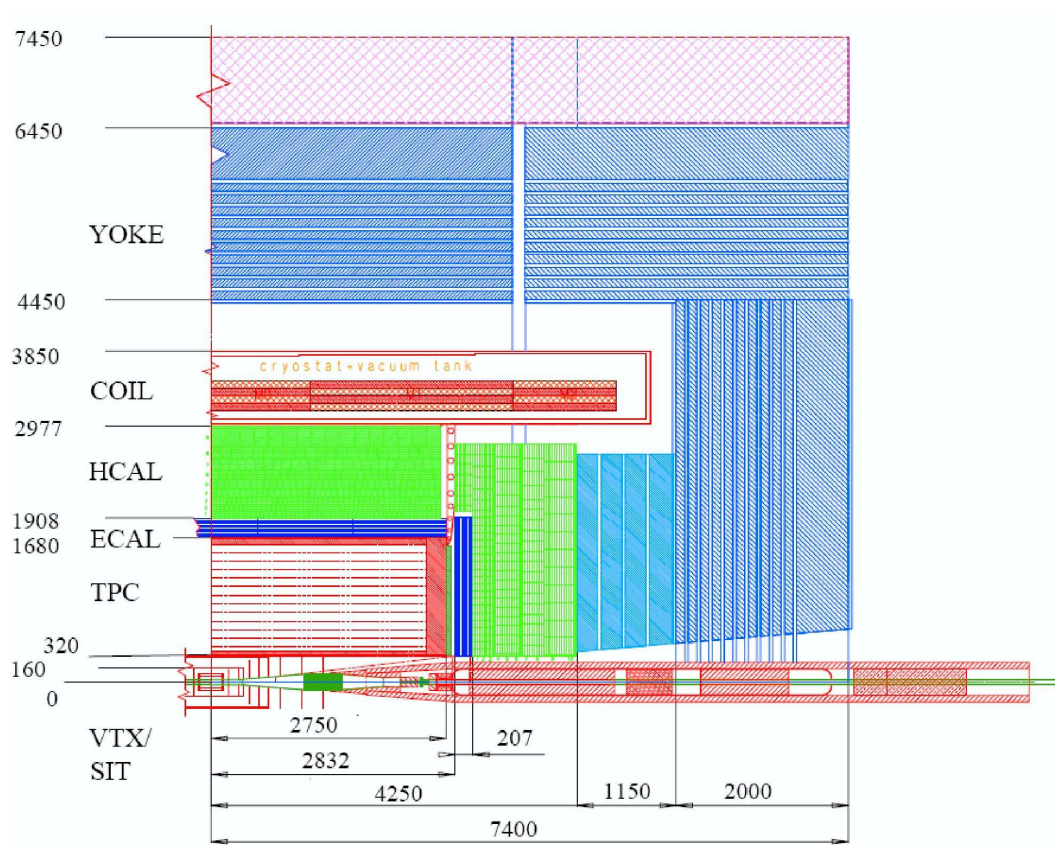


Figure 3.5: One quadrant of the TESLA detector. Dimensions are given in mm. The components of the detector are described in the text.

Tracking System

Five sub-detectors conform the tracking system: A time projection chamber (TPC) ($r=170$ cm, $L=2 \times 273$ cm), a pixel micro-vertex detector (VTX) with a radius be-

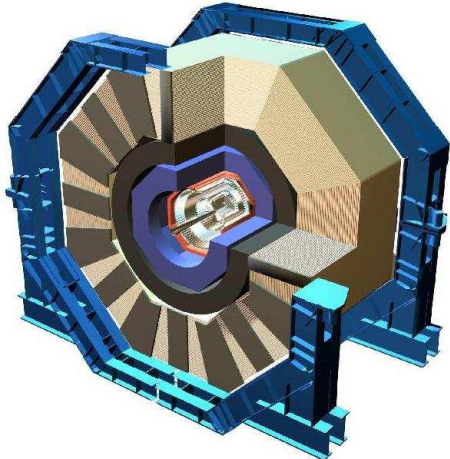
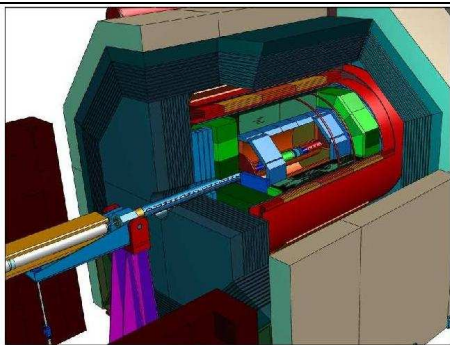
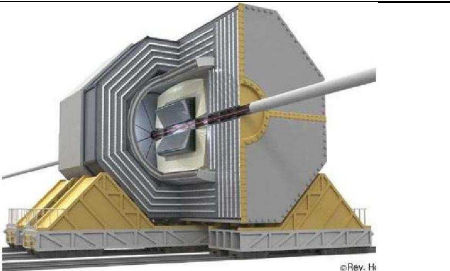
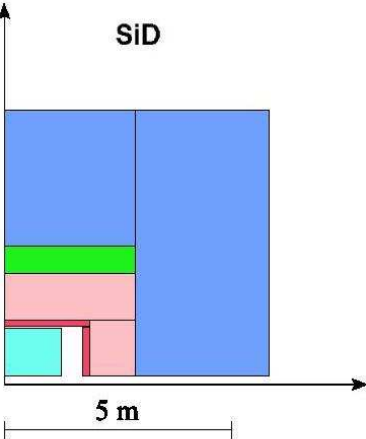
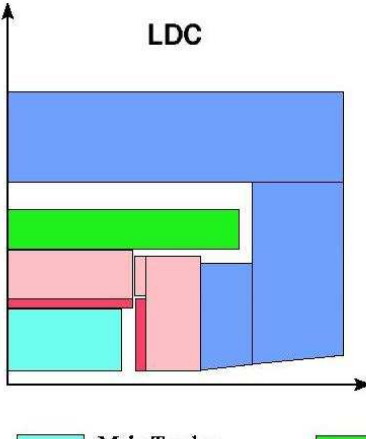
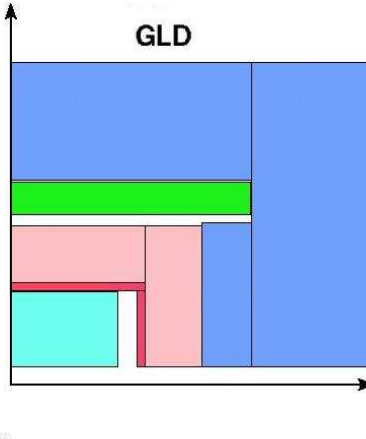
<p>Silicon Detector Design (SiD)</p> <p>Uses a fast timing silicon tracker and a very good resolution SiW ECAL. It has a small radius but this fact is compensated by a high magnetic field of 5 Tesla.</p>							
<p>Large detector concept (LDC)</p> <p>Employs a TPC gaseous tracker and a SiW ECAL of “medium radius” with a magnetic field of 4 Tesla.</p>							
<p>Global Large Detector (GLD)</p> <p>Has a large radius and a magnetic field of 3 Tesla. Employs a gaseous tracker and a scintillator-tungsten ECAL.</p>							
<div style="display: flex; justify-content: space-around; align-items: flex-start;"> <div style="text-align: center;"> <p>SID</p>  </div> <div style="text-align: center;"> <p>LDC</p>  </div> <div style="text-align: center;"> <p>GLD</p>  </div> </div> <div style="margin-top: 10px; text-align: center;"> <table border="0"> <tr> <td style="padding-right: 20px;"> Main Tracker</td> <td> Cryostat</td> </tr> <tr> <td style="padding-right: 20px;"> EM Calorimeter</td> <td> Iron Yoke / Muon System</td> </tr> <tr> <td style="padding-right: 20px;"> H Calorimeter</td> <td></td> </tr> </table> </div>		Main Tracker	Cryostat	EM Calorimeter	Iron Yoke / Muon System	H Calorimeter	
Main Tracker	Cryostat						
EM Calorimeter	Iron Yoke / Muon System						
H Calorimeter							

Table 3.2: The three detector concepts for the international linear collider ILC.

Property	
Track momentum resolution	<p>Physics Requirement. Measurements of recoil mass requires excellent momentum resolution.</p> <p>Solution. Large tracking volume and high magnetic field.</p>
Vertexing	<p>Physics Requirement. Tagging of b and c jets.</p> <p>Solution. A multi-layered Si-based pixel detector with a minimum of material, an innermost layer as close as possible to the interaction point (IP) and a large solenoidal field to confine the background generated in the interaction of the colliding bunches.</p>
Energy Flow	<p>Physics Requirement. The analysis of multi-parton final states employing the particle flow technique which requires an efficient association of the particles in the tracker to those on the calorimeters. This association results more effective if the material between the tracker and the calorimeter is minimized as much as possible.</p> <p>Solution. Tracker and calorimeters contained inside the magnet. Large magnet size to be able to maximize the thickness of the calorimeters and the shower separability. Very granular and efficient electromagnetic and hadronic calorimeters.</p>
Hermeticity	<p>Physics Requirement. Missing energy is the signature of several processes of interest, therefore hermeticity and particle detection capability at small angles is required.</p> <p>Solution. Hermeticity requires having good coverage of and measurement capability in the forward direction; this is also essential to allow a precision determination of the luminosity spectrum.</p>

Table 3.3: Properties for the detector according to the physics requirements.

tween 1.5 and 6 cm, a set of tracking detectors located between the VTX and the TPC (cylinders in the barrel (SIT) and discs in the forward region (FTD)) and finally a precise forward chamber located behind the TPC endplate (FCH). The layout of the tracking system components is shown in Fig. 3.6.

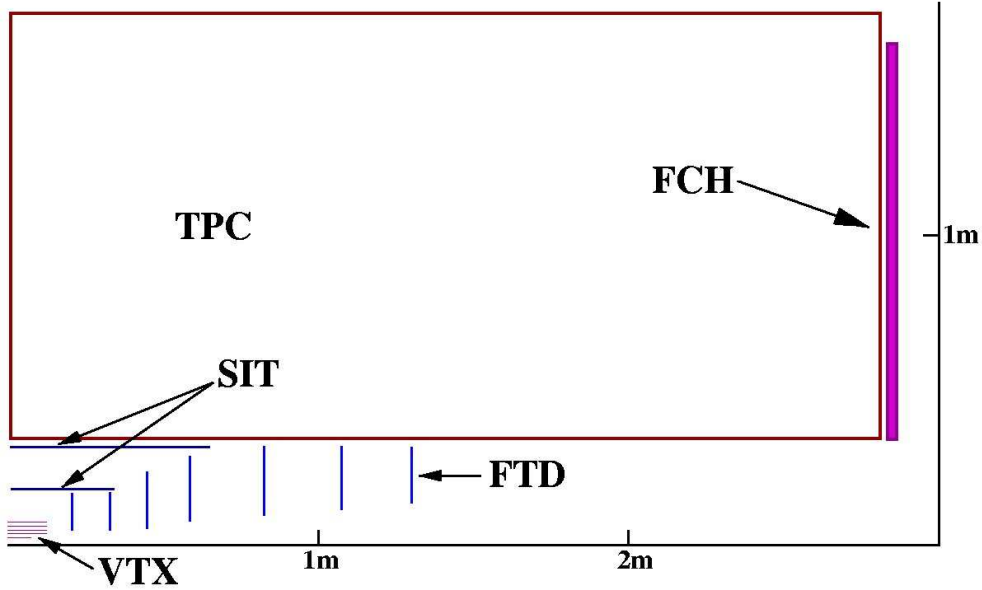


Figure 3.6: Layout of the components of the tracking system.

The required b- and c-tagging capabilities of the VTX should be achieved by a point-measurement precision of about $1\mu\text{m}$ which is reflected in an impact parameter resolution $\sigma_{IP} < 5\mu\text{m} + 10\mu\text{m}/p_t$. The current design contemplates a structure of 5 cylindrical layers of vertex pixel detector between $r = 1.5\text{ cm}$ and $r = 6\text{ cm}$. Two technology options for the VTX are CCD and CMOS Pixels.

The silicon intermediate tracker (SIT) and the forward tracking disks (FTD) are detectors whose main role is to improve the momentum resolution by adding a few very precise space points between the VTX and the TPC. In this way the VTX tracks can be linked to the TPC tracks with a better precision. The SIT consists of two cylinders of double sided silicon strip detectors with a radii of 16 and 30 cm. The FTD is composed of seven disks perpendicular to the z -direction. The first three disks are pixel detectors and the last four are conformed by strip detectors.

The main component of the central tracking system is the TPC, aiming to a momentum resolution $\delta(1/p_t) < 2 \times 10^{-4}(\text{GeV})^{-1}$ and a dE/dx resolution smaller than 5%. However, combining all the tracking system sub-detectors the goal of a momentum resolution $\delta(1/p_t) < 5 \times 10^{-5}(\text{GeV})^{-1}$ can be achieved. Because of the short time between bunch crossings with respect to the drift velocity the timing information has to be sufficiently precise to disentangle events originated from different bunches. In some cases, dense jet environments or events with large backgrounds difficult the task of pattern recognition. This problem is overcome by the good momentum resolution and the many space point measurements product of the large radius of the central tracker. The TPC must be filled with a gas which ensures an adequate drift velocity capable to empty the drift region as quickly as possible. The value of drift velocities for several experiments is shown in Fig. 3.7 [23, 24]. The mixture: Ar-CO₂-CH₄ (93-2-57%), which has a drift velocity of 4.6 cm/ μ s with a drift field of 230 V/cm is considered as a good candidate [22]. The amplification of the drifting electrons can be performed by two recently developed gas avalanche micro detectors: Gas Electron Multipliers (GEMs) [29] or Micromegas [30]. Below $\theta = 12^\circ$, where no vertex detector layer is crossed anymore, the momentum resolution deteriorates due to the decreasing lever-arm, even with the silicon discs present. This problem is addressed by the addition of the forward chamber (FCH). The FCH is located between the TPC and the endcap. Figure 3.8 shows the layout of The FCH system consists of 6 planes of straw-chambers. Each plane is built up from two layers of straws which are shifted with respect to each other by one half of the distance between neighboring wires. At larger polar angles, above $\theta = 12^\circ$, the FCH assists the TPC in the pattern recognition, can be used to help the calibration of the TPC, and serves as a pre-shower detector for showers initiated in the TPC endplate.

Calorimetric Detectors

The particle flow technique requires each final state particle to be reconstructed, this makes necessary the use of imaging calorimetry (a three dimensional picture of the shower development at the calorimeters). The spatial separation of the particles on the inner surface of the electromagnetic calorimeter is influenced by both, the distance R of the calorimeter to the IP and the strength of the magnetic field B . Thus the figure of merit is given in first approach as $B \cdot R^2$. In the case of the LDC “moderate” values for the magnetic field strength and radius have been chosen. In comparison, the magnetic field for the SiD is larger, allowing to reduce the detector size, while in the case of the GLD the situation reverses. A dense calorimeter of high granularity is another factor

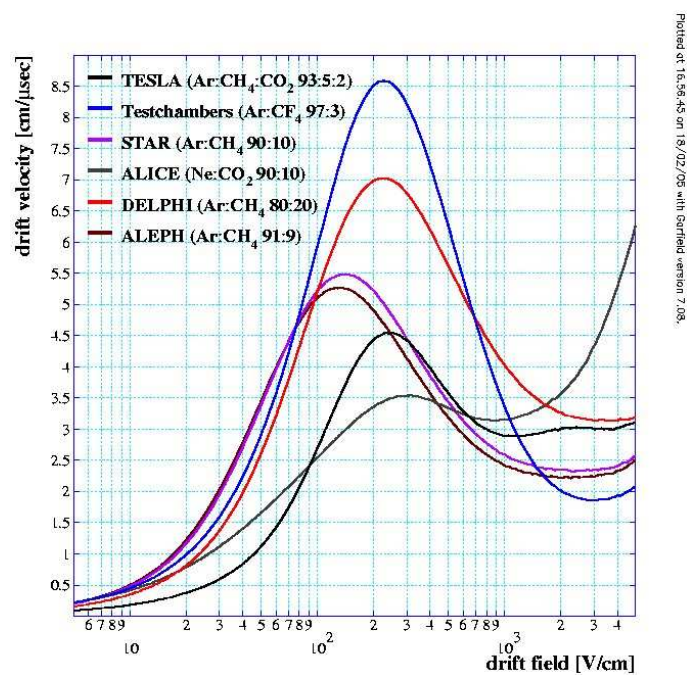


Figure 3.7: Drift velocities for gas mixtures employed in TPCs [23]. The asterisks show the operation points.

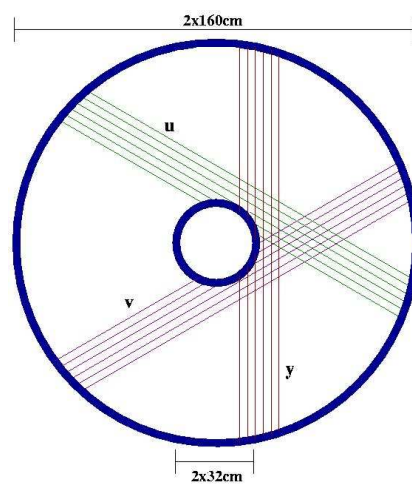


Figure 3.8: Layout of the FCH wires. The u , v coordinates are rotated with respect to y by $\pm 60^\circ$.

necessary to achieve a good separation power. A silicon-tungsten (Si-W) calorimeter based on tungsten absorbers and silicon diode pads is proposed as the main option for the ECAL of the LDC detector. The LDC ECAL operating 32 million channels is expected to reach a resolution of $\Delta E/E < 0.1/\sqrt{E(\text{GeV})} + 0.01$. Other hybrid options are also under study.

In addition to a high granularity the HCAL must have a good time resolution, capable to measure the time of the events with enough precision to reject the cosmic events and for distinguishing exotic signatures of long lived particles predicted by some SUSY models. In the HCAL case the goal is to achieve an energy resolution $\Delta E/E < 0.5/\sqrt{E(\text{GeV})} + 0.04$. At the moment there are three technology options for the HCAL:

- a) A moderate segmentation Fe-scintillator with analogue readout of the cells.
- b) A highly segmented Fe-resistive plate chamber (RPC) digital calorimeter.
- c) A highly segmented Fe-GEM digital calorimeter.

Muon Detector and Coil

The ILC magnet design is based on the CMS experiment [31] with the additional requirement of an even more homogeneous magnetic field, specially in the TPC region. The goal for the degree of homogeneity is given by:

$$\left| \int_0^{2.5m} (B_r/B_z) dz \right| \leq 2mm, \quad (3.3)$$

where

$$B_r = B_x(x/r) + B_y(y/r). \quad (3.4)$$

The coil is composed by three central modules 1.60 m long each and two external modules are 0.80 m long each. The barrel yoke, of octagonal shape, has an inner radius of 3.85 m, an outer radius of 6.00 m and a total length of 6.60 m. Radially the yoke is subdivided into 10 layers of 10 cm iron plate and 4 cm space for muon chambers. At the outer radius the yoke is completed by a 1.0 m thick layer of solid iron. The end cap yokes have also an octagonal shape. The muon detector has two purposes, the identification of muons and tail catching of hadronic showers, hence an adequate longitudinal segmentation is desirable. The iron of the magnet's yoke is used as an absorber and resistive plate chambers are used as detectors, employing strips 3 cm wide, to obtain

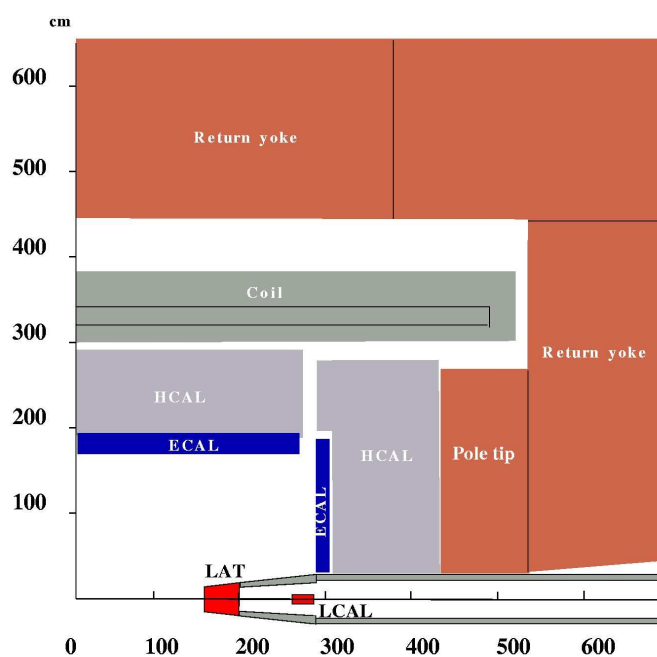


Figure 3.9: The ECAL and the HCAL are immersed in the 4 Tesla magnetic field.

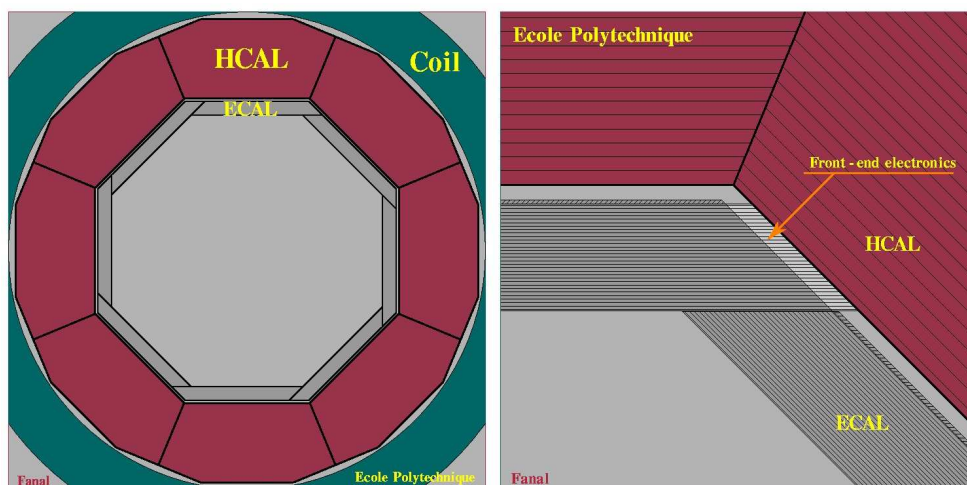


Figure 3.10: An $x - y$ plane view of the electromagnetic and hadronic calorimeters and the location of the front-end electronics.

a resolution of 1 cm. The muon detector is expected to have an efficiency $\varepsilon > 99\%$ for $p > 6$ GeV.

Forward Region Detectors

The signature of many physics processes predict reactions with large missing energy signals, hence a good detector system in the very forward region of the LDC is necessary to fulfill the hermeticity requirements of the ILC. The luminosity calorimeter (LumiCal) and the beam calorimeter (BeamCal) are the main components of The very forward region (VFR) instrumentation consists of three components described below. There are two variants of the VFR instrumentation, one for zero or 2 mrad crossing angle (Fig. 3.11) and one for 20 mrad crossing angle (Fig. 3.12).

Beam Calorimeter (BeamCal) The BeamCal will be used to make fast luminosity measurements. For this purpose it will transmit information directly to the beam delivering system. The BeamCal can be also employed for electron veto. The BeamCal covers a polar angle between 5 and 28 mrad.

Luminosity Calorimeter (LumiCal) The LumiCal's function consists in providing accurate measurements of the luminosity (with a precision better than 10^{-3}). The process of Bhabha scattering at low angle will be employed for the measurement [25]. The LumiCal covers a polar angle between 26 and 82 mrad.

Low angle Hadron Calorimeter (LHCAL) A hadron calorimeter covering almost the polar angle range of LumiCal.

3.3 Beam Polarization and Polarimetry at the ILC

It was already mentioned that the polarized electrons are produced by shooting circularly polarized laser light with a wavelength 840 nm into a GaAs cathode. More details about polarization transfer from electrons (positrons) to photons and vice versa are given in Chapter 6. The polarized electron source will be based on technology developed for SLC [26] and for the NLC [27]. After the generation, the electrons are sent to the polarized electron pre-accelerator linac after being split into smaller bunches. The unpolarized positron source employs the process of high-energy photon conversion into e^+e^- pairs in a thin rotating conversion target. The photons are created by the

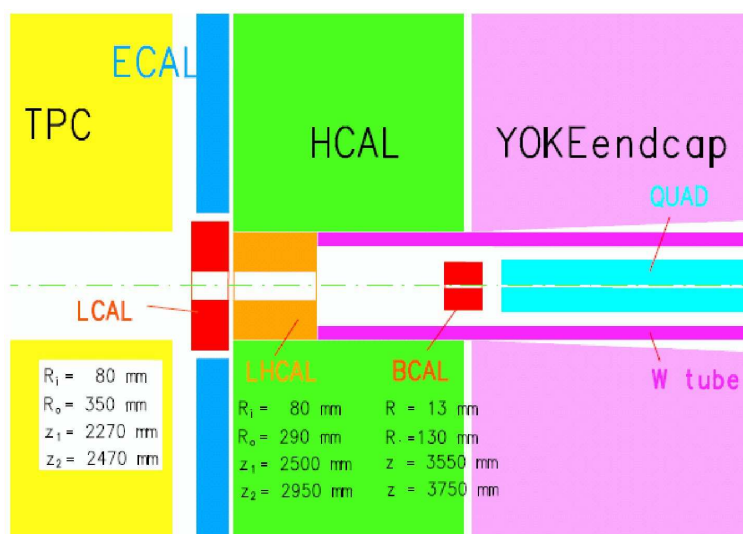


Figure 3.11: The very forward region for zero or 20 mrad. The BeamCal, the LumiCal and the LHCAL are centered on the Detector axis.

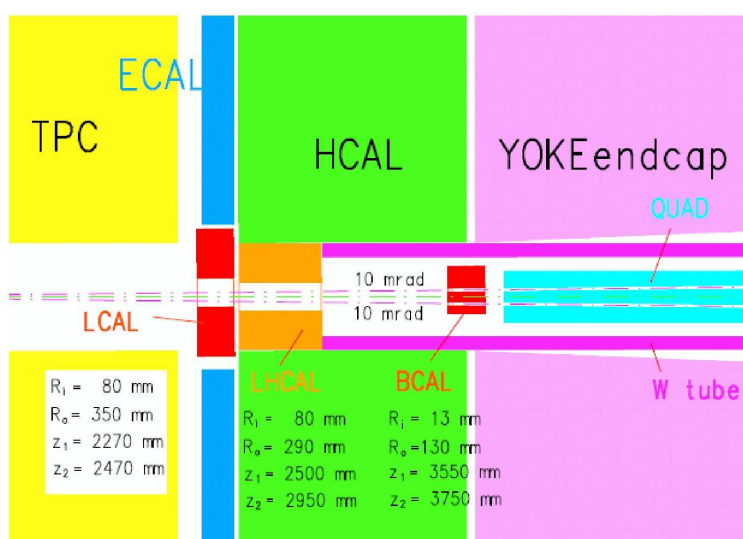


Figure 3.12: The very forward region for 20 mrad. The BeamCal, the LumiCal and the LHCAL are centered on the axes of the outgoing beams.

passage of the high energy electron beam (150-250 GeV) through a planar undulator magnet. For the polarized positron source an helical undulator magnet is used instead to generate circularly polarized photons which transfer the polarization to the positrons produced at the conversion target. The production of polarized positrons is the subject of Chapter 6. The positrons are produced with a large emittance, thus they have to be focused using solenoids before sending them to the first pre-acceleration stage.

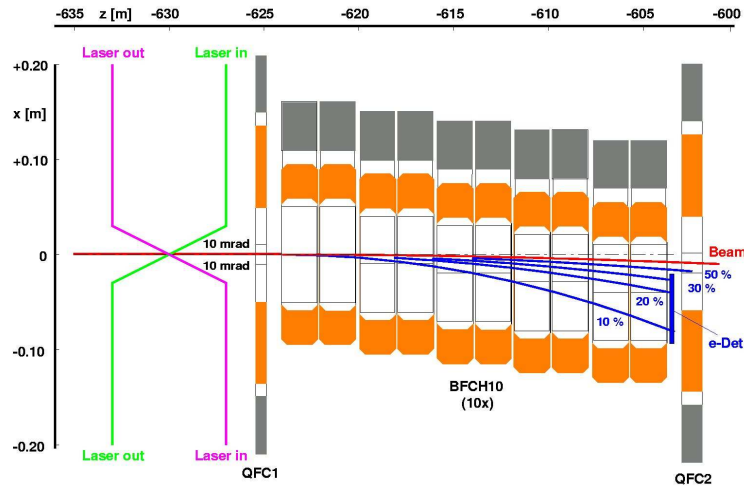


Figure 3.13: Layout of the Compton polarimeter from the TESLA TDR.

Compton polarimetry is considered as the main option to measure the beam polarization at the ILC, among other reasons because the Compton scattering rate is high and small statistical errors can be achieved in a short amount of time (less than 1% precision in one minute), and the laser helicity can be selected on a pulse-by-pulse basis. With this technique it is possible to achieve an accuracy of $(\Delta P_{e^-}/P_{e^-}) = 0.25\%$ [28] Fig. 3.13 shows a diagram of the Compton polarimeter from the TESLA TDR, the circularly polarized laser beam crosses the electron or positron beam with a small crossing angle of 10 mrad. The longitudinal polarization of the electron or positron beam is determined from the asymmetry of two measurements of Compton scattering with parallel and antiparallel spin configurations of the interacting electron and laser beams. To achieve a good precision in the measurement the Compton laser has to be pulsed with a pattern that matches the pulse and bunch structure of the ILC. To cover the whole range of beam energies the wavelength of the laser has to be changed. Alternatively the use of a chicane can permit the polarization measurement for all

the beam energies using a single wavelength. Beam-beam depolarization effects can be measured directly by comparing beams in and out of collision. For this purpose two polarimeters can be employed, one located upstream of the IP and the other downstream.

An alternative for measuring the beam polarization is to employ data from SM events and the fact that the polarization dependency of the physics processes is well known. This method could be useful for some SM and beyond-SM measurements where the precision provided by Compton polarimetry (0.25%) is not enough to reach the required sensitivity. A particular analysis of the expected accuracy of polarization measurements using data is the topic of Chapter 5 (more general views are exposed on [41] and [45]).

Chapter 4

TGCs and Transverse Beam Polarization

Simulations of physics events considering a given machine and detector set-up play an important role to determine the discovery potential and degree of precision of the collider and detectors. This interplay between simulations, collider and detector design, as well as data processing algorithms will result in the final ILC concept. One of the tasks of the ILC is to accomplish precision measurements in order to test the $SU(2)_L \otimes U(1)_Y$ structure of the electroweak sector of the SM. Extensions of the SM like Supersymmetry (SUSY) models would also manifest themselves as loop corrections which could be measurable at an e^+e^- Linear Collider with a center-of-mass energy of 500 GeV [32]. On the other hand, the couplings between gauge bosons are sensitive to models of strong electroweak symmetry breaking. In addition, high precision measurements will be useful to increase the confidence for the extrapolation of the couplings to high scales in order to test theories of grand unification. The production of W -pairs in electron-positron annihilation offers the possibility to test the WWZ and $WW\gamma$ Triple Gauge Boson Couplings (TGCs).

As it was highlighted in Chapter 2, beam polarization gives the advantage of increasing the sensitivity to deviations from the SM and also permits to disentangle different contributions. In this study the option of transverse beam polarization is considered. Once longitudinal beam polarization is realized, it is possible to use spin rotators to achieve transverse polarization [33]. The sensitivity to anomalous TGCs obtained with transverse beam polarization is compared with the case of longitudinal beam polarization. This topic has been already addressed in a comprehensive way by

Nagel et. al. [34]. The difference between the two studies will be explained in Section 4.7. In this study, the potential to explore the physics of longitudinal W bosons is outlined.

4.1 Triple Gauge Boson Couplings

Figures 2.2(a) and 2.2(b) show the Feynman diagrams for on-shell W -pair production. Fig.2.2(a) corresponds to the ν -exchange t-channel diagram, and Fig.2.2(b) shows the s-channel diagram containing the three gauge boson vertex, which is sensitive to anomalous TGC. To model the possible SM deviations which could manifest in processes involving three gauge boson interactions like W -pair production, one has to assume the most general effective Lagrangian describing TGCs WWV ($V = Z$ or γ) [35].

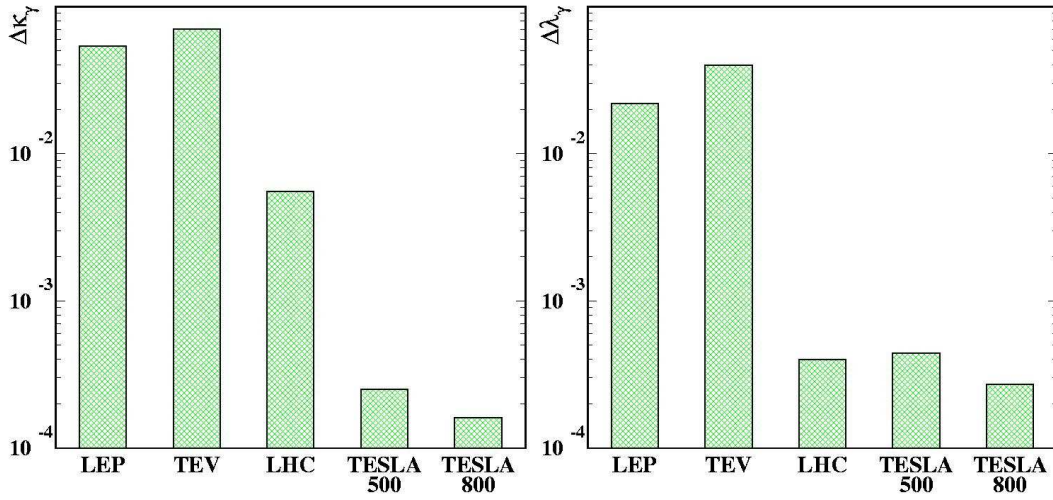
$$\begin{aligned} \frac{\mathcal{L}_{WWV}}{ig_{WWV}} &= g_1^V V^\mu (W_{\mu\nu}^- W^{+\nu} - W_{\mu\nu}^+ W^{-\nu}) + \kappa_V W_\mu^- W_\nu^+ V^{\mu\nu} \\ &+ \frac{\lambda_V}{M_W^2} V^{\mu\nu} W_\mu^{+\rho} W_{\rho\nu}^- - ig_4^V W_\mu^- W_\nu^+ (\partial^\mu V^\nu + \partial^\nu V^\mu) \\ &+ ig_5^V \varepsilon^{\mu\nu\rho\sigma} [(\partial^\rho W_\mu^-) W_\nu^+ - W_\mu^- (\partial^\rho W_\nu^+)] V_\sigma \\ &+ \frac{\tilde{\kappa}_V}{2} W_\mu^- W_\mu^+ \varepsilon^{\mu\nu\rho\sigma} V_{\rho\sigma} + \frac{\tilde{\lambda}_V}{2M_W^2} W_{\rho\mu}^- W_\nu^{+\mu} V_{\alpha\beta}, \end{aligned}$$

here $U_{\mu\nu} = \partial_\mu U_\nu - \partial_\nu U_\mu$, with $U = W^\pm, Z, \gamma$. In the SM at tree level the values of the parameters are fixed. One has $g_1^V = k_V = 1$, and the other couplings are equal to zero. For simplification consider the deviations from the SM: $\Delta g_1^\gamma = g_1^\gamma - 1$, $\Delta g_1^Z = g_1^Z - 1$, $\Delta \kappa_\gamma = \kappa_\gamma - 1$ and $\Delta \kappa_Z = \kappa_Z - 1$. The couplings g_1^V, k_V, λ_V and g_5^V are CP conserving, while $g_4^V, \tilde{\kappa}_V, \tilde{\lambda}_V$ violate CP. In most of the studies this couplings are assumed to be real (In [34] also complex values are considered). With this values the Lagrangian 4.1 describing TGCs reduces to the SM Lagrangian for TGCs (expression 2.13). Until now no anomalous values for the TGCs have been observed, however the current bounds provided by different experiments and mainly by LEP are still relatively weak (see Table 4.1). The comparisons of the sensitivity to anomalous values of $\Delta \kappa_\gamma$ and $\Delta \lambda_\gamma$ for different machines is made in Fig. 4.1, showing the superiority of the ILC regarding precision measurements of the TGCs.

Parameter	Δg_1^Z	$\Delta \kappa_\gamma$	$\Delta \tilde{\kappa}_Z$	λ_γ	λ_Z
1- σ bounds	+0.022 -0.019	+0.044 -0.045	+0.059 -0.056	+0.020 -0.021	+0.060 -0.057

Parameter	g_4^Z	Δg_5^Z	$\tilde{\kappa}_Z$	$\tilde{\lambda}_Z$
1- σ bounds	+0.32 -0.33	+0.7 -0.9	+0.10 -0.07	+0.24 -0.16

Table 4.1: Bounds on TGCs measurements (68% C.L.) [9].

Figure 4.1: The sensitivity of different machines to the parameters $\Delta \kappa_\gamma$ and $\Delta \lambda_\gamma$. For LHC a luminosity of 300 fb^{-1} is assumed, and for TESLA/ILC 900 fb^{-1} and 1500 fb^{-1} for $\sqrt{s} = 500 \text{ GeV}$ and $\sqrt{s} = 800 \text{ GeV}$ respectively.

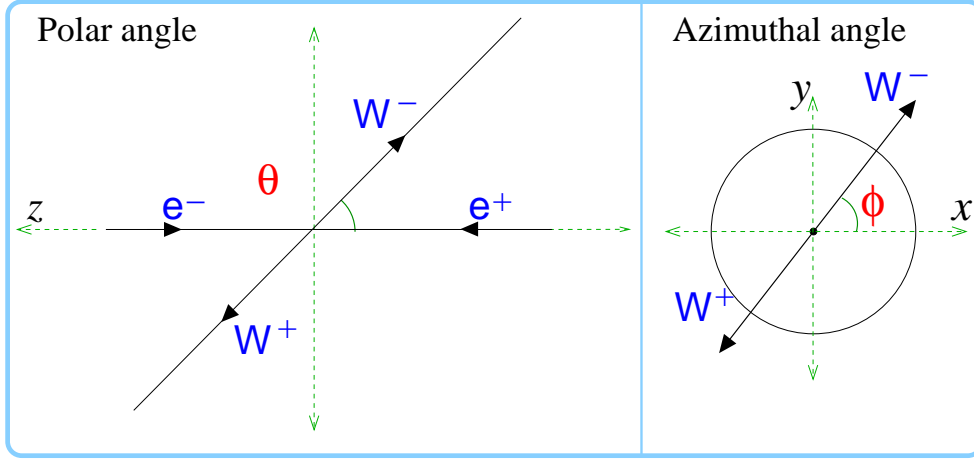


Figure 4.2: W -pair production angles: The polar angle θ (the angle between e^- and W^-), and the azimuthal angle ϕ (in the x - y -plane).

4.2 Transverse Polarization

In the case of unpolarized or longitudinally polarized beams the differential cross section depends on the W -pair production polar angle θ between the electron and the W^- (Fig. 4.2), but it is independent of the azimuthal angle ϕ , in the x - y -plane. A dependency on the azimuthal angle is present only in the case of transverse beam polarization. The explicit dependency on the angles will be discussed in the following.

Consider the electron density matrix $\rho_{\sigma\sigma'}$ in the helicity basis

$$\rho_{\sigma\sigma'} = \frac{1 + \vec{\sigma} \cdot \vec{P}}{2} = \frac{1}{2} \begin{bmatrix} 1 + P_L & P_T e^{-i\phi} \\ P_T e^{-i\phi} & 1 - P_L \end{bmatrix}, \quad (4.1)$$

where $\vec{P} = (P_T \cos \phi, P_T \sin \phi, P_L)$, P_L and P_T denote the magnitude of the longitudinal polarization and the transverse polarization, and $\vec{\sigma}$ are the Pauli matrices. Consider also the helicity amplitudes $M_{\sigma\bar{\sigma}}$ for the process $e^+e^- \rightarrow W^+W^-$ ($\sigma, \bar{\sigma}$ are the helicities of the electron and the positron respectively). Then, the square of the matrix element for W -pair production is given by

$$|\overline{M}|^2 = \sum \rho_{\sigma\sigma'} \bar{\rho}_{\bar{\sigma}\bar{\sigma}'} M_{\sigma\bar{\sigma}} M_{\sigma'\bar{\sigma}'}^* \quad (4.2)$$

Only the amplitudes M_{-+} and M_{+-} are different from zero in the limit of vanishing electron mass. Using the explicit form of the density matrix (4.1) gives[37]:

$$\begin{aligned} \frac{d\sigma}{d\Omega} \propto \overline{|M|^2} &= \frac{1}{4}(1 - P_L P'_L)(|M_+|^2 + |M_-|^2) + \frac{1}{4}(P_L - P'_L)(|M_+|^2 - |M_-|^2) \\ &\quad - \frac{1}{2}(P_T P'_T)[\cos(2\phi) \operatorname{Re}(M_+ M_-^*) + \sin(2\phi) \operatorname{Im}(M_+ M_-^*)], \end{aligned} \quad (4.3)$$

where $M_- = M_{-+}$ and $M_+ = M_{+-}$. In this expression one can appreciate the ϕ -dependence of $d\sigma/d\Omega$ in the presence of transverse polarization. Three situations can be distinguished:

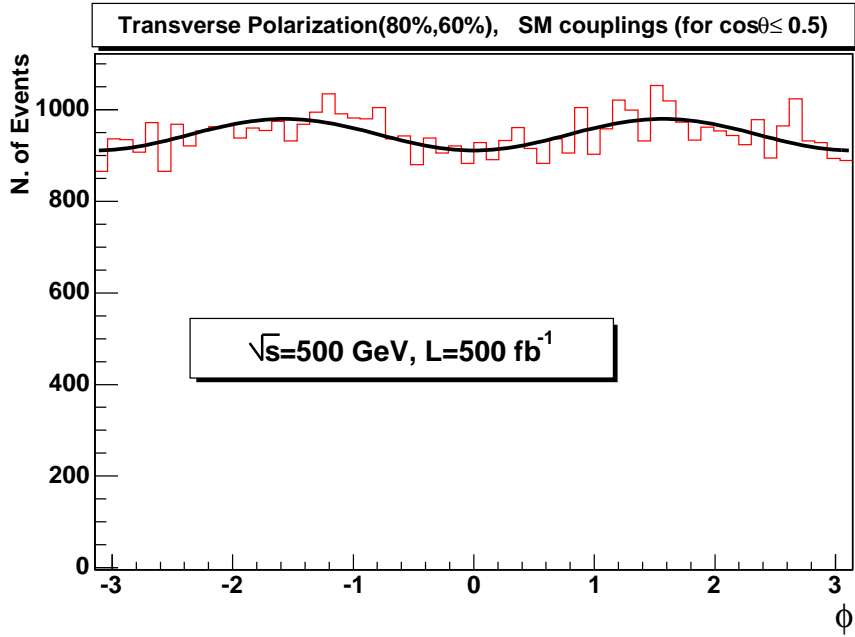
- a) **No polarization** ($P_L = P_T = 0$): When no beam polarization is present the contribution coming from $|M_+|^2 + |M_-|^2$ is measured.
- b) **Longitudinal polarization**: In the presence of longitudinal polarization one is again sensitive to $|M_+|^2 - |M_-|^2$ in addition to $|M_+|^2 + |M_-|^2$.
- c) **Transverse Polarization**: In the case of transverse polarization ($P_T P'_T \neq 0$) contributions from $\operatorname{Re}(M_+ M_-^*)$ and $\operatorname{Im}(M_+ M_-^*)$ are measured. The ϕ -distribution deviates from the flat shape present when the beams are not polarized or longitudinally polarized (Fig. 4.3). In the SM only CP-conserving couplings occur. In this case $\operatorname{Im}(M_+ M_-^*) = 0$ and only the term containing $\cos 2\phi$ contributes.

Figure 4.4 shows $\cos\theta$ -distributions of the W^- bosons for transverse and longitudinal beam polarization for SM couplings and for $\tilde{k}_Z = 1$. Here one can observe the change of the cross section for anomalous TGCs.

The size of the contribution from $\operatorname{Re}(M_+ M_-^*)$ in Eq. 4.3 can be estimated by the azimuthal asymmetry $d(\sigma A_T)/d\cos\theta$:

$$\begin{aligned} \frac{d(\sigma A_T)}{d\cos\theta} &= \int_{-\pi}^{\pi} \frac{d\sigma}{d\Omega} \cos 2\phi d\phi \\ &= \frac{\beta_W}{64\pi s} 2 \operatorname{Re}(M_+ M_-^*), \end{aligned}$$

where $\beta_W = \sqrt{1 - 4M_W^2/s}$ and $s = 4E_b^2$, with E_b being the beam energy. The azimuthal asymmetry has an interesting feature: while the contribution of the $W_L^+ W_L^-$



a) SM couplings

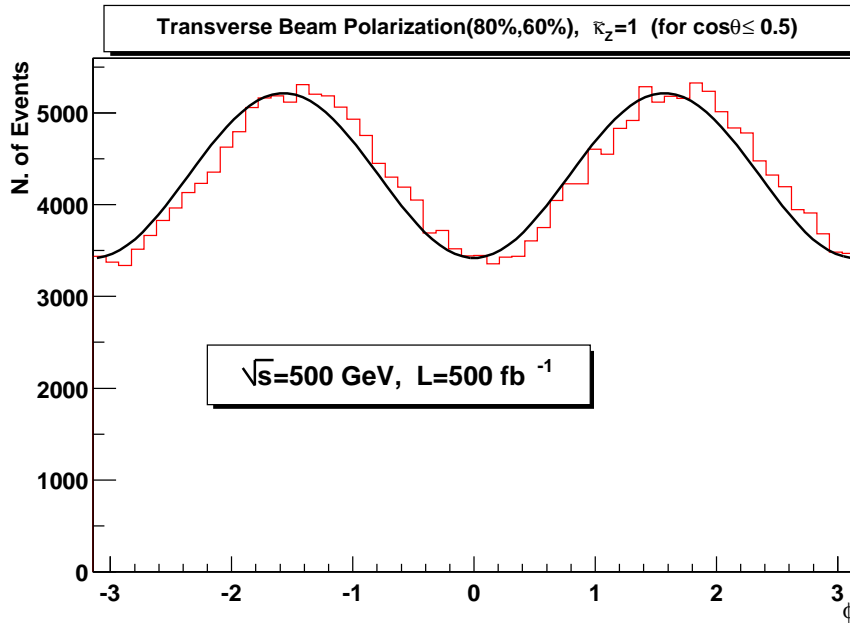
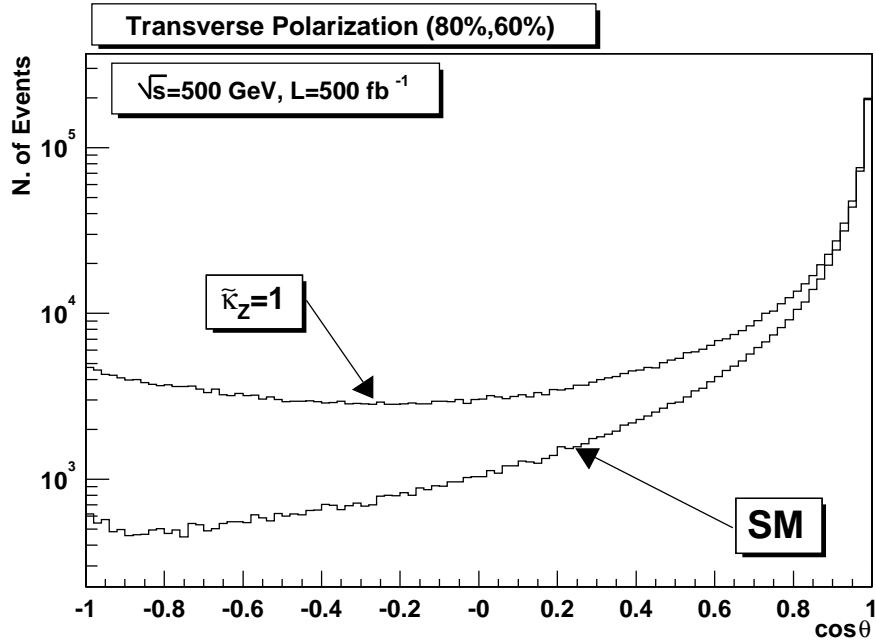
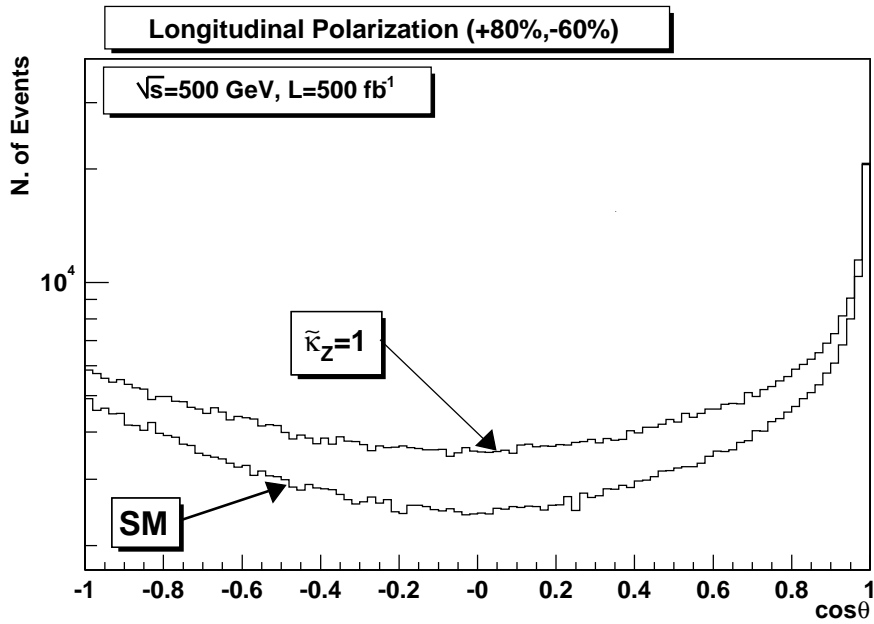
b) $\tilde{k}_Z = 1$

Figure 4.3: Distributions for W^- showing the dependence on the ϕ angle. Fig. 4.3 a) shows the SM distribution. In Fig. 4.3 b) the distribution corresponding to $\tilde{k}_Z = 1$ is shown. A fitted function shows the phase shift resulting from anomalous CP violating couplings (the phase shift of the fitted function is fixed to the SM phase).



a) Transverse beam polarization.



b) Longitudinal beam polarization.

Figure 4.4: $\cos\theta$ -distributions for W^- for transverse and longitudinal beam polarization (comparison between SM couplings and $\tilde{k}_Z = 1$). Here one can observe the change of the cross section for anomalous TGCs.

final state to the total cross section is very small, it dominates completely in the azimuthal asymmetry. The contributions from the state in which W^+ has transverse polarization and W^- is longitudinal ($W_T^- W_L^+$) and the contribution coming from the ($W_L^- W_T^+$) state mutually cancel (Fig. 4.5). In this sense, the azimuthal asymmetry could be used to study the physics of longitudinal W bosons without analyzing the final state polarization [37].

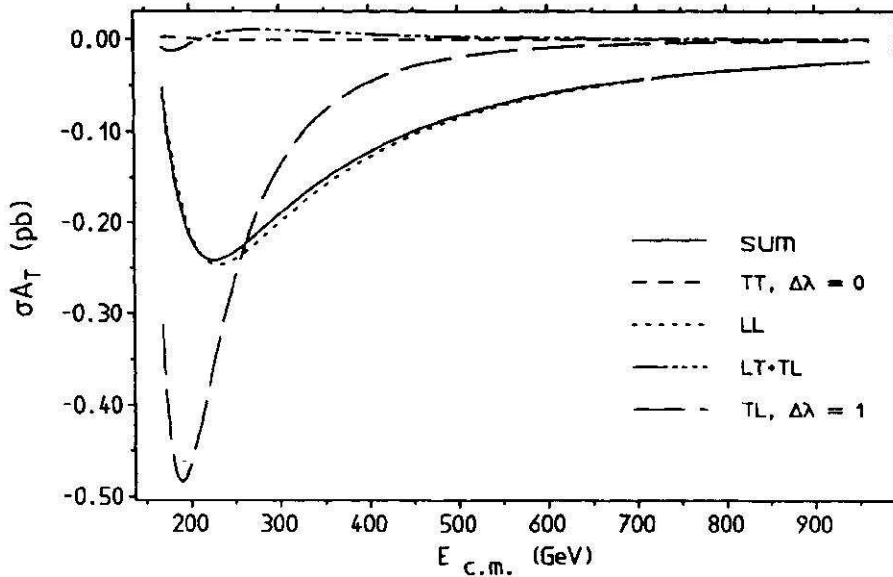


Figure 4.5: Contribution from the final state polarization modes ($W_T^+ W_T^-$, $W_L^+ W_L^-$, $W_T^+ W_L^-$ and $W_L^+ W_T^-$) to the azimuthal asymmetry $d(\sigma_{A_T})/d \cos \theta$. Here $\Delta\lambda = \lambda - \bar{\lambda}$, where λ ($\bar{\lambda}$) is the helicity of the W^- (W^+) [37].

4.3 Monte Carlo Event Generators

In this section the Monte Carlo event generator used in this study is introduced together with the generators employed in the study exposed in Chapter 5. WHIZARD [38] calculates multi-particle scattering cross sections and generates event samples for processes with up to six final state particles. Tree-level matrix elements are generated using O'Mega [53], CompHep [51] and MadGraph [52]. The event samples for this study are generated with WHIZARD, also the signal events and some background

processes for the analysis presented in Chapter 5 are produced with this program. Table 4.2 presents the main features of the event generators WHIZARD, KoralW [49] and grc4f [50]. The last two programs are also employed in the polarization measurement study of Chapter 5. The program SIMDET [58] is employed to simulate the linear collider detector response. SIMDET uses a parametrization of results from the Monte Carlo program BRAHMS [59]. It considers detailed and realistic information for charged particle momenta and directions, impact parameters and calorimeter energies and directions. Gaussian smearing procedures are employed to generate the detector response at SIMDET.

WHIZARD.	Generates events using beam polarization. Uses O’Mega, CompHep and MadGraph as matrix element generators. Includes Initial State Radiation(ISR) (Collinear approximation). Simulates Beamstrahlung using Circe [54].
KoralW.	Has not beam polarization, Uses GRACE [55] as as matrix element generator. Includes ISR with the proper angular distribution. Multiphoton bremsstrahlung is implemented in the ISR approximation using the Yennie-Frautschi-Suura (YFS) formulation with the leading-log matrix elements [49]. The final state QED radiation is generated for charged leptons with PHOTOS (up to two photons)[56].
grc4f.	Generates events using beam polarization. Uses GRACE as as matrix element generator. Includes ISR (Two types: a) Collinear approximation, an b) photons with the proper angular distribution.)

Table 4.2: Main features of the three fully massive 4-fermion generators used in this study.

4.4 Analysis

4.4.1 Frame of the Study

The following conditions are assumed for this study: a center-of-mass energy of 500 GeV, a luminosity L of 500 fb^{-1} and transverse beam polarization (80% right handed electrons and 60% left handed positrons). The Monte Carlo (MC) samples are generated with WHIZARD, including initial state radiation (ISR) and beamstrahlung. The diagrams which contribute to the W -pair production are the t-channel ν exchange and the s-channel γ and Z exchange (Fig. 4.2). The WHIZARD input file for the case of transverse polarization is given in Appendix B. Only the semileptonic decay channel, $e^+e^- \rightarrow W^+W^- \rightarrow \mu\bar{\nu}_\mu q_1\bar{q}_2$, where the charged lepton is a muon is considered. The three decay channels for W -pair production, the leptonic, the semileptonic and the hadronic, have branching ratios of 0.106, 0.439 and 0.456, respectively[36]. For the decay channel considered in this study the branching ratio corresponds to 1/3 of the total semileptonic branching ratio, and therefore, the sensitivity obtained in this study is roughly $\sqrt{3}$ smaller than the sensitivity for the total semileptonic channel.

4.4.2 Fit Method and Construction of Reference Distributions

The sensitivity to deviations from the SM value for a generic coupling constant $\alpha \in \{g_1^V, \kappa_V, \lambda_V, g_4^V, g_5^V, \tilde{\kappa}_V, \tilde{\lambda}_V\}$ ($V = \gamma$ or Z), is quantified by means of the 1σ -bound, defined as the value of α for which the SM and the anomalous coupling distributions are distinguishable at the 1σ level. The smaller the 1σ -bound is, the higher the sensitivity to effects beyond the SM is. To obtain the 1σ -bound, angular distributions ($\cos\theta, \phi$ and two-dimensional ($\cos\theta, \phi$)) for different values of the parameter α are compared with the ones assumed in the SM using the χ^2 method.¹ The 1σ -bound for anomalous values of α , is determined by the condition $\Delta\chi^2(\alpha_{1\sigma}) = 1$, where $\Delta\chi^2 = \chi^2 - \chi_{min}^2$; here χ_{min}^2 corresponds to the SM case. Fig.4.6 shows an example of a $\Delta\chi^2$ curve employed to determine the sensitivity to anomalous TGCs (Δg_1^γ in this case), this curve

¹Given two distribution histograms with i -th bin contents m_i and n_i , one defines:

$$\chi^2 = \sum_i \left(\frac{m_i - n_i}{\sqrt{m_i}} \right)^2$$

is constructed using the polar angle θ observable. The construction of a reference distribution for a given value of α is described below.

It is impossible to generate MC events for each required value of the parameter α , but one can construct a reference distribution for a given value of α assuming a quadratic behavior of the cross section on the coupling constants for each bin of the distribution. This is motivated by the linear occurrence of the coupling constants in (4.1). For the construction of the reference distributions 3 sets of MC events for different values of α : $\alpha_0, \alpha_1, \alpha_2$ are used. The events are generated with WHIZARD using the conditions described in 4.4.1. Let $n_i(\alpha)$ denote the bin content of the i -th bin from an angular distribution histogram for a given value of the parameter α , and let α_1 be the SM value of α . A parabola $n_i(\alpha)$ which contains the points $n_i(\alpha_0), n_i(\alpha_1)$ and $n_i(\alpha_2)$ is constructed for each bin of the angular distribution histograms. In this way, one can obtain a reference distribution with bin contents $n_i(\alpha)$ just by inserting the desired value of α . The procedure employed to compute the 1σ -bound and to verify the method is described in appendix A. The values of α_0 and α_2 have to be carefully chosen in order to obtain distributions which significantly differ from the SM one. α_0 and α_2 are shifted from the SM value by $\Delta\alpha = |\alpha_1 - \alpha_{0,2}|$ ranging from 0.15 to 1, depending on how fast the cross section varies with a given parameter α .

4.4.3 Azimuthal Asymmetry

The sensitivity to deviations from the SM value for the azimuthal asymmetry can be obtained with the same method described in 4.4.2. In this case the integrated azimuthal asymmetry σA_T is studied:

$$\sigma A_T = \int_{-1}^{\cos\theta'} \frac{d(\sigma A_T)}{d\cos\theta} d\cos\theta \quad (4.4)$$

In order to obtain the maximum sensitivity to σA_T it is necessary to find the value of $\cos\theta'$ at which the significance $\sigma A_T/\Delta(\sigma A_T)$ is large. Figures 4.7 and 4.8 show the azimuthal asymmetry σA_T of the ϕ -distribution of the W^- bosons and the corresponding statistical error bars as a function of the cut in $\cos\theta$ (Eq. 4.4). Here the error $\Delta(\sigma A_T)$ is given by the statistical error of the ϕ -distribution. If the whole range of $\cos\theta'$ is considered, then the contribution from the t-channel dominates over the s-channel one as one approaches $\cos\theta' = 1$. Here the W -pair production cross section

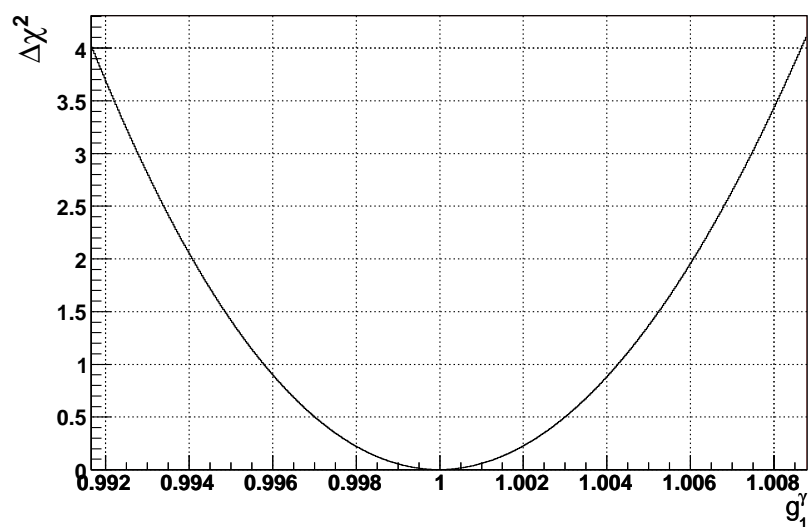


Figure 4.6: $\Delta\chi^2$ curve employed to determine the sensitivity to anomalous values of Δg_1^γ . The curve is obtained from the comparison of $\cos\theta$ distributions for anomalous values of Δg_1^γ with the SM distribution.

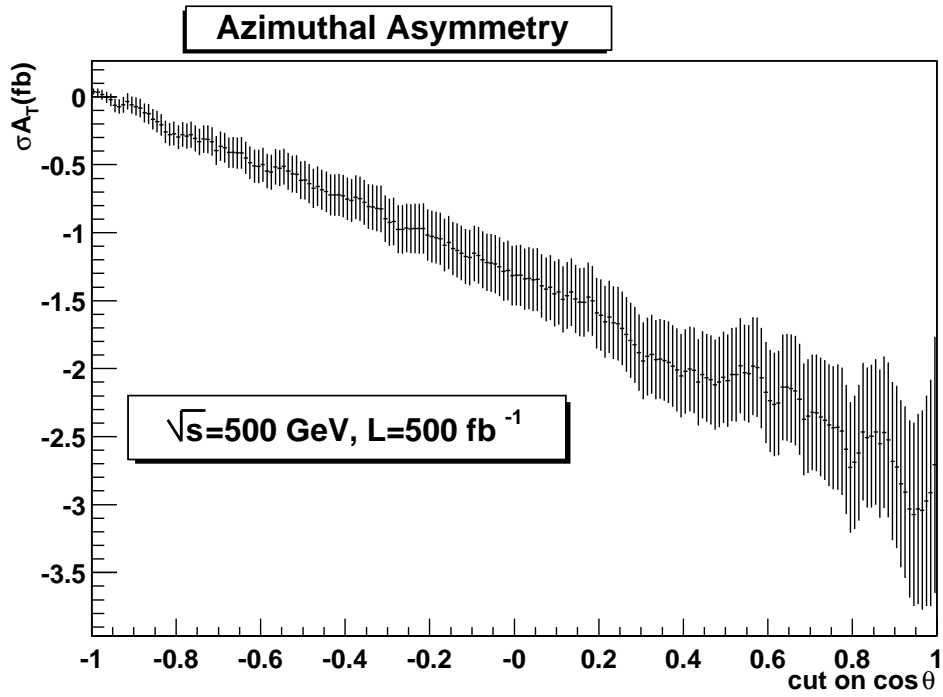


Figure 4.7: Azimuthal asymmetry σA_T of the ϕ -distribution of the W^- bosons and the corresponding statistical error bars as a function of the cut in $\cos \theta$ (Eq. 4.4).

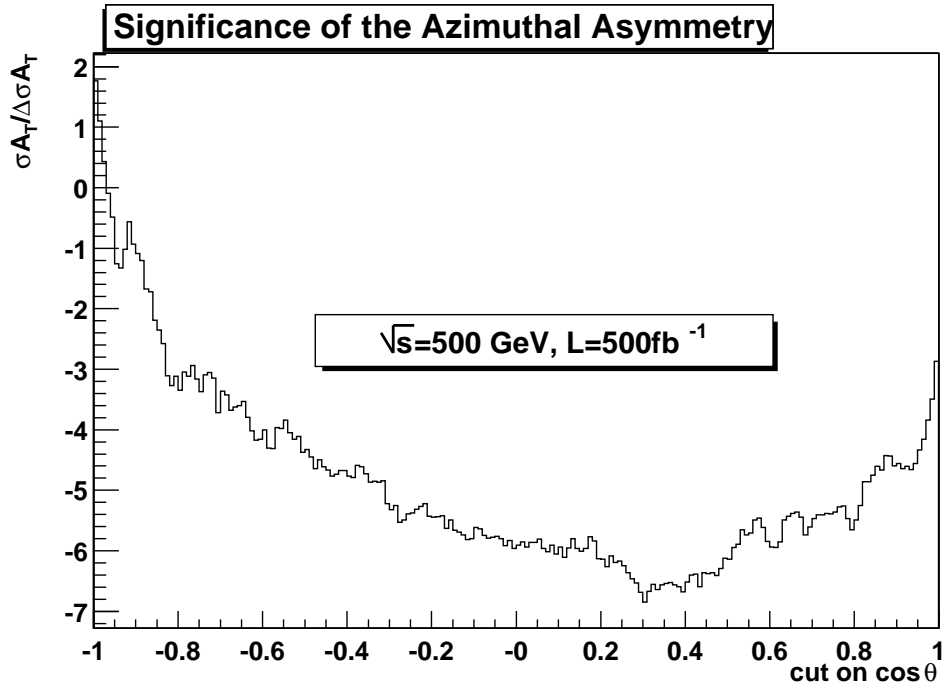


Figure 4.8: Significance of the azimuthal asymmetry σA_T as a function of the cut in $\cos \theta$ (Eq. 4.4).

is larger, and the contributions from the s-channel to the asymmetry, are suppressed.

The value of σA_T (Eq. 4.4) is obtained in the following way: A ϕ -distribution histogram is generated employing the cut $-1 \leq \cos \theta \leq \cos \theta'$, and finally σA_T is computed as $\sigma A_T = \sum_i n_i \cos 2\phi_i$, where n_i is the i -th bin content of the ϕ -distribution and ϕ_i is the value of ϕ in the middle of the i -th bin. As an example the dependence of σA_T on λ_γ and the corresponding error band is shown in Fig. 4.9. The reference distributions employed to construct this graph are the same used to construct the $\Delta\chi^2$ graph from which the sensitivity to anomalous TGCs is obtained.

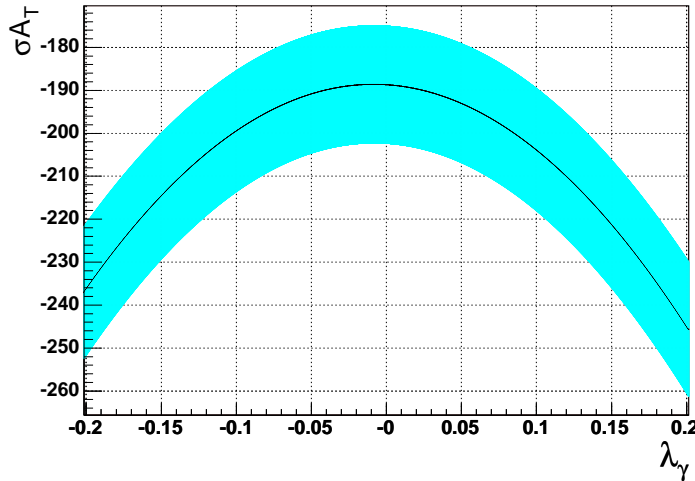


Figure 4.9: Dependence of the azimuthal asymmetry σA_T on λ_γ and the corresponding statistical error band. The reference distributions employed to construct this graph are the same used to construct the $\Delta\chi^2$ graph from which the sensitivity to anomalous TGCs is obtained.

4.5 Results

The 1σ -bound to anomalous TGCs for the case of transverse beam polarization is shown in Table 4.3 for the $\cos \theta$ and ϕ observables as well as for 2-D $\cos \theta - \phi$ distributions. From the entries in Table 4.3 it can be concluded that for this beam polarization

mode the $\cos\theta$ -distribution offers the best possibility to detect the existence of anomalous TGC. The 1σ -bound ranges from 1.0×10^{-3} for $\Delta\kappa_\gamma$, to 39.0×10^{-3} for $\tilde{\kappa}_\gamma$. Similar values are obtained for the $\cos\theta - \phi$ distribution, while the values for the ϕ distribution are typically a factor 2-3 larger. Thus the $\cos\theta$ distribution is equivalent in the cases of unpolarized and transversely polarized beams. The consistency of the method used to compute the 1σ -bound is verified by the procedure described in Appendix A. The 1σ -bound obtained for the cases of transverse and longitudinal beam polarization from the $\cos\theta$ distribution is shown in Table 4.4. For longitudinal beam polarization there is no ϕ -angle dependence of the cross section (Sec. 4.2). The 1σ -bound takes values between 0.4×10^{-3} and 21.0×10^{-3} for $\Delta\kappa_\gamma$ and $\tilde{\kappa}_\gamma$ respectively. Table 4.4 presents in addition 1σ -bound for the azimuthal asymmetry σA_T .

The smallest values of the 1σ -bound are obtained from longitudinally polarized beams (80%,-60%) since already small deviations from the SM for the corresponding coupling constant lead to the required 1σ deviations of the cross section. For longitudinal beam polarization the contribution from the t-channel is strongly suppressed for the case of right-handed electrons and left-handed positrons; this fact allows to have a cleaner s-channel signal. For transverse polarization, the 1σ -bound for the azimuthal asymmetry is larger than the 1σ -bound for the angular distributions, as expected. The azimuthal asymmetry is computed for $-1 \leq \cos\theta \leq 0.5$ in order to have a large significance. In order to verify the results for each coupling constant α , the spread of the fitted values of 10 SM MC samples of 50 fb^{-1} is obtained and compared to the 1σ -bound. The fit of the 10 SM samples was made using the scaled reference curve employed to compute the 1σ -bound (see 4.4.2 and appendix A). For instance, in the case of anomalous \tilde{k}_Z , for the $\cos\theta$ -distribution the ratio of the value of the 1σ -bound and the spread of the fitted samples is 1.01. For the ϕ and $\cos\theta - \phi$ distributions the corresponding ratio is 1.04 and 1.09 respectively. The statistical compatibility of the computed 1σ -bound and the spread of the fitted values of the 10 MC samples, namely, the fact that both numbers almost coincide, is an indication for the consistency of the method employed.

4.6 Systematic Errors

The possible sources of systematic errors include: theoretical errors, uncertainty in the calculations of ISR and beamstrahlung, SM parameters (mainly the W mass) and the error in the measurements of beam polarization and energy. In [43] the sensitivity to

anomalous TGCs was investigated for the options of unpolarized and longitudinally polarized beams; there it was found that the issue of main concern is the error in the magnitude of the beam polarization. The size of the systematic errors obtained in that study for unpolarized beams can tell much about the corresponding quantities for the case of transverse polarization. The previous statement rests on the fact that, assuming leptonic chiral symmetry and massless electrons, the average of the transverse polarization cross section over the azimuthal angle ϕ is equal to the unpolarized cross section[39]. In [43] the values for the systematic errors vary from 1.6×10^{-4} for λ_Z to 35.8×10^{-4} for Δg_1^Z , while the statistical errors range from 4.8×10^{-4} for $\Delta \kappa_\gamma$ to 85.8×10^{-4} for g_4^Z .

4.7 Summary and Conclusion

Transverse beam polarization can not compete with longitudinal polarization regarding sensitivity to anomalous TGCs. The results obtained (Table 4.4) show that the largest sensitivity is observed for the case of longitudinal beam polarization for each coupling constant. The suppression of the t-channel ν -exchange for the case of longitudinal polarization gives the advantage over the other beam polarization modes. The superiority of longitudinal beam polarization over transverse polarization pointed out in this study is compatible with results obtained in a similar study presented in [34]. There, the method of optimal observables is employed taking into account the angles of the decay products from the W bosons. In addition, the simultaneous fit of several coupling constants in [34] provides more information than the one-parameter fit employed in this study.

	Δg_1^γ	Δg_1^Z	$\Delta \kappa_\gamma$	$\Delta \kappa_Z$	λ_γ	λ_Z	g_4^γ	g_4^Z
From $\cos\theta$ distribution	4.2	6.8	1.0	1.6	3.7	2.4	34.5	29.5
From ϕ distribution	10.7	18.2	25.8	4.4	12.4	4.0	50.2	43.2
From 2D $\cos\theta - \phi$ distribution	4.2	6.9	1.0	1.6	4.1	2.5	35.3	30.1

	g_5^γ	g_5^Z	$\tilde{\kappa}_\gamma$	$\tilde{\kappa}_Z$	$\tilde{\lambda}_\gamma$	$\tilde{\lambda}_Z$
From $\cos\theta$ distribution	32.2	27.4	39.0	33.0	4.9	3.5
From ϕ distribution	46.3	40.3	39.0	34.9	7.1	5.2
From 2D $\cos\theta - \phi$ distribution	34.1	27.7	39.0	33.0	4.6	3.3

Table 4.3: Expected 1σ -bound ($\times 10^{-3}$) for the case of transverse polarization(80%,60%) with the conditions $\sqrt{s} = 500$ GeV and a luminosity of 500 fb^{-1} . This numbers correspond to the semileptonic decay channel $e^+e^- \rightarrow W^+W^- \rightarrow \mu\nu_\mu q_1\bar{q}_2$.

	Δg_1^γ	Δg_1^Z	$\Delta \kappa_\gamma$	$\Delta \kappa_Z$	λ_γ	λ_Z	g_4^γ	g_4^Z
From Long.pol.(80%,-60%)	1.9	2.2	0.4	0.5	1.9	1.9	20.3	19.1
From Transv.pol.(80%,60%)	4.2	6.8	1.0	1.6	3.7	2.4	34.5	29.5
From σA_T (Transv.pol.(80%,60%))	193.0	109.0	4.5	40.0	15.3	10.6	93.0	79.0

	g_5^γ	g_5^Z	$\tilde{\kappa}_\gamma$	$\tilde{\kappa}_Z$	$\tilde{\lambda}_\gamma$	$\tilde{\lambda}_Z$
From Long.pol.(80%,-60%)	18.0	17.4	21.0	20.3	2.2	2.1
From Transv.pol.(80%,60%)	32.2	27.4	39.0	33.0	4.9	3.5
From σA_T (Transv.pol.(80%,60%))	91.0	82.3	108.0	94.0	11.0	6.5

Table 4.4: Expected 1σ -bound ($\times 10^{-3}$) for $\sqrt{s} = 500$ GeV and a luminosity of 500 fb^{-1} for the semileptonic decay channel $e^+e^- \rightarrow W^+W^- \rightarrow \mu\nu_\mu q_1\bar{q}_2$. This values, except the results on σA_T , were obtained from the $\cos\theta$ distribution.

Chapter 5

Precision Measurements of the Beam Polarization at the ILC Using Single- W Production

5.1 Introduction

The high statistical precision resulting from the ILC's high luminosity demands a very precise knowledge of the beam polarization, otherwise the size of the error coming from the uncertainty in the polarization will supersede the precision provided by the high luminosity. In the case of measurements of Triple Gauge-Boson Couplings TGCs in W -pair production. An error of the order of 0.1-0.2% (0.2-0.3%) for the electron(positron) beam polarization is necessary to have measurements which are not dominated by the polarization error [43]. A method proposed to measure the magnitude of the beam polarization at the ILC which has been studied is Compton polarimetry, providing an accuracy $\Delta P_{e^-}/P_{e^-} \approx 0.25\%$ [44]. That this number does not contain yet the effects of depolarization due to the beam-beam interactions or influence of the optics employed to make the necessary corrections in the case of a crossing angle different from the 0° design.

This study presents an alternative way for an in-situ measurement of the beam polarization. The central idea is to measure the polarization during the analysis of the physics events taking into account the dependence of the cross section on the polar-

ization. This implies that one has to choose the process for the measurement in such a way that factors which could induce an uncertainty coming from new physics can be controlled. A required feature is also a high cross section. An example of such a method is the Blondel scheme [45]. A study which applies the Blondel scheme to the Linear Collider case is presented in [41]. It is important to mention that the method studied here is intended to improve the precision in the determination of the beam polarization in the required cases and it is in no way a replacement of the polarimeters. The error of the polarization measurement using polarimeters is dominated by systematics, whereas the precision of the measurements using physics events is mainly of statistical nature.

A process which offers interesting properties is single- W production. The possibility to separate the background in an efficient way, a high cross section, the possibility of measuring the polarization of the electron and positron beam in an independent way and the minimum influence of anomalies in the values of Gauge-Boson coupling constants makes single- W production an attractive candidate.

5.2 Single- W Production

For this study the decay channel $W^- \rightarrow \mu^- \bar{\nu}_\mu$ ($W^+ \rightarrow \mu^+ \nu_\mu$) is considered. Therefore the attention is focused on the process $e^+e^- \rightarrow e^+\nu_e W^- \rightarrow e^+\nu_e \mu^- \bar{\nu}_\mu$ and the corresponding charge conjugate process. This four fermion final state contains contributions from a set of 18 diagrams which can be divided into two gauge invariant subsets. The first subset (s-channel) fig. 5.1, receives the largest contribution from the W -pair process, and the second one (t-channel) fig. 5.2, is dominated by the single- W^- process. In the case of single- W^+ production the electron (positron for the charge conjugated case) is predominantly scattered in the forward direction.

In order to be able to study the full phase space of the single- W^- (single- W^+) process it is necessary to generate events in which the final state positron (electron) is scattered at an angle down to 0 degrees. However, this condition is difficult to achieve due to theoretical as well as technical problems demanding a delicate treatment of the cross section calculations. The electron mass has to be considered finite in order to avoid a singularity at zero scattering angle. The introduction of a finite width for the W -boson causes an explosion of a gauge violating term when the electron polar angle approaches zero. This problem is partially remedied by introducing the so called “preserved gauge scheme”. More details are given in [46], [47] and [48]. For this study the Monte Carlo

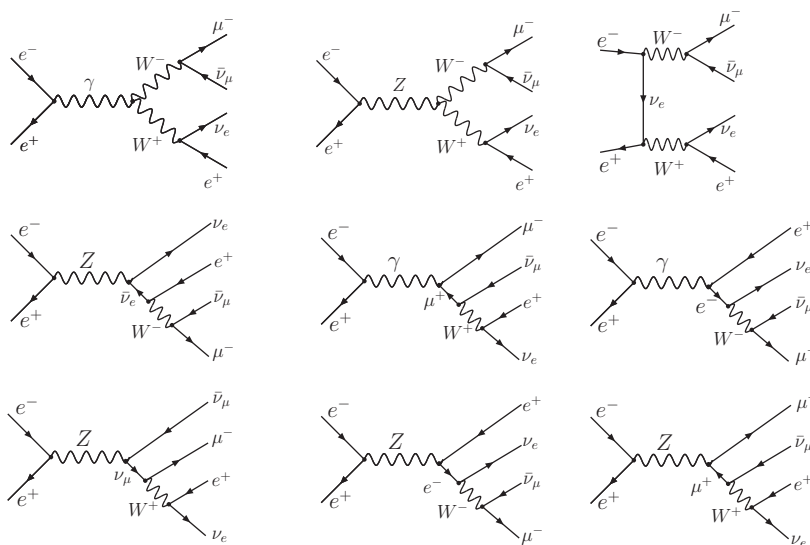


Figure 5.1: s-channel diagrams for the process: $e^+e^- \longrightarrow e^+\nu_e\mu^-\bar{\nu}_\mu$.

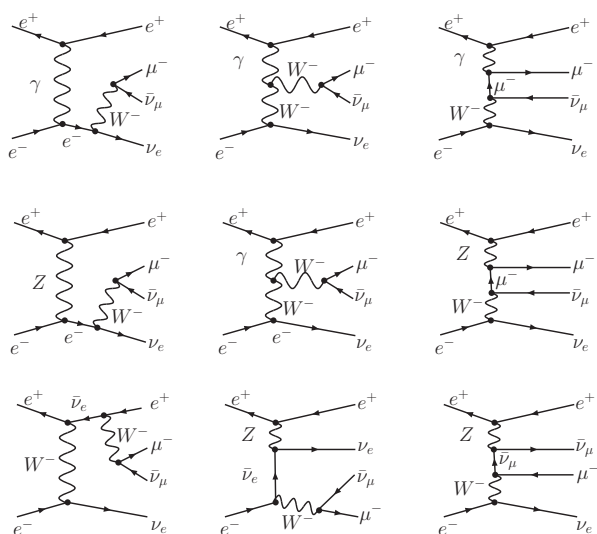


Figure 5.2: t-channel diagrams for the process: $e^+e^- \longrightarrow e^+\nu_e\mu^-\bar{\nu}_\mu$.

generator WHIZARD [38] was chosen as the single- W generator. Comparisons with other two fully massive 4-fermion generators are performed (Section 5.3).

5.3 Single- W Generators

Comparisons between 4-fermion generators which try to solve the problems described in section 5.2 have been made in the past. Most of the attention has been centered on the hadronic decay channel: $e^+e^- \rightarrow e^-\bar{\nu}_e u \bar{d}$ [48]. In this study a comparison of three fully massive 4-fermion generators: WHIZARD [38], KoralW and grc4f is made for the process $e^+e^- \rightarrow e^+\nu_e W^- \rightarrow e^+\nu_e \mu^- \bar{\nu}_\mu$. The features of these generators are shown in Table 4.2.

The value of the total cross section for unpolarized beams obtained without cuts on the positron polar angle θ (for the input parameters shown in Appendices C,D and E) are shown in Table 5.1. The number of events corresponding to a luminosity of 500fb^{-1} for the following cuts are also shown in Table 5.1:

- a) No cuts on $\cos\theta$ and input parameters as shown in Appendices C,D and E.
- b) $\cos\theta < -0.993$ (single- W region) and input parameters as shown in Appendices C,D and E.

	WHIZARD	KoralW	grc4f
Cross section(fb)	445.35 ± 0.94	444.90 ± 7.58	477.92 ± 1.87
Number of events			
a) No cuts	222679	223410	238855
b) $\cos\theta < -0.993$	148772	49776	171749

Table 5.1: Total cross section and number of events for single- W^- for a luminosity of 500fb^{-1} (unpolarized beams).

The dependence of the cross section on the polar angle θ for the three generators is shown in Fig. 5.3. WHIZARD and grc4f broadly agree, but the KoralW distribution differs strongly from the other two generators. Note that the difference in the shape of the distributions is much more pronounced than the difference in the value of the cross section.

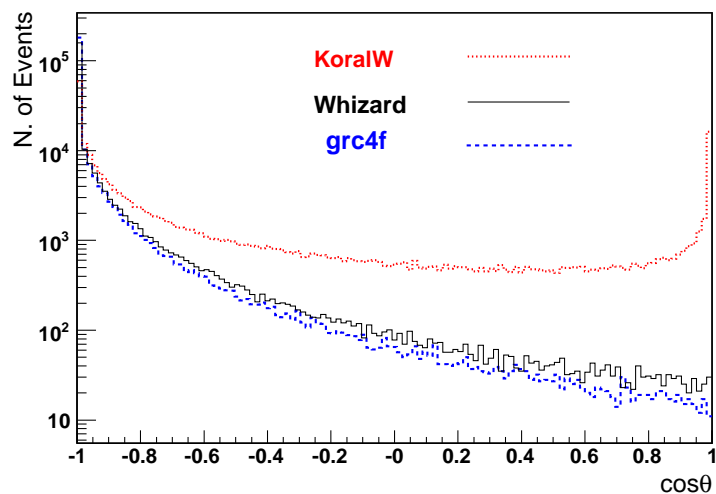


Figure 5.3: $\cos\theta$ distributions of the e^+ for the $e^+\nu_e\mu^-\bar{\nu}_\mu$ final state from the three 4-fermion generators.

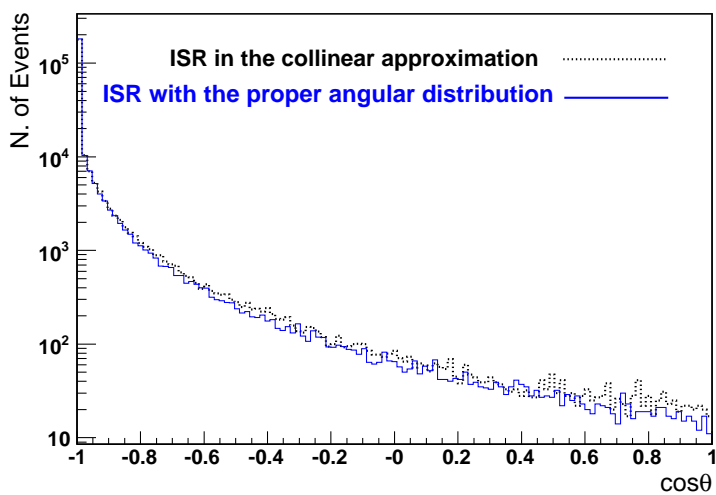


Figure 5.4: $\cos\theta$ distributions of the e^+ for the $e^+\nu_e\mu^-\bar{\nu}_\mu$ final state from the **grc4f** generator employing two types of ISR calculations.

The `grc4f` can treat the ISR in the collinear approximation as well as with the proper angular distribution. The two methods are compared in Fig. 5.4, where the positron polar angle distributions obtained with both methods are shown. Employing the collinear approximation method the resulting cross section is 468.80 fb and for the second method it is 477.92 fb. Here one can notice that the difference among different generators (Fig. 5.3) is much larger than the difference between the two treatments of ISR provided by `grc4f` (see Fig. 5.4 and Table 5.1). Comparisons between `KoralW` and `Grace` have been made in the past, but there is still a number of unresolved issues which have to be studied in more detail by the theorists [60]. `WHIZARD` is selected as the 4-fermion generator because it includes the polarization option and also simulates beamstrahlung with the aid of `Circe`.

5.4 Measuring the Beam Polarization

The cross section $\sigma(P_{e^-}, P_{e^+})$ for a given physical process in terms of the electron and positron beam polarization, P_{e^-} and P_{e^+} respectively, can be written as:

$$\begin{aligned} \sigma(P_{e^-}, P_{e^+}) = \frac{1}{4} \left\{ (1 + P_{e^-})(1 + P_{e^+})\sigma_{RR} + (1 - P_{e^-})(1 - P_{e^+})\sigma_{LL} \right. \\ \left. + (1 + P_{e^-})(1 - P_{e^+})\sigma_{RL} + (1 - P_{e^-})(1 + P_{e^+})\sigma_{LR} \right\}. \end{aligned} \quad (5.1)$$

Where σ_{LL} denotes the cross section for 100% left-handed electron polarization and 100% left-handed positron polarization. The same scheme applies for defining σ_{LR} , σ_{RL} and σ_{RR} . In the case of single- W^- production the $e^- \nu_\mu W^-$ vertex can occur only if the electron is left-handed, hence the cross section vanishes for right handed electrons ($\sigma_{RR} = \sigma_{RL} = 0$). As a result, the cross section for single- W^- production $\sigma_{(W^-)}$ depends only on the electron beam polarization:

$$\sigma_{(W^-)}(P_{e^-}, P_{e^+}) = \frac{1}{4}(1 - P_{e^-})(\sigma_{LL} + \sigma_{LR}).$$

By changing the sign of the electron beam helicity one obtains the cross sections

$$\sigma_{(W^-)\pm} = \sigma_{W^-}(\pm|P_{e^-}|, P_{e^+}) = \frac{1}{4}(1 \pm |P_{e^-}|)(\sigma_{LL} + \sigma_{LR}). \quad (5.2)$$

From this two cross sections one immediately obtains the absolute value of the electron beam polarization:

$$|P_{e^-}| = \left| \frac{\sigma_{(W^-)_+} - \sigma_{(W^-)_-}}{\sigma_{(W^-)_+} + \sigma_{(W^-)_-}} \right|. \quad (5.3)$$

In the same way it is possible to obtain the positron beam polarization considering this time the cross section for single- W^+ production $\sigma_{(W^+)}$, which vanishes for left-handed positrons ($\sigma_{LL} = \sigma_{RL} = 0$). In this case one has

$$|P_{e^+}| = \left| \frac{\sigma_{(W^+)_+} - \sigma_{(W^+)_-}}{\sigma_{(W^+)_+} + \sigma_{(W^+)_-}} \right|. \quad (5.4)$$

5.5 Conditions of the Study and Analysis

The following conditions are assumed for this study: a center-of-mass energy of 500 GeV, a luminosity of 500 fb^{-1} and longitudinal beam polarization (80% for electrons and 60% for positrons). The Monte Carlo (MC) samples are generated with WHIZARD and the two-fermion generator KK including initial state radiation (ISR) and beamstrahlung. The detector response is simulated with the fast detector simulation SIMDET. The luminosity is split into equal parts for each beam polarization configuration:

- a) 80% right electrons and 60% left positrons (+0.8,-0.6),
- b) 80% left electrons and 60% right positrons (-0.8,+0.6).

According to the properties of a single- W event for the decay channel considered in this study (Section 5.2) one can identify a signal event by demanding the electron to be scattered outside the tracker acceptance. In other words, we define a single- W^- (single- W^+) event by the following conditions:

- A)** A single reconstructed (charge identification is assumed) muon (anti-muon) in the detector. The assumed tracker acceptance and general tracker efficiency are $|\theta_{Tracker}| > 7^\circ$ and $\text{Eff}_{Trk} = 0.99$ respectively.
- B)** No further detector activity. The Condition: $E_\mu/E_{Detector} > 0.97$ (where E_μ is the reconstructed energy of the muon and $E_{Detector}$ is the total visible energy in the detector) is applied in order to filter events where a second charged particle at low angle escapes the tracker acceptance but deposits energy in the calorimeters.

For the set of cuts defined above the following processes act as a background:

- I) $W^+W^- \longrightarrow e^+\nu_e\mu^-\bar{\nu}_\mu$
- II) $\mu^+\mu^-$
- III) $\mu^+\nu_\mu\mu^-\bar{\nu}_\mu$
- IV) $\tau^+\tau^- \longrightarrow e^+\nu_e\bar{\nu}_\tau\mu^-\bar{\nu}_\mu\nu_\tau$
- V) $\tau^+\tau^- \longrightarrow \mu^+\nu_\mu\bar{\nu}_\tau\mu^-\bar{\nu}_\mu\nu_\tau$
- VI) $\tau^+\nu_\tau\tau^-\bar{\nu}_\tau \longrightarrow \mu^+\nu_\mu\bar{\nu}_\tau\nu_\tau\mu^-\bar{\nu}_\mu\nu_\tau\bar{\nu}_\tau$
- VII) $e^+e^-\mu^+\mu^-$

The corresponding charge conjugate events play the role of the background for the measurement of single- W^+ events. The two-fermion generator KK is used to generate the background events II, IV and V. For the remaining process WHIZARD is used. The error on the measurement of the electron and positron beam polarization ΔP_{e^\pm} is obtained by Gaussian error propagation from Eq. 5.3:

$$\Delta^2 P_{e^\pm} = 4 \frac{\sigma_{(W^\pm)-}^2 \Delta^2 \sigma_{(W^\pm)+} + \sigma_{(W^\pm)+}^2 \Delta^2 \sigma_{(W^\pm)-}}{(\sigma_{(W^\pm)+} + \sigma_{(W^\pm)-})^4}, \quad (5.5)$$

where $\Delta\sigma_{(W^\pm)\pm}$ includes the contribution to the error coming from the background. The dependence of ΔP_{e^\pm} on the distribution of the luminosity among the two different beam polarization modes is studied by scaling the number of events.

5.6 Results

By demanding the identification of a single muon (Condition A as defined above) and minimizing the activity in the detector by the condition: $E_\mu/E_{Detector} > 0.97$ (Condition B as defined above) the expected relative statistical error for the electron and positron beam polarization for a luminosity of 500 fb^{-1} was found to be:

$$\Delta P_{e^-}/P_{e^-} = 0.26\%$$

$$\Delta P_{e^+}/P_{e^+} = 0.33\%$$

In the case of a luminosity of 1 ab^{-1} the expected relative errors for the electron and positron beam polarization are 0.19% and 0.23% respectively. The number of events

Measuring electron beam polarization:

PROCESS	N.evt. (+80,-60)		N.evt. (-80,+60)	
	Cond. A	Cond. A and B	Cond. A	Cond. A and B
single- W^- (signal)	13390	9784	123170	88656
$W^+W^- \rightarrow e^+\nu_e\mu^-\bar{\nu}_\mu$	220	1	6955	29
$\mu^+\mu^-$	15987	1848	16748	1852
$\mu^+\nu_\mu\mu^-\bar{\nu}_\mu$	238	162	5372	4512
$\tau^+\tau^- \rightarrow e^+\nu_e\bar{\nu}_\tau\mu^-\bar{\nu}_\mu\nu_\tau$	902	45	933	46
$\tau^+\tau^- \rightarrow \mu^+\nu_\mu\bar{\nu}_\tau\mu^-\bar{\nu}_\mu\nu_\tau$	478	55	467	50
$\tau^+\nu_\tau\tau^-\bar{\nu}_\tau \rightarrow \mu^+\nu_\mu\bar{\nu}_\tau\nu_\tau\mu^-\bar{\nu}_\mu\nu_\tau\bar{\nu}_\tau$	342	10	7712	200
$e^+e^-\mu^+\mu^-$	265133	174	265316	171

Measuring the positron beam polarization:

PROCESS	N.evt. (+80,-60)		N.evt. (-80,+60)	
	Cond. A	Cond. A and B	Cond. A	Cond. A and B
single- W^+ (signal)	26423	19405	107332	78373
$W^+W^- \rightarrow e^+\nu_e\mu^-\bar{\nu}_\mu$	264	1	8888	33
$\mu^+\mu^-$	15808	1835	16195	1795
$\mu^+\nu_\mu\mu^-\bar{\nu}_\mu$	221	153	5377	4533
$\tau^+\tau^- \rightarrow e^+\nu_e\bar{\nu}_\tau\mu^-\bar{\nu}_\mu\nu_\tau$	880	38	916	50
$\tau^+\tau^- \rightarrow \mu^+\nu_\mu\bar{\nu}_\tau\mu^-\bar{\nu}_\mu\nu_\tau$	434	40	449	44
$\tau^+\nu_\tau\tau^-\bar{\nu}_\tau \rightarrow \mu^+\nu_\mu\bar{\nu}_\tau\nu_\tau\mu^-\bar{\nu}_\mu\nu_\tau\bar{\nu}_\tau$	351	8	7677	218
$e^+e^-\mu^+\mu^-$	268559	192	274681	146

Table 5.2: Number of events for the signal and background for a luminosity of 250 fb^{-1} for each polarization mode. The condition A means: A single reconstructed (charge identification is assumed) muon (anti-muon) is found in the detector. The condition B demands the cut: $E_\mu/E_{Detector} > 0.97$ (where E_μ is the reconstructed energy of the muon and $E_{Detector}$ is the total visible energy in the detector).

Purity for single- W^-

	Cond. A	Cond. A and B
(+80,-60)	4.5%	44.7%
(-80,+60)	29.7%	48.1%

Purity for single- W^+

	Cond. A	Cond. A and B
(+80,-60)	8.4 %	47.2%
(-80,+60)	26.2%	47.9%

Table 5.3: Purity of the single- W^\pm signal, where the condition A means: A single reconstructed (charge identification is assumed) muon (anti-muon) is found in the detector. The condition B demands the cut: $E_\mu/E_{Detector} > 0.97$ (where E_μ is the reconstructed energy of the muon and $E_{Detector}$ is the total visible energy in the detector).

for the signal and background processes before and after applying the Condition B: $E_\mu/E_{Detector} > 0.97$ are shown in Table 5.2. The effect of this cut on the purity¹ of the signal can be appreciated in Table 5.3. Additional cuts on the polar angle and energy of the muons do not provide significant additional precision. As an example, if an additional cut $20 \text{ GeV} < E_\mu < 180 \text{ GeV}$ on the muon's energy is introduced $\Delta P_{e^-}/P_{e^-}$ decreases negligibly (by 0.001%) but $\Delta P_{e^+}/P_{e^+}$ increases by 0.008%. Furthermore, if a cut $|\cos \theta_\mu| < 0.98$ is added $\Delta P_{e^-}/P_{e^-}$ increases by 0.003%. All these values were obtained for the case of equally shared luminosity between the two beam polarization modes mentioned in the previous section. In the Figures 5.5 and 5.6 one can appreciate the behavior of the relative error of the electron and positron polarizations as a function of the luminosity shared by the two beam polarization modes. Here n is the fraction of the luminosity assigned to the (+80%,-60%) polarization mode ($1 - n$ for the (-80%,+60%) mode).

¹We define the purity of the signal as $N_S/(N_S + N_B)$, where $N_S(N_B)$ is the number of signal(background) events.

5.7 Systematic Errors

The complications in the calculations of the signal events (mainly in the vicinity of zero electron scattering angle) mentioned in Section 5.2 manifested in the discrepancy among generators exposed in Section 5.3. However, for the purpose of measuring the degree of beam polarization this source of systematic errors cancel (they are contained in the factor $\sigma_{LL} + \sigma_{LR}$ of Equation 5.2). The uncertainty in the signal cross section only influences the precision of the polarization measurement at the level of statistical information. Other sources of systematic errors are the calculations describing the background processes (two and four fermion final states), which in most cases are well understood. It is possible to obtain a rough estimation of the results produced by employing the KoralW generator instead of WHIZARD even though it cannot generate events using polarized beams. For this, two assumptions are made: a) The calculations employed to generate the W -pair background events are not as delicate as for the single- W case and therefore it is only necessary to replace the t-channel events. b) The new number of signal events (detector level) is obtained by scaling the old number by the factor N_{KW}^{GL}/N_W^{GL} , where N_{KW}^{GL} is the number of KoralW unpolarized signal events at generator level having the electron or positron polar angle outside the tracker acceptance angle and N_W^{GL} is the corresponding number for WHIZARD. This follows from the fact that the polarized cross section for single- W^\pm production is obtained from the unpolarized one just by multiplying by the factor: $1 \pm P_{e^\pm}$. The relative error in the electron polarization measurement using this approximation shifts from 0.26% (WHIZARD) to roughly 0.5% (KoralW approximation). In the case of the positron polarization measurement the relative error changes from 0.33% to 0.6%.

5.8 Conclusions

The precision in the value of the electron and positron beam polarization obtained in this study from the single- W production process makes it an attractive candidate for such a measurement. The obtained values reach the current precision offered by Compton polarimetry (specially if a luminosity larger than 500 fb^{-1} is available for the measurement) and are already free of depolarization effects. Considering in addition other W -decay channels might help to reduce further the error on the polarization.

The selection method is efficient and easy, in addition the low number of W -pair events which survive the selection makes the influence of anomalous TGCs negligible considering that in the case of the signal the deviations due to TGCs cancels for the

asymmetry expressions 5.3 and 5.4. In general, the theoretical errors in the case of the signal processes do not influence significantly the result because the values of σ_{LL} , σ_{LR} , σ_{RL} and σ_{RR} cancel in 5.3 and 5.4.

The behavior of the polarization error as a function of the luminosity sharing between the two polarization modes (+80%,-60%) and (-80%,+60%) favors the configuration in which most of the luminosity is spent for right handed electrons and left handed positrons (+80%,-60%) (Figs. 5.5 and 5.6). If 90% of the luminosity is used for the running with right handed electrons and left handed positrons, a relative error of 0.25%(0.40%) for the electron(positron) beam polarization is expected. This is very convenient for cases in which W -pair production represents one of the main backgrounds (i.e. Higgs physics). In the opposite case, namely when 10% of the luminosity is used for the running with right handed electrons and left handed positrons, a relative error of 0.55%(0.68%) for the electron(positron) beam polarization is expected. For the last case, if a total luminosity of 1 ab^{-1} is used for the measurement the expected error is 0.39% for the electron beam polarization and 0.48% for the positron beam polarization.

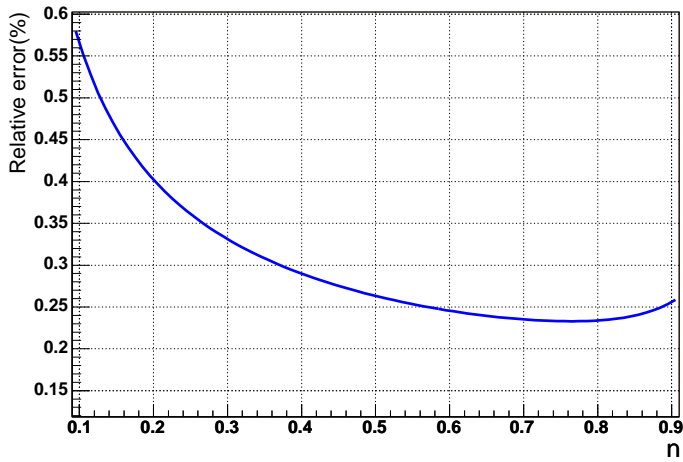


Figure 5.5: Relative error of the electron polarization as a function of the luminosity (500fb^{-1}) shared by the two beam polarization modes. Here n is the fraction of the luminosity assigned to the $(+80\%, -60\%)$ polarization mode ($1 - n$ for the $(-80\%, +60\%)$ mode).

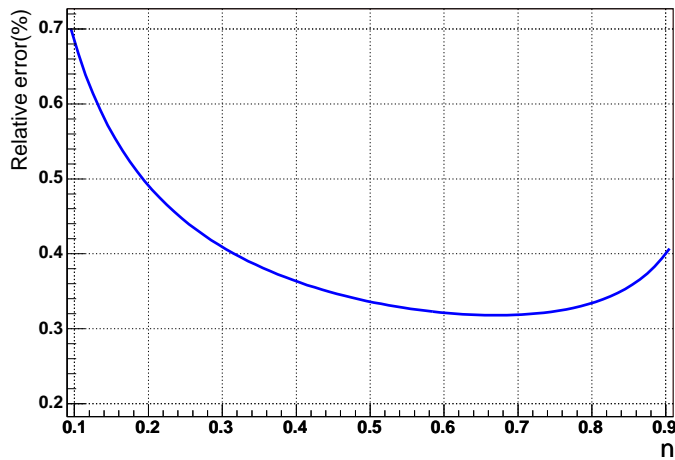


Figure 5.6: Relative error of the positron polarization as a function of the luminosity (500fb^{-1}) shared by the two beam polarization modes. Here n is the fraction of the luminosity assigned to the $(+80\%, -60\%)$ polarization mode ($1 - n$ for the $(-80\%, +60\%)$ mode).

Chapter 6

Polarized Positrons at the E-166 Experiment

6.1 Aim of the Experiment

The advantages of having both beams polarized at the ILC have been discussed in Chapter 2. Until now, only electron beam polarization has been employed in e^+e^- colliders, namely at the SLAC Linear Collider where the electron beam polarization was fundamental to improve the precision of the measurements [61]. It is necessary to prove the possibility of producing a polarized positron beam with the characteristics required by the ILC physics program. Briefly described, the method proposed to generate polarized positrons consists in shooting circularly polarized photons into a thin target to produce e^+e^- pairs. In this process the circular polarization of the photons is transferred into longitudinal polarization of the positrons. The polarized photons are produced by passing a 150-250 GeV (in the case of the ILC) electron beam through a helical undulator. An alternative method to produce circularly polarized photons is being tested at KEK [64]. In this case the photons are produced by Compton backscattering of a YAG laser and an electron beam with an energy around 1 GeV.

The main point of the E-166 experiment at SLAC is to produce longitudinally polarized positrons and test the whole process of polarization transfer mentioned above. The cross section which describes the basic process of polarization transfer was derived in the late 1950's [62], but the behavior of the polarization transfer along a complete

electromagnetic cascade still has to be experimentally measured. In the following sections the processes involved in the production of polarized positrons will be described in more detail, as well as the way in which the degree of polarization would be measured and the general structure of the E-166 experiment.

6.2 Interaction of Particles with Matter

At the E-166 experiment a variety of interaction processes occur in the chain γ -positron/electron- γ -conversion, and at the absorption polarimetry devices. In this section a brief review of the relevant processes of interaction of radiation with matter for the E-166 experiment is made. The charged particles traversing matter suffer energy loss due to the following mechanisms [9, 65]:

Ionization. Ionization is the main source of energy loss for low energetic electrons (less than approximately 10 MeV) Above 10 MeV the energy loss by ionization decreases steeply and bremsstrahlung is the dominating process (see Fig. 6.1). In a detector, electrons created by ionization can be collected by means of an electric field and yield an electric signal.

Atomic excitation. The light emitted from the de-excitation can be also used as a calorimeter signal (scintillation).

Čerenkov radiation. By selecting the adequate refraction index of the medium, Čerenkov detectors can be used as threshold counters.

Bremsstrahlung. Bremsstrahlung is the main source of electron energy loss for energies around 100 MeV or even less for some materials.

The Bethe-Bloch formula [9, 10] describes the energy loss $-dE/dx$ of moderately relativistic charged particles in matter, mainly due to ionization and atomic excitation:

$$-\frac{dE}{dx} = Kz^2 \frac{Z}{A} \frac{1}{\beta^2} \left[\frac{1}{2} \ln \frac{2m_e c^2 \beta^2 \gamma^2 T_{max}}{I^2} - \beta^2 - \frac{\delta}{2} - \frac{C(\beta\gamma)}{Z} \right].$$

Here $K = 4\pi N_A r_e^2 m_e c^2$, where N_A is the Avogadro's number, m_e the mass of the electron, r_e is the classical electron radius, A the atomic mass of the absorber, z is the charge of the incident particle, Z the atomic number of the absorber, I is the mean excitation energy, β is the velocity of the particle and $\gamma = (1 - \beta^2)^{-1/2}$, T_{max} is the maximum kinetic energy which can be imparted to a free electron in a single collision, δ is the density effect correction to ionization energy loss and C is the shell correction

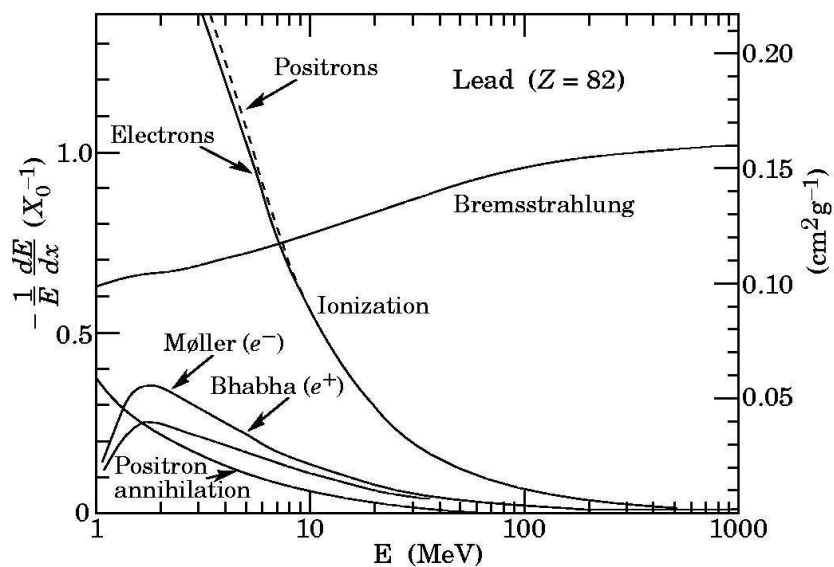


Figure 6.1: Fractional energy loss per radiation length in lead as a function of electron or positron energy [9].

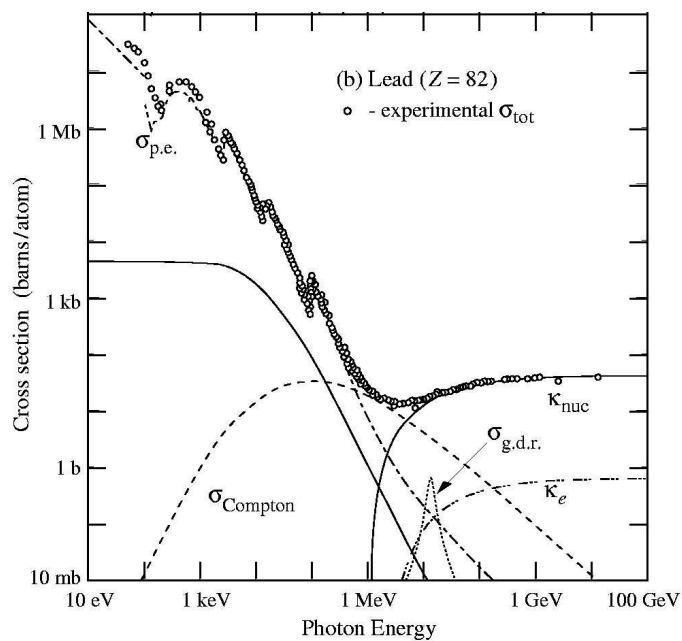


Figure 6.2: Photon total cross sections for different processes in lead [9].

parameter. The fractional energy loss for electrons or positrons per radiation length¹ for lead is shown in Fig. 6.1. The behavior is similar for other materials. Photons interact with matter by means of the following mechanisms:

Photoelectric effect. The photoelectric cross section largely depends on the available number of electrons (Z value of the absorber material).

Rayleigh scattering. In this process the photon does not lose energy, therefore only the spatial distribution of the energy is affected.

Compton scattering. In this case the photon is scattered by an atomic electron transferring the sufficient fraction of the momentum and energy to put the electron in an unbound state.

Pair production. The $\gamma \rightarrow e^+e^-$ reactions are caused by nuclear electromagnetic fields. At high energies pair production dominates over other photon interaction processes (Fig. 6.2).

6.3 Polarized Positron Production

As it was mentioned in the previous section, the first step in the production of polarized positrons consist in the production of circularly polarized photons. In the E-166 experiment this is achieved by passing a low emittance 50 GeV beam through a helical undulator. This photons are converted into electron-positron pairs when interacting with the material of a thin target. The positrons (and the electrons) “inherit” the polarization of the photons in form of longitudinal polarization. The desired positron momentum is selected by a spectrometer. At the end, the polarization of the positrons is analyzed using a polarimeter. The polarization of the photons produced in the helical undulator is also controlled with the help of a polarimeter, see Fig. 6.3. The production of polarized photons and the conversion into longitudinally polarized positrons are described in the following sub-sections.

6.3.1 Production of Circularly Polarized Photons

The undulator field induces the emission of γ -photons by the passing electrons; this photons are produced by backscattering of a beam electron off the virtual photon of the undulator field. The polarization of the undulator field is acquired by the emitted

¹Radiation length is the mean distance over which a high-energy electron loses all but $1/e$ of its energy by bremsstrahlung.

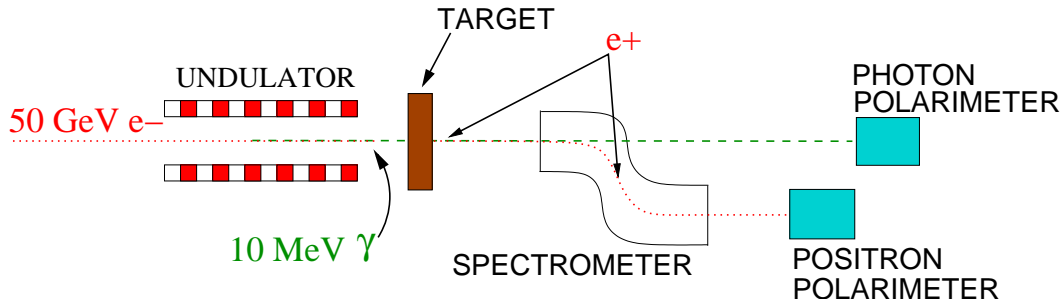


Figure 6.3: Conceptual layout of the E-166 experiment at SLAC.

photons which have the largest value of the energy, which are emitted at 0° with respect to the electron beam. Applications of helical undulators for the generation of circularly polarized photons are described in [42, 66, 67].

Energy of the photons. The energy of the most energetic emitted photons is to a first approximation:

$$E_0 \approx \frac{2\gamma^2 hc}{\lambda_u} = 24[\text{MeV}] \frac{(E_e/50[\text{GeV}])^2}{\lambda_u[\text{mm}]} \quad (6.1)$$

where $E_e = \gamma mc^2$ is the beam electron energy, and λ_u is the undulator period. Assuming an energy of 50 GeV for the SLAC beam electrons, an undulator period of 2.4 mm is required in order to obtain polarized photons with an energy of 10 MeV. The photon cross section reaches the minimum value around 10 MeV (Fig. 6.2).

Intensity of the photon radiation. The number of photons emitted per meter of undulator dN_γ/dL depends on the intensity of the virtual photons of the undulator field, which at the same time depends on the square of the magnetic field strength. An approximation to the number of photons per meter of undulator length is

$$\frac{dN_\gamma}{dL} = \frac{4\pi\alpha}{3\lambda_u} \frac{K^2}{1+K^2} \text{ photons}/m/e^-, \quad (6.2)$$

where the undulator parameter K is a dimensionless parameter defined as:

$$K = \frac{2\pi B_o \lambda_u}{mc^2} = 0.09 B_o[T] \lambda_u[\text{mm}], \quad (6.3)$$

Here B_o is the peak transverse magnetic field in the undulator. The expression 6.2 is only valid for small values of K . From the required values for the undulator period

mentioned above, the highest achievable value of K is about 0.2; in this case the number of photons emitted per electron in a 1-meter-long undulator is about 0.2. The photon number spectrum for the proposed experimental parameters: $E_e = 50$ GeV, $\lambda_u = 2.4$ mm and $K = 0.17$ is shown in Fig. 6.3.1.

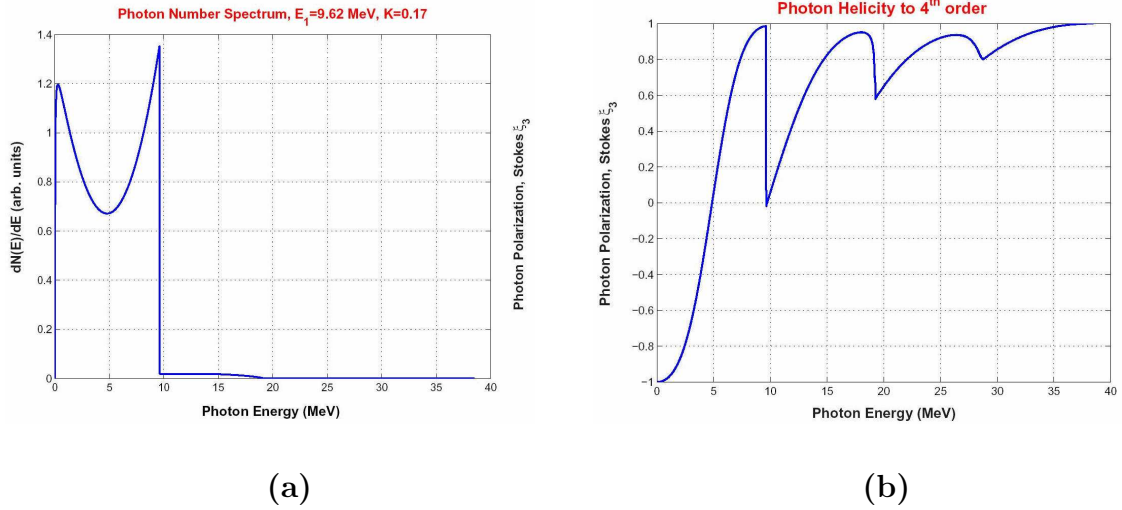


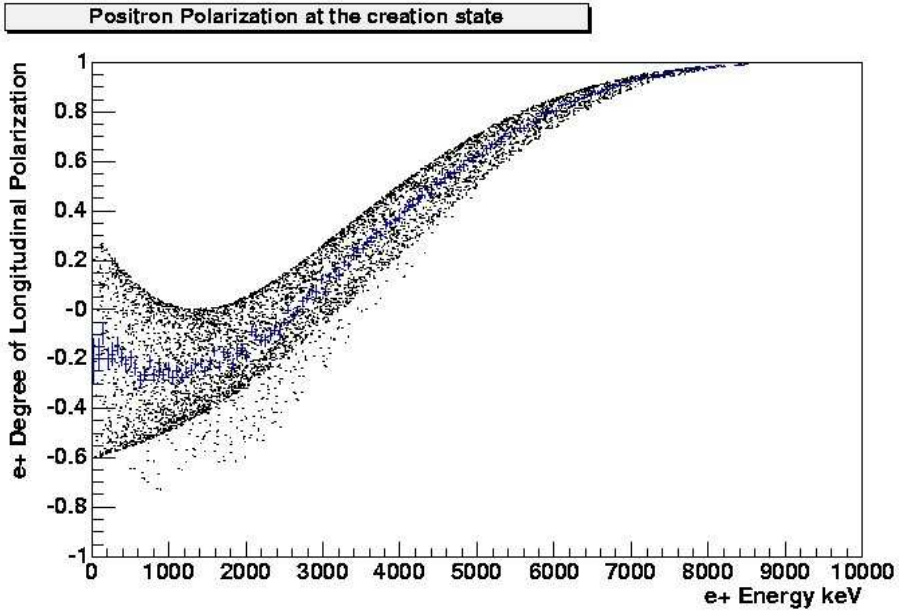
Figure 6.4: (a) Photon number spectrum(intensity spectrum of undulator radiation integrated over angle). (b) Dependence of the polarization P_γ on the photon energy E_γ .

Angular dependence of the energy of the photons.

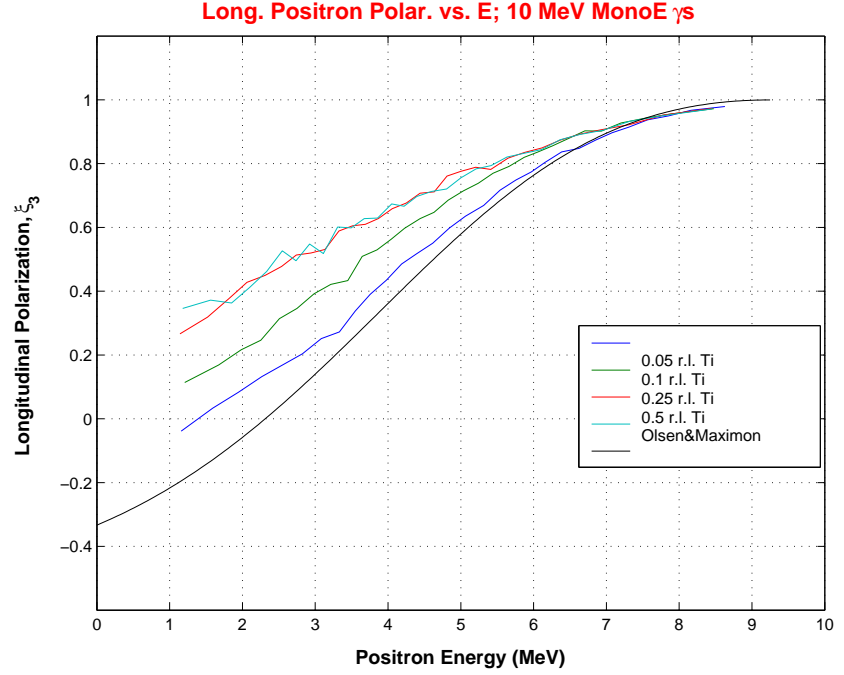
The dependence of the energy of the photons on the emission angle θ for the n^{th} -order multipole radiation is described by the expression:

$$E_\gamma(n, \theta) = \frac{nE_{c10}}{1 + (\gamma\theta)^2/(1 + K^2)} \quad (6.4)$$

where E_{c10} is the energy of the first harmonic and $\gamma = E_e/mc^2$. As it was already mentioned, the photon polarization has its maximum value at 0° (highest value of the energy E_γ) and falls off for larger angles (lower energies). The behavior of the polarization P_γ as a function of the energy E_γ is described by Fig. 6.4.



(a)



(b)

Figure 6.5: (a) Longitudinal polarization of positrons produced by conversion of circularly polarized photons as a function of the ratio of positron energy. From [74]. (b) Longitudinal polarization of positrons produced by conversion of 10-MeV circularly polarized photons in targets of various thickness in radiation lengths, as a function of the positron energy.

6.3.2 Polarized Positrons Production

The second step in the production of polarized positrons consists on the creation of electron-positron pairs by means of the interaction of the polarized photons with the material of a thin target. The cross section which describes the polarization transfer was derived by Olsen and Maximon in 1959 [62]. The polarization of positrons as a function of the energy E_{e^+} is shown in Fig. 6.5(a). Here one can notice that the positrons whose energy is close to the energy of the incoming photons are 100% longitudinally polarized, and the polarization diminishes as the energy of the positrons gets smaller. In the case of a finite size target the positrons lose a fraction of the energy due to bremsstrahlung or are completely stopped due to ionization if their energy is low enough. The positron polarization as a function of the positron energy is plotted in Fig. 6.5(b) for targets of various thickness. Another consequence of beamstrahlung is a slight loss of polarization. The fact that the energy loss is larger than the polarization loss leads to a repopulation of the spectrum at smaller energies with positrons of initially higher energies.

6.4 Polarimetry at E-166

Transmission polarimetry is the most appropriate technique for measuring the photon and positron polarization at the E-166 experiment due to the high rate and small energy of the particles. This method is based on the fact that the cross section for Compton scattering of circularly polarized photons depends on the photon polarization. In few words, the amount of transmitted photons through a magnetized iron absorber will depend on the polarization of the photons and the magnetization of the absorber (polarization of the atomic electrons in unsaturated shells). In order to be able to measure the polarization of the positrons, they first have to be reconverted into photons (the photons acquire again the polarization of the positrons according to the graph shown in Fig. 6.7).

Compton scattering cross section. It is possible to write the Compton scattering cross section in terms of an unpolarized cross section σ_o and a polarized one σ_P as [62]:

$$\sigma = \sigma_o + P_\gamma P_e \sigma_P. \quad (6.5)$$

Here P_γ is the photon polarization and P_e is the polarization of the atomic electrons, which for the case of iron is approximately $\pm 2/26$ (from the 26 electrons of an iron atom, the two electrons in the unsaturated shells contribute to the magnetized material

polarization). The unpolarized cross section takes the form:

$$\sigma_o = \frac{\pi r_o^2}{k_o} \left[\left(1 - \frac{2}{k_o} - \frac{2}{k_o^2} \right) \ln(1 + 2k_o) + \frac{1}{2} + \frac{4}{k_o} - \frac{1}{2(1 + 2k_o)^2} \right], \quad (6.6)$$

and the polarized cross section can be written as:

$$\sigma_P = \frac{2\pi r_o^2}{k_o} \left[\frac{1 + 4k_o + 5k_o^2}{(1 + 2k_o)^2} - \frac{1 + k_o}{2k_o} \ln(1 + 2k_o) \right], \quad (6.7)$$

where $r_o = e^2/mc^2$ is the classical electron radius and $k_o = E_\gamma/mc^2$.

Transmission polarimetry for photons. The probability of a photon to be transmitted through a magnetized iron absorber in terms of the photon helicity and electron polarization in the iron P_e is:

$$T^\pm(L) = e^{-nL\sigma} = e^{-nL\sigma_o} e^{\pm nLP_e P_\gamma \sigma_P} \quad (6.8)$$

where n is the number density of atoms in the iron and $T^+(T_-)$ is the transmission probability for the case in which the electron spin is parallel (antiparallel) to the direction of the incoming photons. One must invert the sign of the iron absorber's magnetization to switch between T^+ and T^- . The asymmetry δ obtained from the transmission probabilities T^\pm will be proportional to P_γ as well as to P_e :

$$\delta(L) = \frac{T^+(L) - T^-(L)}{T^+(L) + T^-(L)} = \tanh(nLP_e P_\gamma \sigma_P) \approx nLP_e P_\gamma \sigma_P. \quad (6.9)$$

The electron polarization in the magnetized iron absorber is given by the formula

$$P_e = 2 \cdot \frac{g' - 1}{g'} \cdot \frac{M}{n\mu_B},$$

where $M = (B - B_o)/\mu_o$, is the magnetization, n is the number of electrons per unit of volume, μ_B is the Bohr magneton and g' is the gyromagnetic ratio, known from the Einstein-de Haas type experiment [68]. If the asymmetry takes small values one can define the analysis power A_γ for transmission polarimetry as:

$$A_\gamma(L) \equiv \frac{\delta(L)}{P_e P_\gamma} \approx nL\sigma_P \quad (6.10)$$

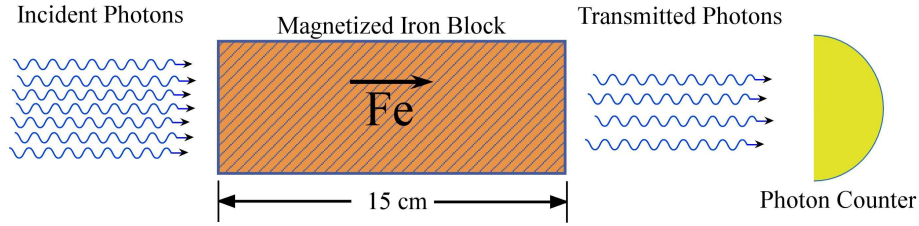


Figure 6.6: Transmission polarimetry for photons. The rate of transmitted photons depends on the iron magnetization.

The photon polarization can be extracted from the asymmetry δ if the electron polarization P_e and the analyzing power A_γ are known:

$$P_\gamma = \frac{\delta}{P_e^- A_\gamma} \quad (6.11)$$

Transmission polarimetry for positrons. The measurement of the positron polarization requires more effort than the photon case due to the necessity of reconvertng the positron into photons. Again it is possible to use the relation:

$$P_{e^+} = \frac{\delta}{P_e^- A_{e^+}}, \quad (6.12)$$

where A_{e^+} is the analyzing power for the positron case. However, now the value of A_{e^+} is not obtained in a simple manner as in Eq. 6.10 (the process of polarization transfer from the positrons to the γ must be also considered), but it has to be obtained from simulations which must take into account the following factors:

- The positrons can suffer depolarization by atomic interactions during the reversion process. For relativistic electrons this effect has a size of a few percent only [69, 70]. This can be studied with a version of the EGS4 [71] code that includes polarization.
- The average polarization of the photons produced by 10-MeV positrons is only 21% of that of the positrons. The transfer of polarization from positrons to photons after reconvertng in a thin foil is shown in Fig. 6.7.
- The large multiple scattering of the positrons in the reversion target will cause the angular distribution of the reconverted photons to be nearly isotropic. For the case of A_γ the photon beam is a collimated one and the computation is easier.

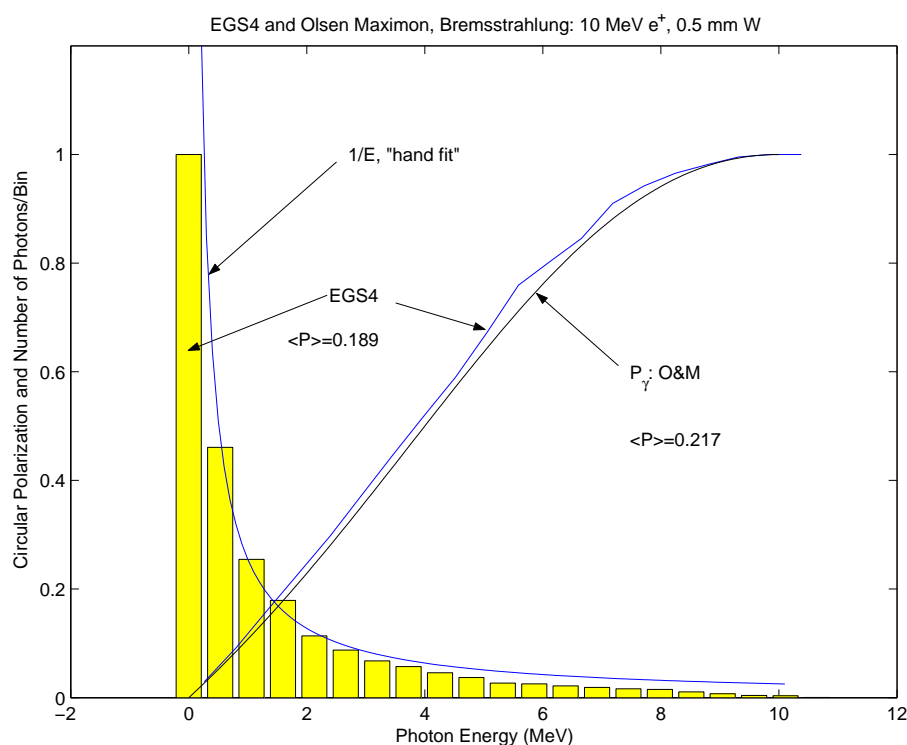


Figure 6.7: The solid curve labeled as $P_{\gamma}:O\&M$ shows the polarization of photons generated by a 10-MeV positron incident on 0.5 mm of tungsten as a function of the photon energy. The line labeled EGS4 is obtained from simulations performed with the code EGS4. The histogram shows the energy spectrum of the photons.

6.5 Structure of the E-166 Experiment

The E-166 experiment is installed at the end of the Final Focus Test Beam FFTB area at SLAC (see Fig. 6.8). The low emittance and high energy provide unique conditions to run the E-166 experiment. In this section the main experimental parameters are introduced.

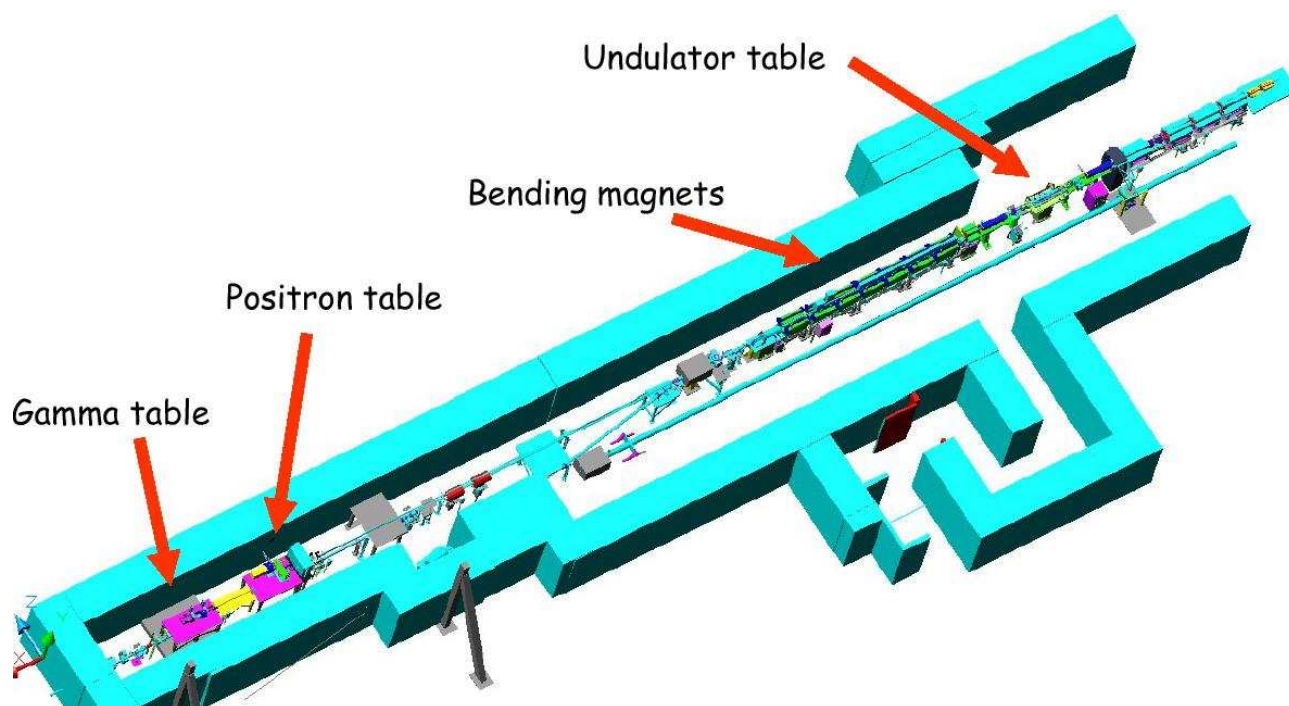


Figure 6.8: A view of the E-166 experiment at the FFTB showing the location of the helical undulator with respect to the photon and positron polarimeters.

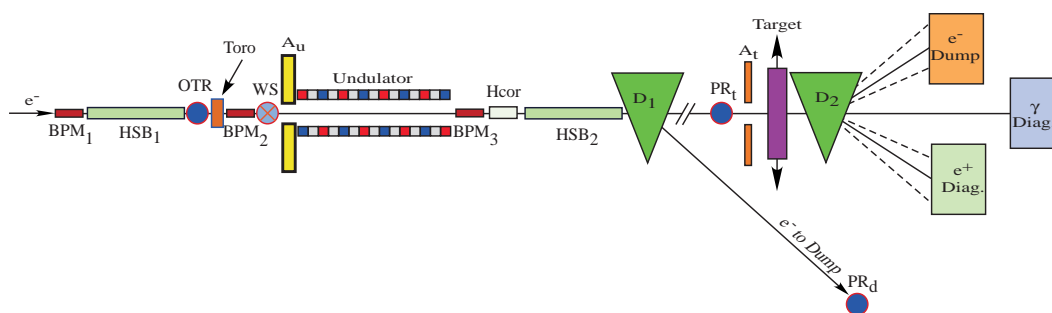


Figure 6.9: E-166 experiment conceptual layout (not to scale). The labels are explained in the text.

6.5.1 Beam Parameters and Background

The beam parameters employed in the E-166 experiment are determined by beam energy requirements and limitations due to background among other conditions. The beam parameters are shown in Table 6.1.

Beam energy. In order to achieve the highest photon energy a 50 GeV electron beam is requested. During the actual measurements a beam energy of 46.6 GeV was employed because not enough klystrons were available to reach the required stability and quality of the beam.

Beam power. The maximum beam power in the FFTB enclosure must not exceed 2.5 kW due to radiation shielding considerations. This value corresponds to a beam current of less than $1 \times 10^{10} e^-/pulse$ for a 50 GeV, 30 Hz operation.

Beam size. The small aperture of the undulator (0.885 mm) demands a small beam size of $40 \mu\text{m}$ rms which corresponds to an undulator radius-to-beam size ratio of 11σ . To achieve this beam size at 50 GeV the β functions at the IP1 must take values between 7.8 m to 3.9 m for an emittance value $\gamma\epsilon$ of $2 - 4 \times 10^{-5}$.

Energy spread. Background generation in the FFTB due to beam loss in regions of large dispersion is controlled by limiting the energy spread to $\sigma_E/E \leq 0.3\%$.

E_e	f_{rep}	N_e	$\gamma\epsilon_x = \gamma\epsilon_y$	$\beta_X = \beta_y$	$\sigma_x = \sigma_y$	σ_E/E
GeV	Hz	e^-	m-rad	m	μm	%
50	30	1×10^{10}	3×10^{-5}	5.2, 5.2	40	0.3

Table 6.1: Beam parameters for the E-166 experiment.

The synchrotron radiation emitted by the electrons in the upstream transport magnets and in the dumping magnets can be largely reduced by locating a pair of soft bends before and after the undulator (HSB₁ and HSB₂ in Fig. 6.9). These bends have the same polarity and give a vertical downward kick to the electron beam. The helical undulator is protected from being hit head-on by the primary electron beam by a collimator (referred as A_u in Fig. 6.9) made of copper: a 30-cm-long cylinder with a 0.85 mm inner diameter hole. A second collimator (A_t in Fig. 6.9) with a 3 mm inner aperture is employed to define the photon beam created in the undulator. A beam-current toroid (referred as Toro in Fig. 6.9) is used to measure the electron current on a pulse-to-pulse basis with a relative accuracy of a few tenths of a percent.

Parameter	Units	Value
Number of Undulators	-	1
Length	<i>m</i>	1.0
Inner Diameter	<i>mm</i>	0.89
Period	<i>mm</i>	2.4
Field	<i>kG</i>	7.6
<i>K</i> Undulator Parameter	-	0.17
Current	<i>A</i>	2300
Pulse Width	<i>μs</i>	30
Inductance	<i>H</i>	0.9×10^{-6}
Wire Type	-	Cu
Wire Diameter	<i>mm</i>	0.6
Resistance	Ω	0.125
Repetition Rate	<i>Hz</i>	30
Power Dissipation	<i>W</i>	260
ΔT /pulse	$^{\circ}C$	2.7

Table 6.2: Helical Undulator Parameters.

6.5.2 The Helical Undulator

The helical undulator (Figs. 6.10 and 6.11) consists of a copper wire bifilar helix wound around a stainless steel support tube whose outer diameter is 1.068 mm and the inner one is 0.889 mm. The copper wire has a diameter of 0.6 mm. The undulator parameter of $K = 0.17$ is achieved by inducing an on-axis field of 0.76 T using a 2300 A excitation. An oil bath is employed to cool down the undulator. In addition a water cooled heat exchanger loop is required to remove the heat from the oil. The undulator system parameters are shown in Table 6.2

6.5.3 The Photon Polarimeter

The principle of photon polarimetry was introduced in 6.4. The details of the apparatus are given below for the polarimetry of the photons produced in the undulator. The case of the positron polarimeter will be discussed in 6.5.4. In addition to the total absorption polarimeter, an auxiliary aerogel flux Čerenkov counter is also employed (Fig. 6.12).

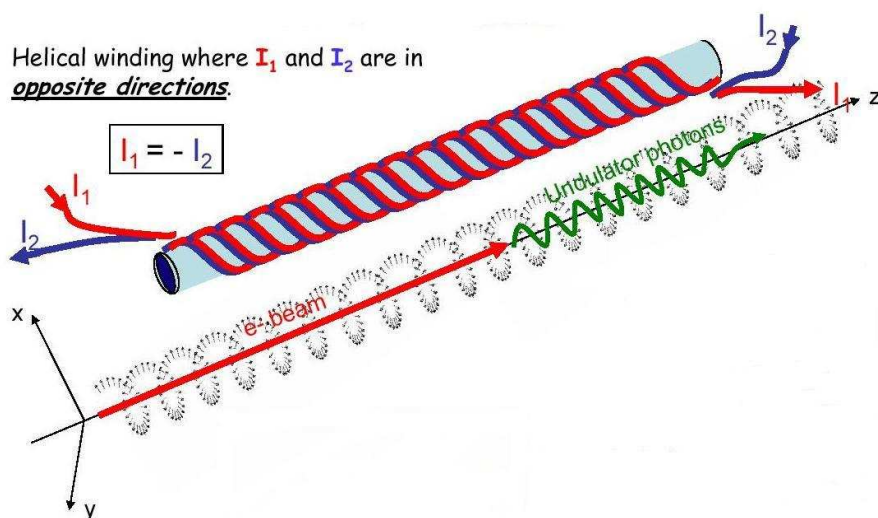


Figure 6.10: Structure of the helical undulator. The current flowing in opposite directions generates a helical field.

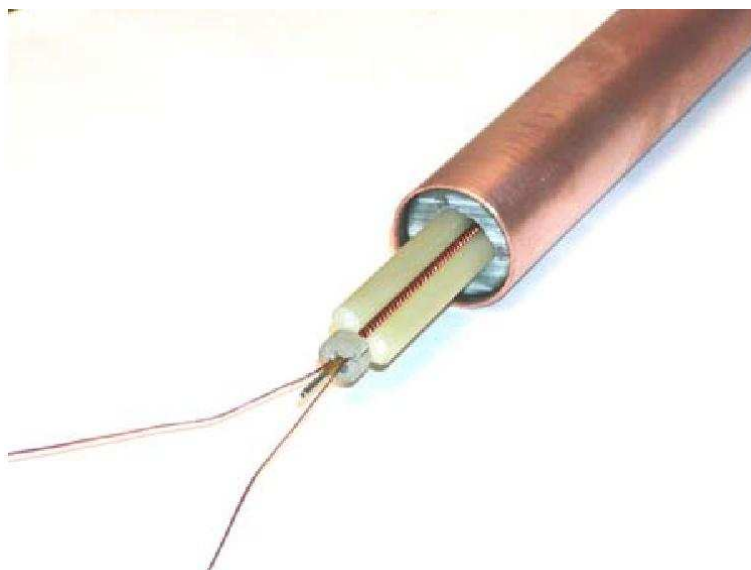


Figure 6.11: One end of a 23-cm-long prototype of the helical undulator.

Magnetized Iron absorber. A 15 cm long magnetized iron absorber is used to minimize the transmission of the synchrotron radiation produced in the soft bend magnets HSB₁ and HSB₂.

Silicon-Tungsten Si-W calorimeter. The photons transmitted through the magnetized iron absorber are detected using a silicon-tungsten calorimeter which consists of 20 plates of tungsten, each 1 rad. len. thick separated by silicon detectors in the form of 4×4 array of pads, each $1.6 \times 1.6 \text{ cm}^2$ in area (Fig. 6.13). The longitudinal segmentation is meant to permit to confirm that the energy deposited in the calorimeter has the profile expected from the signal of the undulator photons. The expected relative error for a pulse of 10^{10} electrons (the expected energy of all the undulator photons produced by such a pulse reaching the calorimeter is about 100 TeV.) is of the order of 0.05%.

Aerogel Flux counters. The aerogel flux counters can be used to confirm the attenuation of the of the absorber photons due to their insensitivity to synchrotron radiation in the beam (their threshold energy is 4.3 MeV). A pair of aerogel flux counters are placed upstream and downstream of the magnetized iron absorber (Fig. 6.12). The aerogel flux counters are Čerenkov counters with an index of refraction $n = 1.007$. Electrons and photons with energies greater than 4.3 MeV will emit Čerenkov light which is observed by photomultipliers.

6.5.4 Positron Production and Polarimetry

As it was mentioned in 6.4, the polarized positrons are generated by converting the circularly polarized photons produced in the helical undulator into electron-positron pairs with the help of a thin target (referred as Target in Fig. 6.9). Next, the desired positron energy is selected in the positron spectrometer (see Fig. 6.12). In order to measure the positron polarization the positrons are reconverted into photons with the help of a reversion target (Fig. 6.12). Finally, transmission polarimetry is employed to determine the polarization of the photons. Each beam pulse containing around 10^{10} electrons produces 4×10^9 photons at the helical undulator, and each photon produces roughly 0.005 positrons. Only 2% of the positrons reach the reversion target of the positron polarimeter. At the end, only about 10^3 photons arrive at the CsI calorimeter. In contrast, approximately 4×10^7 photons arrive at the detector in the photon polarimeter. The elements of the apparatus corresponding to the positron production and polarimetry are described next:

The Positron Production target. Two primary target materials are chosen for

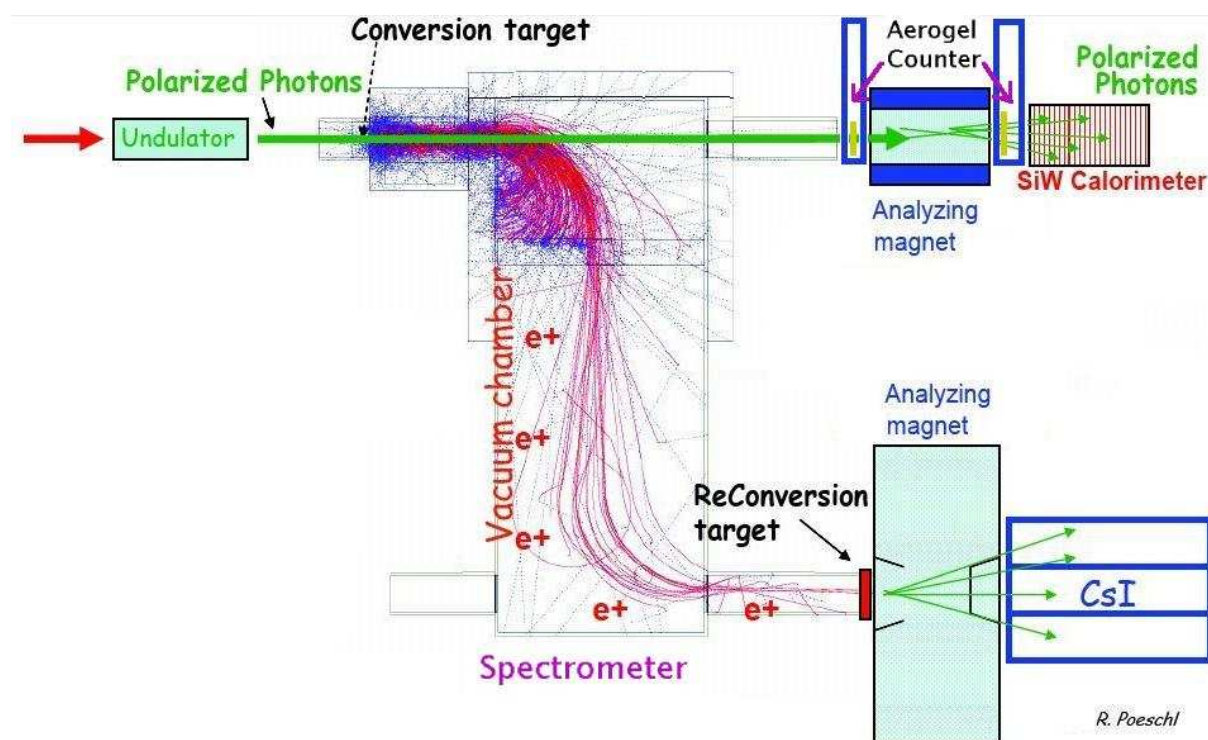


Figure 6.12: Layout of the main components of the photon and positron polarimeters. The figure is not to scale. The helical undulator is located approximately 30 m upstream of the polarimeter.

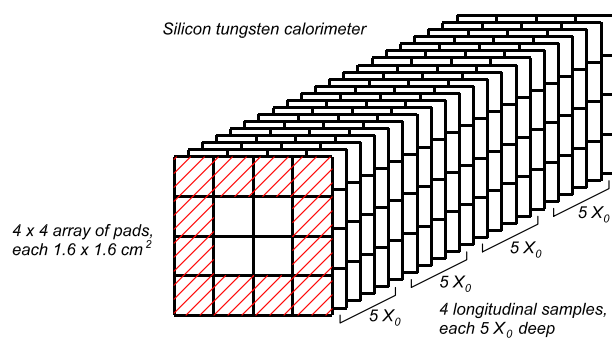


Figure 6.13: The silicon tungsten calorimeter.

the experiment, a high-strength titanium-alloy and a tungsten-rhenium-alloy, being the titanium-alloy the primary choice. For the titanium-alloy target the raw yield is lower and the polarization and emittance is higher. Table 6.3 shows the properties for Ti and W-Re targets of different lengths (a transverse Gaussian spatial distribution of $450 \mu\text{m}$ rms is assumed for the E-166 photon beam). The raw yield is the ratio of the total number of emitted positrons to the number of emitted photons, the raw polarization is the mean longitudinal positron polarization average of all positrons and $\sigma_{x'}$ is the standard deviation of the horizontal angular distribution of positrons. The transverse emittance is the rms horizontal emittance normalized by the (mean positron energy)/ mc^2 .

Material	Thickness (rad. len.)	Raw Yield (%)	Raw Polarization (%)	$\sigma_{x'}$ (rad)	Transv. Emit. (π m-rad)
Ti	0.05	0.34	42	1.1	0.005
Ti	0.1	0.46	48	1.4	0.008
Ti	0.25	0.51	52	1.3	0.009
Ti	0.5	0.46	53	0.7	0.005
W-25%Re	0.05	0.43	36	1.3	0.005
W-25%Re	0.1	0.67	41	1.2	0.005
W-25%Re	0.25	0.93	49	1.5	0.006
W-25%Re	0.5	0.93	51	1.0	0.004

Table 6.3: Properties of positrons generated in Ti and W-Re alloy targets, assuming incident photons from a helical undulator with $K = 0.17$, first-harmonic cutoff energy of $E_{c10} = 9.62$ MeV, and an rms spot size of $450 \mu\text{m}$.

The Positron Transport System. The positron transport system consists essentially of a double 90° system of bend magnets. The main purpose of the transport system is the selection of positrons of a given momentum (within a momentum band of about $\pm 20\%$) while minimizing the background in the reconversion target. The momentum selection can be refined by a set of jaws of variable aperture located between the two magnets.

Magnetized Iron absorber. The iron absorber for the positron polarimeter has a length of 7.5 cm and a diameter of 5 cm. It is surrounded by a water-cooled coil of 360 turns operated at 60 A. The iron must be magnetized to saturation in order to attain the maximum possible magnetization.

CsI Calorimeter. The CsI calorimeter consists in 9 thallium-doped CsI crystals

stacked in a 3×3 array. Each crystal has a front face of $6 \times 6 \text{ cm}^2$ in area and a length of 28 cm. A lead housing protects the crystals from background radiation. Two large area photodiodes located at the rear end of each crystal are used to detect the scintillation light. The CsI calorimeter is appropriate to detect the low energy photons (about 1 MeV) passing the analyzer magnet. The energy resolution for such photon energy is close to 2.5%, in comparison the resolution of the Si-W calorimeter is 20%.

6.6 Data-taking June 2005

The data-taking of the E-166 experiment was carried out in two periods: one in June 2005 and the second one on September 2005. The experience obtained during the June run (data taking and analysis) was used to improve the experimental conditions to be used for the September run. The September data-taking program included the measurement of the positron polarization for different values of the positron momentum. The momentum was selected by adjusting the current in the magnets of the positron spectrometer (described in 6.5.4). Also positron production targets of Ti (titanium) and W (tungsten) (various radiation lengths) were tested.

During the June run only one value for the current of the spectrometer magnets was used: 150 A (roughly corresponds to a positron energy of 5.5 MeV, simulations are still required to find the corresponding positron momentum and momentum band). Two targets were used for the positron production, a 0.25 r.l. (radiation lengths) Ti target and a 0.5 r.l. W target. The first three weeks of June were spent for setting up the required experimental conditions, being the main activities: beam tuning, undulator adjustment, background reduction and detector shielding. The last 10 days were employed for the actual photon and positron asymmetry measurements. The data-taking conditions for the June run are shown in Table 6.4.

6.6.1 Data Analysis

The measurement is accomplished by taking sets of data alternating the orientation of the magnetization (for further reference each set of data is called “a run”). The magnetization was induced/inverted by circulating a current of $\pm 60 \text{ A}$. The normalized particle fluxes through the analyzer magnet is obtained from the stored data taking into account the following elements:

Beam energy	46.6 GeV
Beam pulse frequency	10 Hz
Undulator frequency	10 Hz (Und. OFF every 2nd bunch)
Number of collected beam pulses	$\approx 2 \times 10^5$
Number of collected runs	400
Runs for polarization analysis	≈ 100
Pulses per run	≈ 2000 (signal + background)
Spectrometer current	± 150 A (positron energy: roughly 5.5 MeV)
Current in the analyzer magnets	± 60 A

Table 6.4: Data-taking conditions for the June run.

Flux on the detector. The energy deposited on the detector (Si-W or Csi) is proportional to the number of incoming photons.

Signal normalization In order to account for fluctuations in the beam current the magnitude of the signal (MeV) is divided by the toroid (Subsection 6.5.1) signal (given in ADC counts).

Background subtraction. Every second beam pulse the undulator is pulsed out of phase with respect to the electron beam, this events are called undulator off hereafter. The remaining signal in the CsI calorimeter can be attributed to background events. From this values one can obtain a better estimate for the actual positron signal by subtracting the undulator-off signal from the undulator-on signal.

In Fig. 6.15 the energy (normalized with respect to the toroid signal) deposited by every bunch in the central crystal of the CsI calorimeter is plotted for a typical run for the cases of: undulator-on (signal), shown as a solid line, and undulator-off (background), plotted as a dotted line. The photon signal obtained from subtracting the background from the signal is shown in Fig. 6.16. The mean value \bar{E} of the signal distribution is a measure of the transmission probability T (see 6.4) which is proportional to the number of photons (produced by the positrons hitting the reconversion target) transmitted through the magnetized iron absorber. For each consecutive pair of runs two photon signal distributions are obtained, one for each orientation of the iron absorber magnetization, and hence two mean values for the positron signal distri-

butions, \bar{E}_+ and \bar{E}_- , are also obtained. Employing the value of the asymmetry

$$\delta = \frac{\bar{E}_+ - \bar{E}_-}{\bar{E}_+ + \bar{E}_-} \quad (6.13)$$

in Eq. 6.12 for the computation of the positron polarization will be equivalent to the use of the asymmetry obtained from Eq. 6.9. The same procedure can be applied for measuring the asymmetry in the photon arm polarimeter. A first approach to obtain the energy mean value \bar{E} and the corresponding error for a given run consists in fitting a Gaussian function to the photon signal distribution (method I), from which the mean \bar{E} and the error of the mean $\Delta\bar{E} = \sigma/\sqrt{n}$ (σ^2 is the variance of the distribution and n the number of signal and background event pairs) can be obtained. Each event contained in the photon signal distribution has the form $s_i - b_i$, where s_i (b_i) is the value of the i^{th} undulator-on (undulator-off) measurement of the energy at the CsI calorimeter. In case of a systematic increase or decrease of the beam current the results obtained by this method may depend on the pairing order of the signal and background events (see Fig. 6.14). An alternative to this procedure is suggested by writing the statistical mean value in the following way:

$$\bar{E} = \frac{1}{n} \sum_{i=1}^n (s_i - b_i) = \frac{1}{n^2} \sum_{i=1}^n \sum_{j=1}^n (s_i - b_j). \quad (6.14)$$

Using this idea the photon signal distribution can be conformed by events of the form $s_i - b_j$ for all possible combinations of the signal and background events. One can again fit a Gaussian function to this distribution and extract the mean and the error (we refer to this procedure as method II). The particularities of this methods are discussed in [72]. It is possible to employ even a different number of signal and background events (n and m respectively) to construct the distribution. Now the error determination takes the form:

$$\Delta\bar{E} = \sigma \sqrt{\frac{1}{2} \left(\frac{1}{n} + \frac{1}{m} \right)}, \quad (6.15)$$

which reduces to the form $\Delta\bar{E} = \sigma/\sqrt{n}$ if $n = m$. In this case the statistical significance is the same as in the previous method. One of the advantages of method II is the independence of the asymmetry on the pairing order of the signal and background event. This dependence of the asymmetry can be the result of a systematic increase or decrease of the signal which can become more severe as the data taking period is increased. On the other hand, the potential "damage" on a signal event by a "bad" background event is reduced, helping in this way to improve the quality of the fit.

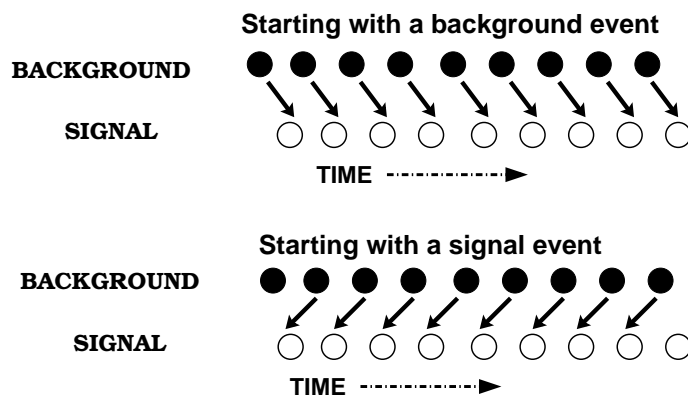


Figure 6.14: Two ways to start the signal and background event pairing.

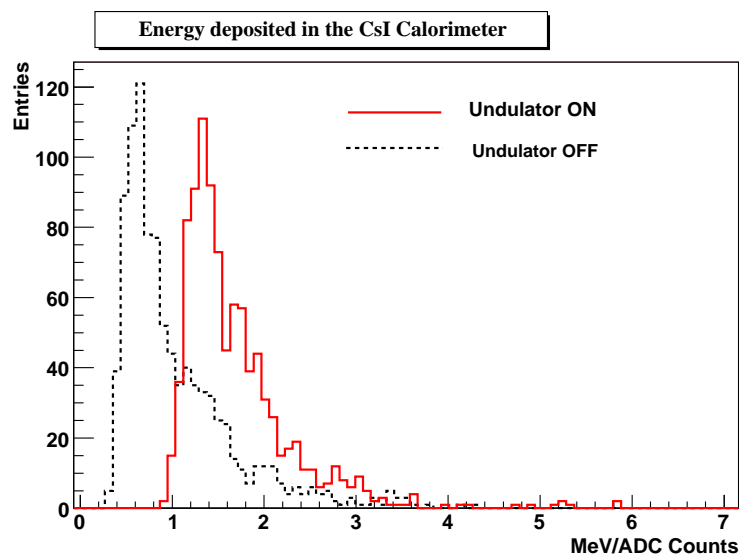


Figure 6.15: Energy (normalized with respect to the toroid signal) deposited by every bunch in the central crystal of the CsI calorimeter.

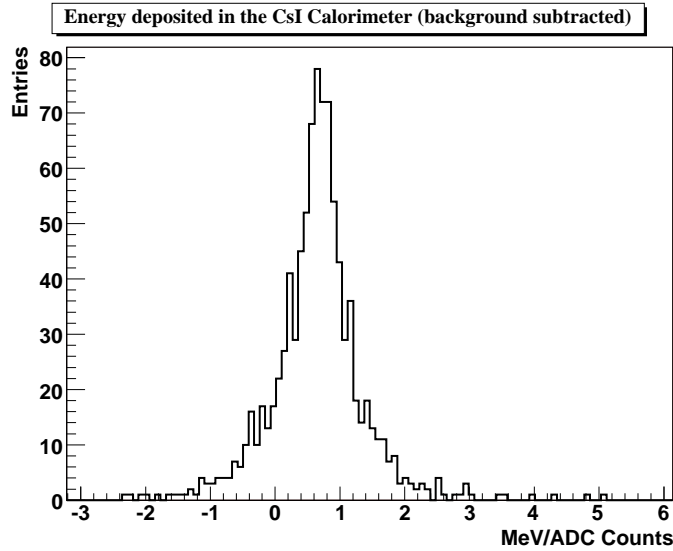


Figure 6.16: Photon signal obtained by subtracting the undulator-off events from the undulator-on events (using only the central crystal of the CsI calorimeter).

The precision of the asymmetry measurement will improve statistically depending on the amount of data (number of runs) considered for the measurement. The way in which several runs are employed to determine the transmission asymmetry is by computing the weighted mean value $\bar{\delta}$ of the asymmetries δ_i corresponding to each one of the available runs:

$$\bar{\delta} = \frac{\sum(\delta_i/(\Delta\delta_i)^2)}{\sum(1/(\Delta\delta_i)^2)} \quad (6.16)$$

The error on the asymmetry is:

$$\Delta\bar{\delta} = \sqrt{\frac{1}{\sum(1/(\Delta\delta_i)^2)}}. \quad (6.17)$$

6.6.2 Results for the Positron Polarimeter Asymmetry Measurements

For the measurements of the asymmetry made with the positron polarimeter only the central crystal of the CsI calorimeter is employed because the background dominates the signal in the surrounding crystals. One of the reasons for this behavior is the

fact that the background is widely spread whereas the signal events travel close to the line pointing into the central crystal. This situation can be appreciated in Fig. 6.20. The quality of the signal in the CsI detector was improved with the help of a series of cuts on the toroid signal and on the photon signal (normalized undulator-on minus undulator-off) distributions:

Cut on the toroid signal. A cut of 3σ around the mean value of the toroid signal distribution (Fig. 6.17) is applied to remove events produced with unstable conditions.

Cut on the photon signal. Large fluctuations around the mean value of the photon signal distributions (Fig. 6.16) may be the result of high background conditions. A cut around 1.5σ is employed to clean-up the signal.

The results of the analysis of 45 pairs of runs taken on June is presented here. The runs were selected according to the cleanness of the data regarding signal/background ratio, shape of the distributions and beam stability as main criteria. Fig. 6.18 shows an example of a signal and background distribution corresponding to a background dominated run (compare with the central plot in Fig. 6.20). From the 45 pairs of runs, 40 were acquired employing the 0.5 r.l. W-target and for the remaining 5 pairs the 0.25 r.l. Ti-target was used. The asymmetry obtained from the 45 pairs of runs using methods I and II is shown in Table 6.5, and the distributions of the individual asymmetries can be appreciated in Fig. 6.19. The values reported in Table 6.5 were computed using Equations 6.16 and 6.17. A selection of 32 pairs of W-target runs was made by rejecting 8 pairs of runs for which the energy mean value ($\bar{E} \approx 0.5$) was significantly lower than the rest of the data ($\bar{E} \approx 0.7$). The asymmetries corresponding to this selection of 32 pairs is also included in Table 6.5. A test is made to check if the origin of the observed asymmetries could be other than the dependence of the Compton cross section on the polarization of the produced positrons and the electrons of the iron analyzer. The asymmetry of pairs of runs, both taken with the same sign of the analyzer magnet polarization is computed. The 32 selected pairs of W-target runs are used to make this test. The results are given in Table 6.6, where the equal sign asymmetries are shown for 16 W-target pairs taken with the magnetization induced by a current of -60 A, for 16 pairs pairs taken with the magnetization induced by a current of +60 A, and for both sets of data combined.

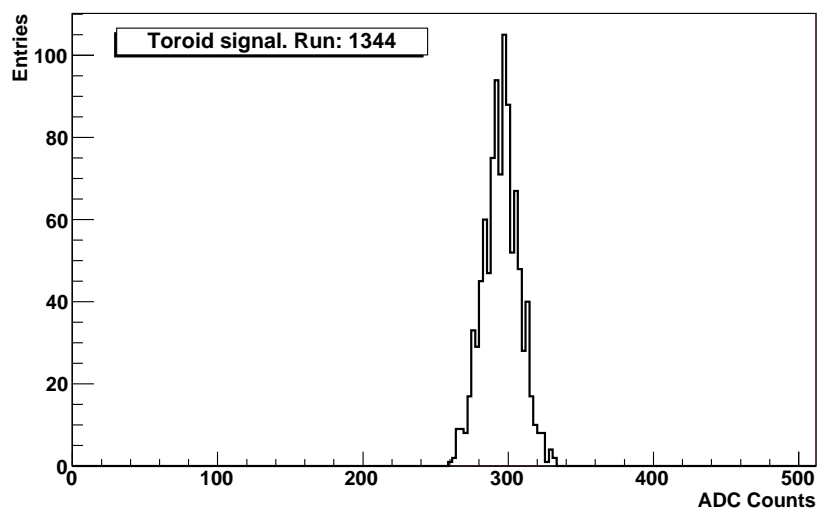


Figure 6.17: Distribution of the toroid signal employed to normalize the photon signal.

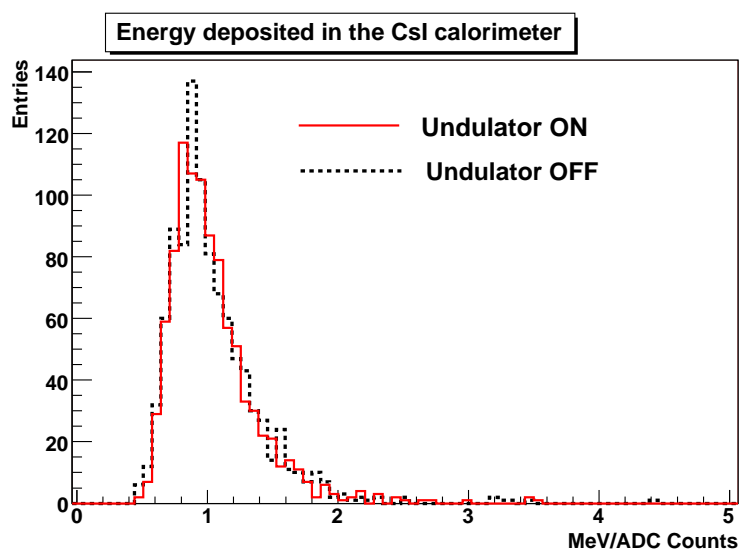


Figure 6.18: An example of a low quality run where the background dominates the signal.

6.6.3 Systematic Errors

The main sources of systematic errors for the measurement of the asymmetry, and consequently of the positron polarization are resumed below. Some of these sources have been already mentioned in subsections 6.6.3 and 6.6.2.

- Unstable beam current conditions. They are avoided by applying a 3σ cut on the toroid signal distribution.
- A constant increase or decrease of the signal leads to slightly different results in the asymmetry measurement when changing the signal-background pairing order (see Fig. 6.14). This problem is overcome by employing the method II exposed in Subsection to find the value of \bar{E} .
- Determination of the degree of magnetization of the iron absorber at the positron polarimeter. In the process of computing the positron polarization from the measured asymmetry, the error in the value of the iron absorber magnetization is one of the factors with largest influence on the error of the positron polarization measurement. Three coils wound around the magnetized iron absorber measure the induced current during the magnetization reversal. With the aid of Faraday's law and the hysteresis curve the magnitude of the magnetization can be obtained.
- Polarization transfer. As commented in Section 6.5.4 the polarization transfer has to be carefully modelled. An effort to model polarized processes using Geant4 [73] is reported in [74]
- Presence of background. It is partially reduced by excluding events in the background-subtracted photon signal distribution which are outside a 1.5σ region around the mean \bar{E} . Other way to quantify the amount of background is the ratio σ/\bar{E} , which may be considered as a measure of the number of events with negative values in the distribution (small values of σ/\bar{E} imply a small number of events with negative values; in the ideal case the normalized energy s_i corresponding to the undulator-on (signal) event should be larger than the value of the undulator-off (background) normalized energy b_i).

The main sources of the non signal photon background are electrons hitting the internal part of the undulator [75] and the collimators. Radiation shields build from tungsten and lead bricks are employed to protect the detectors in order to reduce the background. The statistical behavior of the background subtraction procedure is studied by computing the error on the asymmetry considering only one quarter of the total

number of bunches per run; the resulting statistical error is doubled. Taking into account all the bunches of the 45 studied pairs of runs and method I, a statistical error of $\Delta\bar{\delta} = 0.0012$ is obtained (see Table 6.5), if one fourth of the bunches per run is employed, the statistical error increases to $\Delta\bar{\delta} = 0.0024$, suggesting that the influence of the background can be fought by increasing the amount of data.

	Method I		Method II	
	Asymmetry	Error	Asymmetry	Error
All 45 pairs	0.0078	0.0012	0.0073	0.0013
32 selected W-target pairs	0.0077	0.0013	0.0073	0.0014

Table 6.5: Asymmetries of the photon signal at the CsI calorimeter and the corresponding errors for all 45 pairs runs and for 32 selected W-target pairs.

	Method I		Method II	
	Asymmetry	Error	Asymmetry	Error
16 selected W-target pairs(-60A)	0.0017	0.0018	0.0004	0.0019
16 selected W-target pairs(+60A)	-0.0001	0.0019	0.0019	0.0020
32 selected W-target pairs	0.0008	0.0013	0.0011	0.0014

Table 6.6: Equal sign asymmetries obtained using the sub-set of 32 W-target pairs of runs.

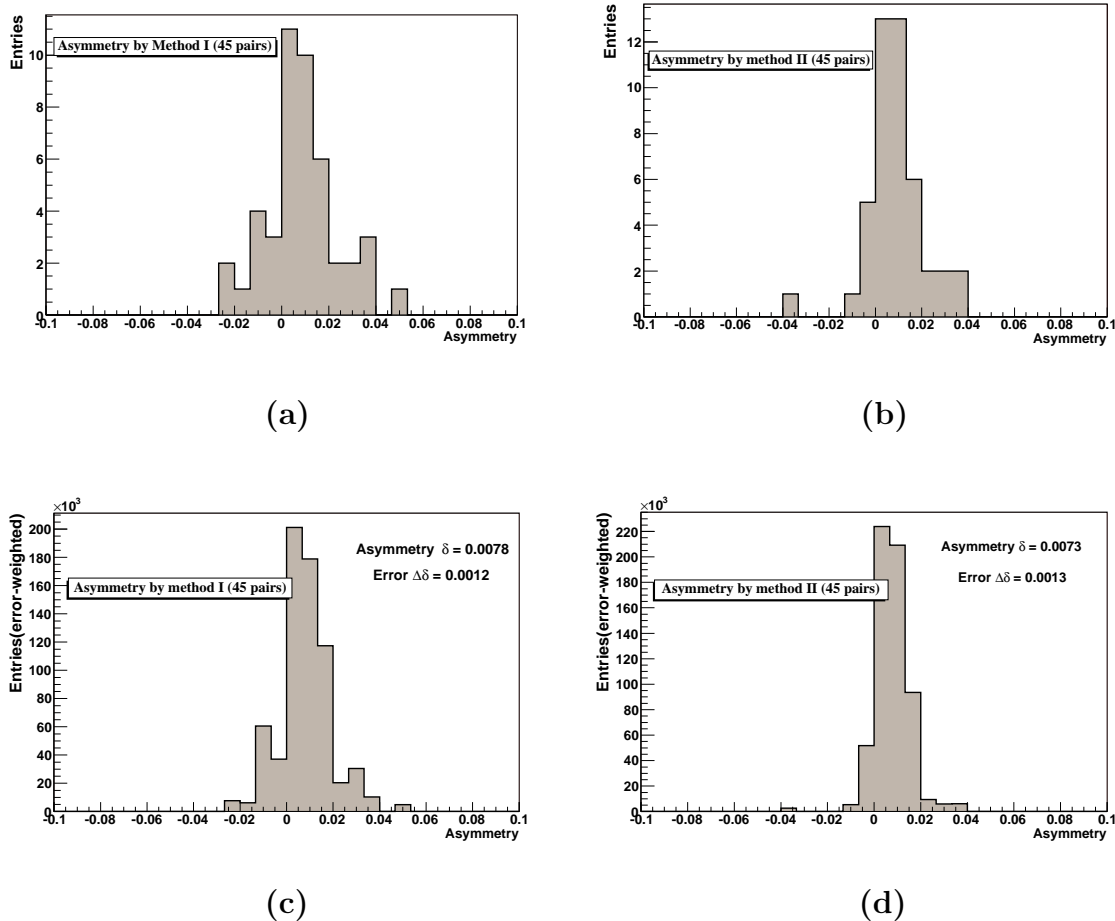


Figure 6.19: Distributions of 45 individual asymmetries (The results are shown in Table 6.5). The bare asymmetries obtained using methods I and II are shown in (a) and (b) respectively. The error-weighted asymmetries obtained using methods I and II are displayed in (c) and (d) respectively. The asymmetries and errors are obtained using Equations 6.16 and 6.17.

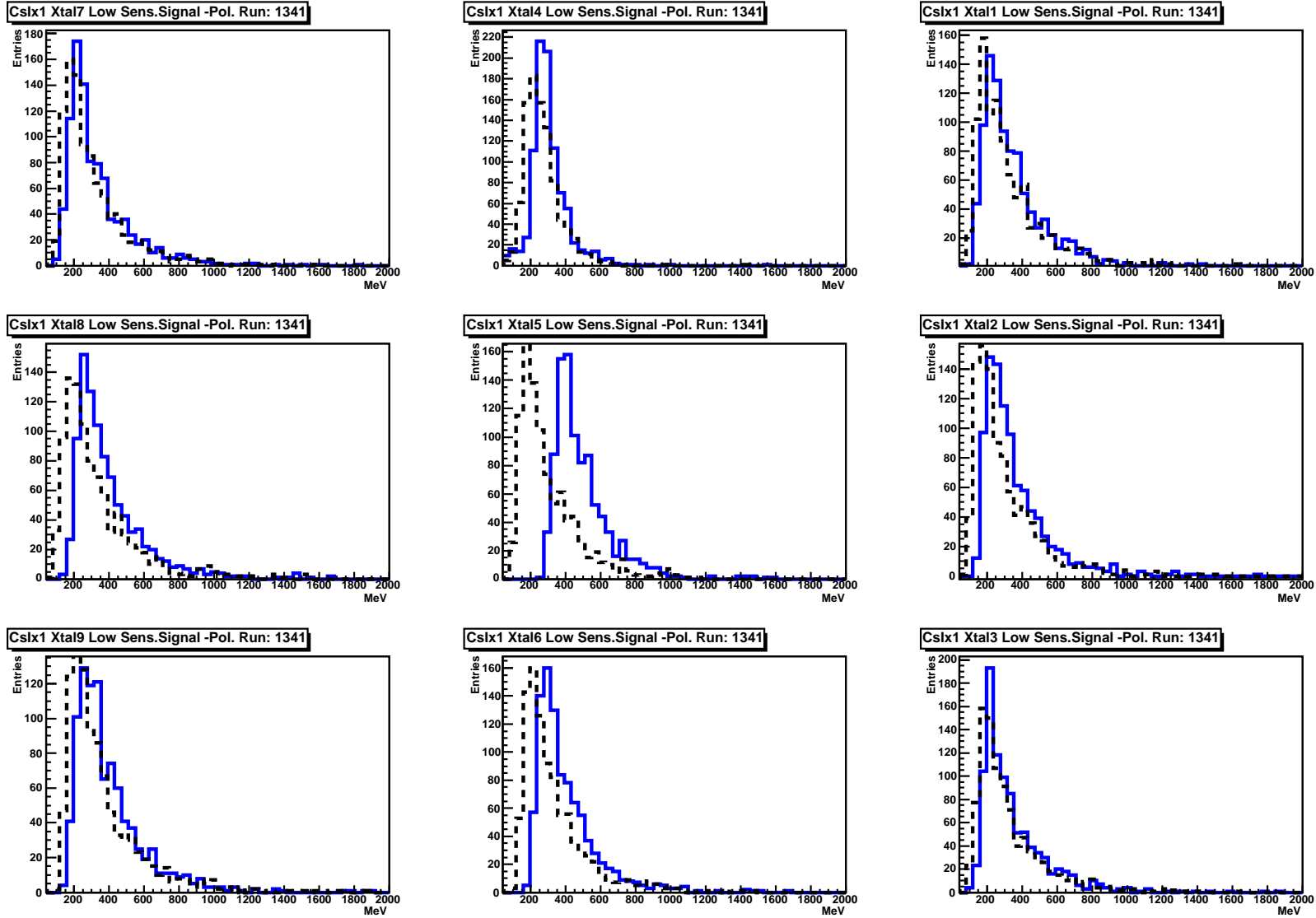


Figure 6.20: Energy deposition in the 9 CsI crystals. The solid line corresponds to the undulator-on events (signal) and the dotted line the undulator-off events (background). The signal is dominated by the background events in the surrounding crystals.

6.7 Conclusions and Outlook

Transmission asymmetries in the positron polarimeter of the E-166 experiment were analyzed for a set of 46 pairs of runs taken on June 2005. The two methods defined in Subsection 6.6.3 were applied giving as a result practically the same values for the asymmetry and the error ($\bar{\delta} = 0.0073$ and $\Delta\bar{\delta} = 0.0013$ using method II), demonstrating the existence of positron polarization. This result is supported by the fact that the equal sign asymmetries are compatible with zero within the error ($\bar{\delta} = 0.0011$ and $\Delta\bar{\delta} = 0.0014$ using method II). The method II is appropriate to remedy effects resulting from a systematic change in the signal, specially for a long data taking period of time.

From the number of useful runs it was clear that the background had to be controlled in a more efficient way, and the experience gained during the June run was used to improve the background conditions for the September data taking period, data which is currently being analyzed by the E-166 collaboration members. Studies on simulations to extract the positron polarization from the measured asymmetry are also being made. Finally, the behavior of the statistical error indicates that an increase of the experimental data would help to reduce the contribution to the error by the photon background .

Summary and Conclusions

The ILC has the capability to test the SM with great precision and make radical discoveries which could repercuss in our current view of the structure of the Universe. The discovery potential of the ILC is significantly increased with the aid of beam polarization, specially when both the electron and the positron beams are polarized (see Section 2.5). Physics processes involving the couplings of three gauge bosons is the perfect place to test the $SU(2)_L \otimes U(1)_Y$ structure of the SM. The potential of the ILC to measure deviations from the SM values of the TGCs using transverse beam polarization is investigated and the results are reported in Chapter 4. For transverse beam polarization the 1σ -bound ranges from 1.0×10^{-3} (for $\Delta\kappa_\gamma$) to 39.0×10^{-3} (for $\tilde{\kappa}_\gamma$). If longitudinal polarization is employed the 1σ -bound takes values between 0.4×10^{-3} and 21.0×10^{-3} for $\Delta\kappa_\gamma$ and $\tilde{\kappa}_\gamma$ respectively (in both cases the 1σ -bound is roughly one half of the corresponding quantity for transverse polarization). Longitudinal polarization helps to increase the sensitivity to anomalous TGCs by selecting contributions from the s-channel diagrams. The azimuthal asymmetry is also studied, in this case deviations from the TGCs SM values manifest with much lower sensitivity. Transverse beam polarization is superior to longitudinal polarization only for the measurement of anomalous values of $\text{Im}(g_1^R + \kappa_R)$ [34].

The use of beam polarization renders the desired precision provided the degree of polarization is known with great accuracy. It was mentioned in Chapter 5 that the current polarimetry techniques can measure the beam polarization with a relative error of about 0.25%. In the same chapter a method to improve the measurements of the polarization employing physics data is exposed; in this case the process of single- W production is employed. This process owns the desired properties to make such a measurement: a high cross section and the possibility to measure the electron and positron beam polarization independently of each other. It was found that this method provides approximately the same precision than the polarimeter based techniques when the single- W muon decay channel is considered and a luminosity of 500 fb^{-1} is dedicated to the measurement, but the result is already free of possible depolarization effects. The expected relative errors are:

$$\Delta P_{e^-}/P_{e^-} = 0.26\% \quad \text{and} \quad \Delta P_{e^+}/P_{e^+} = 0.33\%.$$

Moreover, if also the electron and tau decay channels are used, then the precision of the polarimeters should be overcome. This results were obtained assuming equal share of the luminosity among the two polarization modes necessary for the measurement. The dependence of the polarization relative error on the polarization modes luminosity sharing was also investigated, favoring the right handed electrons and left handed positrons configuration.

The production of polarized electron beams is relatively uncomplicated and its application has already produced important physics results. For the design of the ILC it is necessary to prove the possibility to produce polarized positron beams. In Chapter 6 the first results of the polarized positron production experiment E-166 are presented. The polarized positrons are created during the reconversion of circularly polarized gamma rays in a thin target. The polarized photons are generated by passing the SLAC electron beam (46.6 GeV) through a 1 m long helical undulator. Transmission asymmetry is employed to measure the positron polarization; the positrons have to be reconverted into photons (which inherit the longitudinal polarization of the positrons in form of circular polarization) and the number of transmitted photons through a magnetized iron absorber depends on the orientation of the magnetization and on the polarization of the incoming photons. From the measured asymmetry the value of the positron polarization can be inferred. Employing the data taken in the June 2005 run the transmission asymmetry and the error were obtained (method I and 45 pairs of runs were employed):

$$\bar{\delta} = 0.0078 \quad \text{and} \quad \Delta\bar{\delta} = 0.0012,$$

demonstrating the production of polarized positrons. The error is of statistical nature, but the influence of the photon background and other sources of systematics were studied indicating that the use of a larger set of data can significantly help to reduce the overall error. The experience gained during the June 2005 run was employed to improve the background conditions for the September 2005 run. Studies based on simulations are being made to obtain the magnitude of the positron polarization from the measured asymmetry.

Bibliography

- [1] S. Glashow, Nucl. Phys. 22 (1961) 579;
S. Weinberg, Phys. Rev. Lett. 19 (1967) 1264;
A. Salam, in “Elementary Particle Theory”, ed. N. Svartholm, Almqvist and Wiksells, Stockholm (1969) p. 367.

- [2] M. Gell-Mann, Phys. Lett. 8 (1964) 214; G. Zweig, CERN-Report 8182/TH401 (1964);
H. Fritzsch, M. Gell-Mann and H. Leutwyler, Phys. Lett. B47 (1973) 365;
D. Gross and F. Wilczek, Phys. Rev. Lett. 30 (1973) 1343;
H.D. Politzer, Phys. Rev. Lett. 30 (1973) 1346;
G.’t Hooft, Marseille Conference on Yang-Mills fields (1972).

- [3] F. Boudjema *et al.*, “Standard Model Processes at LEP-2,” arXiv:hep-ph/9601224.

- [4] A. Miyamoto, in the proceedings of the Workshop on Physics and Experiments with Linear Colliders - Volume I, ed. F.A. Harris et al. (World Scientific, Singapore, 1993), p.141 ; A. Miyamoto, KEK-Preprint 93-116 (1993).

- [5] G. Moortgat-Pick *et al.*, “The role of polarized positrons and electrons in revealing fundamental interactions at the linear collider,” arXiv:hep-ph/0507011.

- [6] K. Moffeit, M. Woods, P. Schuler, K. Moenig and P. Bambade, “Spin rotation schemes at the ILC for two interaction regions and positron polarization with both helicities,” SLAC-TN-05-045

- [7] F. Franco-Solova, “A study of triple gauge boson couplings in W-pair production at the linear collider using transversely polarized beams,” LC-PHSM-2004-011
- [8] [ALEPH Collaboration], “Precision electroweak measurements on the Z resonance,” arXiv:hep-ex/0509008.
- [9] S. Eidelman *et al.* [Particle Data Group], “Review of particle physics,” Phys. Lett. B **592** (2004) 1.
- [10] W. R. Leo, “Techniques For Nuclear And Particle Physics Experiments: A How To Approach,”
- [11] O. Adriani *et al.* [L3 Collaboration], “Determination of the number of light neutrino species,” Phys. Lett. B **292** (1992) 463.
- [12] D. Decamp *et al.* [ALEPH Collaboration], “Determination Of The Number Of Light Neutrino Species,” Phys. Lett. B **231** (1989) 519.
- [13] [LEP Collaboration], “A combination of preliminary electroweak measurements and constraints on the standard model,” arXiv:hep-ex/0312023.
- [14] LEP Electroweak Working Group (LEP EWWG) Home Page, <http://lepewwg.web.cern.ch/LEPEWWG/>, Modified: Mon Aug 4 15:54:02 METDST 2003 by Martin Grnewald.
- [15] V. M. Abazov *et al.* [D0 Collaboration], “A precision measurement of the mass of the top quark,” Nature **429** (2004) 638 [arXiv:hep-ex/0406031].
- [16] The CDF Collaboration, the D Collaboration, and the TEVATRON Electro-Weak Working Group. Combination of CDF and D Results on the Top-Quark Mass. Preprint at <http://www.arXiv.org/hep-ex/0404010> (2004).
- [17] “ITRP final report”, September 2004.
<http://www.linearcollider.org/cms/?pid=1000025>
- [18] Large Detector Concept Outline Document, Draft Version 1.3, March 8, 2006. Prepared by the LDC group for the Reference Design Report of the International Linear Collider. <http://www.ilcldc.org/>

- [19] G. Materlik *et al.*, “TESLA: The superconducting electron positron linear collider with an integrated X-ray laser laboratory. Technical design report. Pt. 5: The X-ray free electron laser,” DESY-01-011
- [20] The International Linear Collider Global Design Effort, “Baseline Configuration Document”, Accepted by GDE at the Frascati, Italy (12 Dec 2005).
- [21] R. Brinkmann *et al.* “TESLA: The superconducting electron positron linear collider with an integrated X-ray laser laboratory. Technical design report. Pt. 2: The accelerator,” DESY-01-011
- [22] T. Behnke *et al.* “TESLA: The superconducting electron positron linear collider with an integrated X-ray laser laboratory. Technical design report. Pt. 4: A detector for TESLA,” DESY-01-011
- [23] T. Lux, “Studies for a time projection chamber for the International Linear Collider and measurement of beauty cross sections in deep inelastic scattering at HERA,” DESY-THESIS-2005-019
- [24] M. Gruwe, “Studies of dE/dx capabilities of a TPC for the future linear collider TESLA,” LC-DET-2001-043
- [25] H. Abramowicz *et al.*, “Instrumentation of the very forward region of a linear collider detector,” IEEE Trans. Nucl. Sci. **51** (2004) 2983.
- [26] R. Alley *et al.*, “The Stanford Linear Accelerator polarized electron source,” Nucl. Instrum. Meth. A **365** (1995) 1.
- [27] “The NLC Design Group, Zeroth-Order Design Report for the Next Linear Collider”, SLAC Report 474, pp 28-34 (1996)
- [28] P. C. Rowson and M. Woods, Contr. to 5th international Linear Collider Workshop (LCWS 2000), Fermilab, Batavia, Illinois, 24-28 Oct 2000. Published in Batavia 2000, Physics and experiments with future linear e+e- colliders, 515-520, SLAC-PUB-8745, Dec.2000, hep-ex/0012055.
- [29] F. Sauli, “GEM: A new concept for electron amplification in gas detectors,” Nucl. Instrum. Meth. A **386** (1997) 531.

- [30] Y. Giomataris, P. Rebourgeard, J. P. Robert and G. Charpak, “MICROMEGAS: A high-granularity position-sensitive gaseous detector for high particle-flux environments,” Nucl. Instrum. Meth. A **376** (1996) 29.
- [31] G. Acquistapace *et al.* [CMS Collaboration], “CMS, the magnet project: Technical design report,” CERN-LHCC-97-10
- [32] J. A. Aguilar-Saavedra *et al.* [ECFA/DESY LC Physics Working Group Collaboration], “TESLA Technical Design Report Part III: Physics at an e^+e^- Linear Collider”, arXiv:hep-ph/0106315.
- [33] For the employment of spin rotators at e.g. HERA see:
E. Gianfelice, “First polarization studies at HERA with 3 spin rotators”, DESY-HERA-03-18
- [34] M. Diehl, O. Nachtmann and F. Nagel, “Probing triple gauge couplings with transverse beam polarisation in $e^+e^- \rightarrow W^+W^-$ ”, Eur. Phys. J. C **32** (2003) 17 [arXiv:hep-ph/0306247].
- [35] K. Hagiwara, R. D. Peccei, D. Zeppenfeld and K. Hikasa, “Probing the Weak Boson Sector in $e^+e^- \rightarrow W^+W^-$ ”, Nucl. Phys. B **282** (1987) 253.
- [36] K. Hagiwara *et al.* [Particle Data Group Collaboration], “Review Of Particle Physics”, Phys. Rev. D **66** (2002) 010001.
- [37] J. Fleischer, K. Kolodziej and F. Jegerlehner, “Transverse versus longitudinal polarization effects in $e^+e^- \rightarrow W^+W^-$ ”, Phys. Rev. D **49** (1994) 2174.
- [38] W. Kilian, WHIZARD. A generic Monte-Carlo integration and event generation package for multi-particle processes(MANUAL), LC-TOOL-2001-039.
- [39] K. i. Hikasa, “Transverse Polarization Effects In $E^+ E^-$ Collisions: The Role Of Chiral Symmetry,” Phys. Rev. D **33** (1986) 3203.
- [40] T. Omori, “A polarized positron beam for linear colliders,” KEK-PREPRINT-98-237 Presented at the 1st ACFA Workshop on Physics Detector at the Linear Collider, Beijing, China, 26-28 Nov 1998

- [41] K. Moenig “The use of Positron Polarization for precision Measurements”, LC-PHSM-2000-059.
- [42] E-166 collaboration: G.Alexander et.al. “Undulator-based production of polarized positrons: A proposal for the 50-GeV beam in the FFTB”, LC-DET-2003-044.
- [43] W. Menges, “ A Study of Charged Current Triple Gauge Couplings at TESLA ”, LC-PHSM-2001-022.
- [44] P. C. Rowson and M. Woods, “Experimental issues for precision electroweak physics at a high-luminosity Z factory,” arXiv:hep-ex/0012055.
- [45] A. Blondel, “A Schemme to Measure the Polarization Asymmetry at the Z Pole in LEP,” Phys. Lett. **B202** (1988) 145.
- [46] T. Tsukamoto and Y. Kurihara, “Single W production to test triple gauge boson couplings at LEP,” Phys. Lett. B **389** (1996) 162 [arXiv:hep-ph/9607353].
- [47] Y. Kurihara, D. Perret-Gallix and Y. Shimizu, “ $e^+ e^- \rightarrow e^-$ anti-electron-neutrino u anti- d from LEP to linear collider energies,” Phys. Lett. B **349** (1995) 367 [arXiv:hep-ph/9412215].
- [48] E. E. Boos and M. N. Dubinin, “Single W boson production at linear colliders,” arXiv:hep-ph/9909214.
- [49] S. Jadach, W. Placzek, M. Skrzypek, B. F. L. Ward and Z. Was, “Monte Carlo program KoralW 1.42 for all four-fermion final states in $e^+ e^-$ collisions,” Comput. Phys. Commun. **119** (1999) 272 [arXiv:hep-ph/9906277].
- [50] J. Fujimoto *et al.*, “grc4f v1.1: A four-fermion event generator for $e^+ e^-$ collisions,” arXiv:hep-ph/9603394.
- [51] A. Pukhov *et al.*, “CompHEP: A package for evaluation of Feynman diagrams and integration over multi-particle phase space. User’s manual for version 33,” arXiv:hep-ph/9908288.
- [52] F. Maltoni and T. Stelzer, “MadEvent: Automatic event generation with MadGraph,” JHEP **0302**, 027 (2003) [arXiv:hep-ph/0208156].

- [53] T. Ohl, "O'Mega: An optimizing matrix element generator," arXiv:hep-ph/0011243.
- [54] T. Ohl, "CIRCE version 1.0: Beam spectra for simulating linear collider physics," Comput. Phys. Commun. **101**, 269 (1997) [arXiv:hep-ph/9607454].
- [55] T. Ishikawa, T. Kaneko, K. Kato, S. Kawabata, Y. Shimizu, and H. Tanaka, KEK Report 92-19, 1993, The GRACE manual v1.0; Minami-Tateya collaboration, GRACE User's manual v1.1, 1994.
- [56] E. Barberio, B. van Eijk and Z. Was, "Photos: A Universal Monte Carlo For QED Radiative Corrections In Decays," Comput. Phys. Commun. **66** (1991) 115.
- [57] S. Jadach, B. F. L. Ward and Z. Was, "The precision Monte Carlo event generator KK for two-fermion final states in e+ e- collisions," Comput. Phys. Commun. **130** (2000) 260 [arXiv:hep-ph/9912214].
- [58] "SIMDET - A Fast Simulation Tool for Linear Collider Detector Studies, Development area",
http://www-zeuthen.desy.de/lc_repository/detector_simulation/dev/SIMDET/readme.html
- [59] T. Behnke, G. Blair, K. Mönig and M. Pohl, "BRAHMS-Version 1.00, a Monte Carlo Program for a Detector at a 800 GeV Linear Collider", November 6, 1998,
<http://www.hep.ph.rhbnc.ac.uk/blair/detsim/brahms.html>
- [60] S. Jezequel, Y. Kurihara, M. Skrzypek, Z. Was, "The systematic errors for single W production in ALEPH at generator level, based on KoralW/Grace comparisons", ALEPH note ALEPH:2004-004.
- [61] P. C. Rowson, D. Su and S. Willocq, "Highlights of the SLD physics program at the SLAC Linear Collider," Ann. Rev. Nucl. Part. Sci. **51** (2001) 345 [arXiv:hep-ph/0110168].
- [62] H. Olsen and L.C. Maximon, "Photon and Electron Polarization in High-Energy Bremsstrahlung and Pair Production with Screening," Phys. Rev. **114**, 887 (1959).

- [63] R. Dollan, K. Laihem and A. Schalicke, “Monte Carlo based studies of a polarized positron source for International Linear Collider (ILC),” arXiv:physics/0512192.
- [64] I. Sakai *et al.*, “Production of high-brightness gamma-rays through back scattering of laser photons on high-energy electrons,” Phys. Rev. ST Accel. Beams **6** (2003) 091001.
- [65] R. Wigmans, “Calorimetry: Energy measurement in particle physics,” Oxford University Press (2000).
- [66] G. Y. Kezerashvili, A. P. Lysenko, Y. M. Shatunov and P. V. Vorobev, “Colliding beam polarization measurement using superconducting helical undulator at the VEPP-2M storage ring,” Nucl. Instrum. Meth. A **314** (1992) 15.
- [67] R. Carr, J. B. Kortright, M. Rice and S. Lidia, “Performance of the elliptically polarizing undulator on SPEAR,” Rev. Sci. Instrum. **66** (1995) 1862.
- [68] G.G. Scott, “Review of Gyromagnetic Ratio Experiments”, Rev. Mod. Phys. **34**, 102 (1962).
- [69] S. M. Harris, R. J. Jabbur, “On Depolarization of Fast Positrons by Bremsstrahlung,” Il Nuovo Cimento **XXXII**, (1964) 258-260.
- [70] C. Bouchiat, J. M. Levy-Leblond, “Depolarization of Electrons in Matter”, Il Nuovo Cimento **XXXIII** (1964) 193-200.
- [71] W. R. Nelson, H. Hirayama and D. W. O. Rogers, “The Egs4 Code System,” SLAC-0265
- [72] R. Dollan *et al.*, “Analysis of positron asymmetries using September data,” Internal note E-166 collaboration.
- [73] S. Agostinelli *et al.* [GEANT4 Collaboration], “GEANT4: A simulation toolkit,” Nucl. Instrum. Meth. A **506**, 250 (2003).
- [74] R. Dollan, K. Laihem and A. Schalicke, “Monte Carlo based studies of a polarized positron source for International Linear Collider (ILC),” arXiv:physics/0512192.

- [75] Y. K. Batygin, "Background from undulator in the proposed experiment with polarized positrons," SLAC-PUB-10549

Acknowledgements

The realization of this thesis work was possible thanks to the support of many people. I want to thank Professor Dr. Rolf-Dieter Heuer for his supervision, advices and support during my stay at DESY as a PhD student. I also want to sincerely credit my supervisors, Klaus Desch, Roman Pöschl and Wolfgang Menges, as well as to the FLC group leader Ties Behnke. Also the advices provided by Klaus Mönig and Wolfgang Kilian resulted very valuable for the present thesis work. I also want to thank Prof. Prof. Dr. Caren Hagner and Prof. Dr. Peter Schleper for examining this work.

I equally have to recognize the support of all the FLC group members during my stay at DESY as a PhD student. Special thanks to Ramona Matthes for helping us to put order in our administrative lifes. Finally I want to recognize the valuable support of my family and friends on both sides of the Atlantic.

Appendix A

1) Procedure Employed to Compute the 1σ -bound

- (a) Constructing reference distributions
 - i. MC event distributions for a given observable for 3 different values of α (for example $\alpha_0 = -1$, $\alpha_1 = \alpha_{SM} = 0$ and $\alpha_2 = 1$) are generated.
 - ii. Let $n_i(\alpha)$ denote the bin content of the i -th bin from the distribution histogram for the observable O for a given value of the parameter α . For each one of the bins of the 3 MC distributions a parabola $n_i(\alpha) = A\alpha^2 + B\alpha + C$ which contains the set of points $\{(\alpha_0, n_i(\alpha_0)), (\alpha_1, n_i(\alpha_1)), (\alpha_2, n_i(\alpha_2))\}$ is constructed.
- (b) Determining the 1σ sensitivity limit
 - i. The SM ($\alpha = 0$) reference distribution is compared with distributions for $\alpha \neq 0$ (α is changed in discrete steps of proper size) by the χ^2 method. The $\alpha \neq 0$ distribution is obtained with the aid of the parabolae constructed in 1(a)ii.
 - ii. The value of α for which $\Delta\chi^2 = \chi^2 - \chi_{min}^2 = \chi^2 = 1$ (a vanishing error in the determination of the SM distribution, $\chi_{min}^2 = 0$, is considered) is taken as the 1σ -bound.

2) Procedure Employed to Verify the Method

- (a) 10 statistically independent SM MC distributions with $L = 50\text{fb}^{-1}$ are generated.
- (b) Each one of the 10 distributions are compared with the scaled reference distributions obtained in 1(a)ii. For this, α is changed again in discrete steps until $\min\{\chi^2(\alpha)\} = \chi^2(\alpha_{min})$ is found, and the value of $\alpha = \alpha_{min}$ is associated to the corresponding distribution.
- (c) The fitted values of α found in step 2(b) are filled into an histogram and the width of the distribution is computed.

- (d) This width has to be statistically compatible with the 1σ limit found in 1(b)ii, i.e. no more than 31,7 % of the values should be found outside the 1σ -bound. In this case, the width of the distributions obtained in 2(c) and the 1σ -bound for a given observable coincide.

vector_polarization = T
polarization = 0 -0.6 0
ISR_on = T
ISR_alpha = 0.0072993
ISR_m_in = 0.000511
CIRCE_on = T

CIRCE_acc = 2
CIRCE_chat = 2
CIRCE_ver = 7
CIRCE_rev = 20000426
/

Appendix D

KoralW input file for the $e^+\nu_e\mu^-\bar{\nu}_\mu$ final state.

```

BeginX
*-----|
1          500d0 CmsEne  =CMS total energy [GeV]
4          91.1888d0 amaZ  =Z mass [GeV] (PDG)
5          2.4974d0 gammZ  =Z width [GeV] (PDG)
6          80.230d0 amaW  =W mass [GeV]
14         0.1         min vis PT
15         0.0         inv. mass
16         0           themin
17        800         max Pt2 of photons
1011       1d0 KeyISR  =0,1 initial state radiation off/on (default=1)
1013       1d0 KeyNLL  =0 sets next-to leading alpha/pi terms to zero
*          =1 alpha/pi in yfs formfactor is kept (default)
1014       1d0 KeyCul  =0,1 Coulomb correction, off/on (default=1)
1021       2d0 KeyBra  =0 Born branching ratios, no mixing
*          =1 branching ratios with mixing and naive QCD
*          =2 IBA from the CKM matrix (PDG '96); see filexp.f (default)
1031       1d0 KeyWgt  =0, wtmod=1 useful for apparatus Monte Carlo (default)
*          =1, wtmod varying, option faster and safer
1033       2d0 KeySmp  =0 presampler set as in KORALW v. 1.02-1.2
*          =1 first presampler for all 4fermion final states
*          =2 second presampler for all 4fermion final states (default)
1041       1d0 KeyMix, =0 EW renormalisation scheme 'LEP2 Workshop' (default)
*          =1 'G_mu' scheme
1042       1d0 Key4f   =0, INTERNAL matrix element
*          =1, EXTERNAL matrix element (default)
1044       1d0 KeyZon  =1/0, ZZ type final states ON/OFF (default=1)
1045       1d0 KeyWon  =1/0, WW type final states ON/OFF (default=1)
* If you do NOT want to hadronize nor use Tauola/Photos then set the following:
* 1071       -1d0 JAK1   Decay mode tau+ (default=0)
* 1072       -1d0 JAK2   Decay mode tau- (default=0)
* 1073       0d0 ITDKRC  Bremsstrahlung in Tauola (default=1)
* 1074       0d0 IFPHOT  PHOTOS switch (default=1)
* 1075       0d0 IFHADM  Hadronisation W- (default=1)
* 1076       0d0 IFHADP  Hadronisation W+ (default=1)
* 1084       0          CC03
EndX
*****

```

BeginM

* 1-81: WW Wp=1:1-9; 2:10-18..

Wm=	1:ud	2:cd	3:us	4:cs	5:ub	6:cb	7:el	8:mu	9:ta	/ Wp=
	0	0	0	0	0	0	0	0	0	1:ud
	0	0	0	0	0	0	0	0	0	2:cd
	0	0	0	0	0	0	0	0	0	3:us
	0	0	0	0	0	0	0	0	0	4:cs
	0	0	0	0	0	0	0	0	0	5:ub
	0	0	0	0	0	0	0	0	0	6:cb
	0	0	0	0	0	0	0	1	0	7:el
	0	0	0	0	0	0	0	0	0	8:mu
	0	0	0	0	0	0	0	0	0	9:ta

* 82-202: ZZ Z1=1:82-92; 2:93-103..

Z1=	1:d	2:u	3:s	4:c	5:b	6:el	7:mu	8:ta	9:ve	10vm	11vt	/ Z2=
	0	0	0	0	0	0	0	0	0	0	0	1:d
	0	0	0	0	0	0	0	0	0	0	0	2:u
	0	0	0	0	0	0	0	0	0	0	0	3:s
	0	0	0	0	0	0	0	0	0	0	0	4:c
	0	0	0	0	0	0	0	0	0	0	0	5:b
	0	0	0	0	0	0	0	0	0	0	0	6:el
	0	0	0	0	0	0	0	0	0	0	0	7:mu
	0	0	0	0	0	0	0	0	0	0	0	8:ta
	0	0	0	0	0	0	0	0	0	0	0	9:ve
	0	0	0	0	0	0	0	0	0	0	0	10vm
	0	0	0	0	0	0	0	0	0	0	0	11vt

EndM

////////////////////////////////////

Appendix E

grc4f input file for the $e^+\nu_e\mu^-\bar{\nu}_\mu$ final state.

c... Global initialization

```
call grcevt(-3,iopt,ier)

call grcpar('energy',500.0d0,1,ierr)
call grcpar('process','eCenmcmN',1,ierr)
call grcpar('canon',0,1,ierr)
call grcpar('ncall',80000,1,ier)
call grcpar('itmx1',15,1,ier)
call grcpar('itmx2',14,1,ier)
call grcpar('isrtype',4,1,ier)
```